

# The Atmospheric Circulation of Tidally Locked Terrestrial Exoplanets



Mark Hammond

Hertford College

University of Oxford

A thesis submitted for the degree of

*Doctor of Philosophy*

Trinity Term 2019



## Abstract

Exoplanets are planets orbiting stars other than the Sun. Tidally locked exoplanets always present the same face to their host stars, resulting in a global atmospheric circulation unlike anything in the Solar System. This thesis develops theories of the formation of this global circulation, demonstrates the circulation in atmospheric simulations, and shows its effect on observations of the “lava planet” 55 Cancri e.

The first two chapters introduce the topic and review relevant literature. The next two chapters investigate the atmospheric dynamics of terrestrial tidally locked planets. Chapter 3 uses the Gierasch-Rossow-Williams mechanism to describe the formation of zonal flow on these planets. Chapter 4 uses a shallow-water model linearised about an equatorial jet to show how this zonal flow produces the global circulation pattern and hot-spot shift seen in observations and simulations.

The following chapters use the theory developed in the first part of the thesis alongside atmospheric simulations to interpret the thermal phase curve of 55 Cancri e. Chapter 5 models possible atmospheres with different bulk properties on this planet, and simulates observations for comparison with the original phase curve. Chapter 6 simulates similar atmospheres using more realistic radiative transfer, and shows that the global circulation is similar but that the observed hot-spot shift requires a sufficiently thick atmosphere.

I conclude that the meridional circulation is vital to the formation of zonal flow on tidally locked planets, and that the observable hot-spot shift is caused by wave-mean flow interactions between this zonal flow and the stationary wave response to day-night forcing. The case study of 55 Cancri e suggests that the observations are evidence for an atmosphere thicker than 10 bar with a mean molecular weight higher than that of H<sub>2</sub>, with night-side cloud formation. Future work should use this theoretical understanding of the global circulation alongside more realistic modelling, to interpret the more detailed observations that will be made in the coming decades.



## Acknowledgements

It has been a real pleasure to work on this topic for the last three years. Thanks first of all to Ray for taking me on with such an interesting project, for encouraging me to follow the avenues that led to the different parts of this thesis, and for your encyclopaedic knowledge of any subject we worked on.

Thanks to everyone in the group, which has given me friends and support that I couldn't have imagined when I started. In particular, thanks to Graham, Neil, Shami, and Tim for distractions from work, fun times away at conferences, and the occasional collaboration. It has been so exciting to see the group develop in my time here, and I can't wait to see what it can achieve.

Thanks to STFC, Hertford College, and AOPP for all of the financial support and administrative help that made this DPhil possible. I feel very lucky to have been supported by, and a part of, these institutions.

Thanks to my friends at Hertford, those around Oxford, and everyone else who has made my time here such fun. Holidays, dinners, squash, croquet, bops, punting, dog walks, and Pango Pong have all been more important to this thesis than any pseudo-spectral method. Thanks especially to Antonis, Maj, Phoebe, Georgia, Adam, Sacha, Dáire, and everyone from Pembroke. Thank you Mann, for making me so happy, supporting me every day, and even eventually remembering the name of the planet I'm researching.

Finally, thanks most of all to my family. I have always felt encouraged to do whatever interested me, and I am so grateful for all of the support I have had in going down this path.



# *Contents*

---

|          |   |           |
|----------|---|-----------|
| <b>1</b> | <b>Introduction</b>   | <b>1</b>  |
| <b>2</b> | <b>The Atmospheric Circulation of Tidally Locked Exoplanets</b>           | <b>5</b>  |
| 2.1      | Exoplanets . . . . .  | 5         |
| 2.2      | Tidally Locked Planets . . . . .  | 9         |
| 2.3      | Atmospheric Dynamics . . . . .  | 14        |
| <b>3</b> | <b>The Gierasch-Rosswall-Williams Mechanism on Tidally Locked Planets</b> | <b>21</b> |
| 3.1      | Linear Shallow-Water Model of a Tidally Locked Atmosphere . . . . .       | 22        |
| 3.2      | Linear Model of the GRW Mechanism . . . . .                               | 29        |
| 3.3      | Non-Linear Model of the GRW Mechanism . . . . .                           | 34        |
| 3.4      | GCM Simulations of the GRW Mechanism . . . . .                            | 41        |
| 3.5      | Scaling Behaviour of Zonal Jets on Tidally Locked Planets . . . . .       | 49        |
| 3.6      | Discussion . . . . .  | 52        |
| 3.7      | Conclusions . . . . .   | 54        |
| <b>4</b> | <b>Wave-Mean Flow Interactions in Tidally Locked Atmospheres</b>          | <b>57</b> |
| 4.1      | Linear Shallow-Water Model in Zonal Flow . . . . .                        | 58        |
| 4.2      | Free Modes in Shear Flow on the Beta-Plane . . . . .                      | 60        |
| 4.3      | Forced Response in Shear Flow on the Beta-Plane . . . . .                 | 66        |
| 4.4      | Forced Response in Shear Flow on a Sphere . . . . .                       | 72        |
| 4.5      | Scaling Relations . . . . .   | 74        |
| 4.6      | Discussion . . . . .  | 80        |
| 4.7      | Conclusions . . . . .   | 83        |
| <b>5</b> | <b>Linking the Climate and Thermal Phase Curve of 55 Cancri e</b>         | <b>85</b> |
| 5.1      | Observations of 55 Cancri e . . . . .                                     | 87        |
| 5.2      | Simplified Scaling Theory . . . . .                                       | 91        |
| 5.3      | Exo-FMS Configuration . . . . .   | 95        |
| 5.4      | Simulation Results . . . . .  | 97        |
| 5.5      | Simulated Observations . . . . .  | 106       |
| 5.6      | Discussion . . . . .  | 113       |
| 5.7      | Conclusions . . . . .   | 115       |

|   |            |
|---|------------|
| <b>6 Phase-Resolved Emission Spectra of Potential Climates on 55 Cancri e</b> | <b>117</b> |
| 6.1 Improvements to Exo-FMS . . . . .   | 118        |
| 6.2 Control Simulation Results . . . . .                                      | 120        |
| 6.3 Best-Fit Simulation Results . . . . .                                     | 128        |
| 6.4 Thick Atmosphere Results . . . . .  | 132        |
| 6.5 Discussion . . . . .  | 136        |
| 6.6 Conclusions . . . . .   | 139        |
| <b>7 Conclusions</b>  | <b>141</b> |
| <b>Bibliography</b>   | <b>145</b> |
| <b>A The Exo-FMS GCM</b>  | <b>153</b> |
| A.1 Model Structure . . . . .   | 153        |
| A.2 Finite-Volume Dynamical Core . . . . .                                    | 155        |
| <b>B Pseudo-Spectral Methods for the Shallow-Water Equations</b>              | <b>159</b> |
| B.1 Pseudo-Spectral Collocation for a Single Equation . . . . .               | 159        |
| B.2 Beta-Plane Shallow Water Equations . . . . .                              | 161        |
| B.3 Spherical Shallow-Water Equations . . . . .                               | 163        |

# CHAPTER 1

## *Introduction*

---

Exoplanets orbit stars other than the Sun. Over the past two decades since the first was discovered, new types of exoplanet have been discovered unlike anything in the Solar System. Tidally locked planets, where the same side of the planet always faces its star, are among the most striking examples. The global circulation of an atmosphere that is only heated on one side is very different to anything seen in the Solar System. This thesis considers the formation and behaviour of this global circulation, and investigates a case study of an observed tidally locked terrestrial planet.

Tidally locked planets appear to be common despite their unusual behaviour. Figure 1.1 shows the exoplanets listed on the NASA Exoplanet Archive<sup>1</sup> at the time of writing plotted by stellar masses and semi-major axes. All the planets below the line were estimated to be tidally locked by the simple estimate in [Pierrehumbert and Hammond \(2019\)](#). These planets are also generally more easily characterised due to their proximity to their host stars ([Crossfield, 2015](#)). This may have created a detection bias, where we are more likely to find tidally locked planets. However, it means that they make up many of the best observational targets, so a theoretical understanding of them will be vital to making the most of upcoming measurements.

---

<sup>1</sup>[exoplanetarchive.ipac.caltech.edu](http://exoplanetarchive.ipac.caltech.edu)

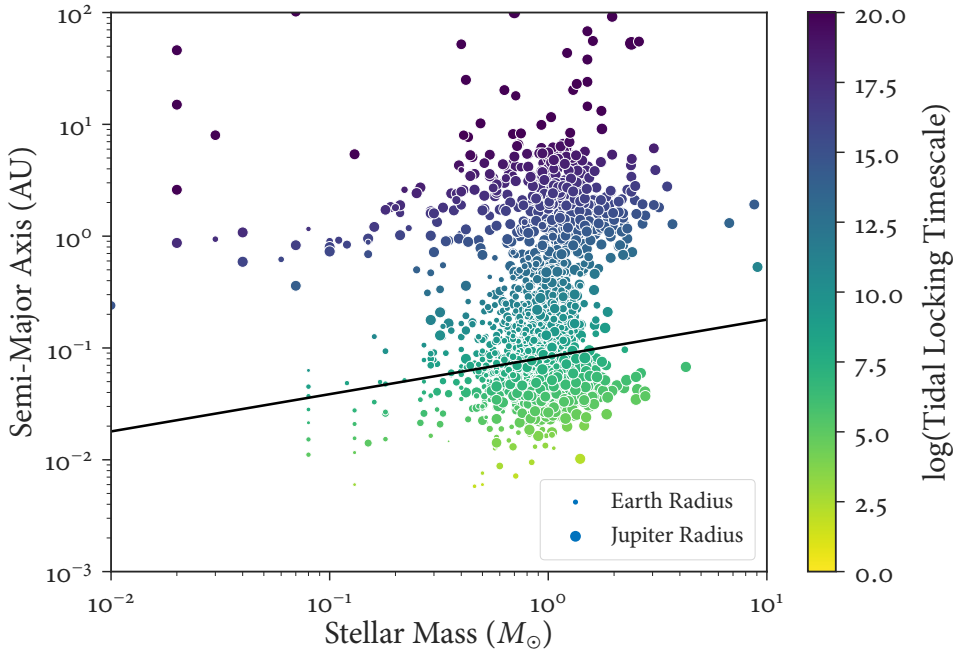


Figure 1.1: The population of known exoplanets plotted by semi-major axis and stellar mass. All the planets below the line have a timescale to reach a tidally locked state of less than 0.1 billion years, so are expected to be in this state. Chapter 2 explains how this timescale is calculated.

Current observations and simulations show that these planets have unique atmospheric dynamics, but the mechanisms for the formation of their global circulation and its effects on planetary climate are not fully understood (Heng and Showman, 2015; Pierrehumbert and Hammond, 2019). The circulation governs the temperature structure of the atmosphere, affecting atmospheric stability, observations of composition, and many other important features.

This thesis has two main themes. In the first part, Chapters 3 and 4 address the theoretical circulation of terrestrial tidally locked planets and its observational consequences. In the second part, Chapters 5 and 6 apply this theory to a case study of the “lava planet” 55 Cancri e, using a variety of models to interpret observations of its thermal emission.

---

The two themes of the thesis are reviewed in Chapter 2, “The Atmospheric Circulation of Tidally Locked Exoplanets”, which discusses relevant work on the subject of tidally locked exoplanets, focusing on the tidal locking process and the resulting atmospheric circulation. It introduces the planet 55 Cancri e, and discusses its observational characterisation to date.

In Chapter 3, “The Gierasch-Rossow-Williams Mechanism on Tidally Locked Planets”, I propose a mechanism for the formation of the zonal flow on tidally locked planets. It shows that the meridional circulation is vital to this flow, and uses the equilibrium angular momentum fluxes predicted by the mechanism to explain the behaviour of a suite of atmospheric simulations.

Chapter 4, “Wave-Mean Flow Interactions in Tidally Locked Atmospheres”, is based on [Hammond and Pierrehumbert \(2018\)](#). I linearise the shallow-water model of [Showman and Polvani \(2011\)](#) about the equatorial jet discussed in Chapter 3, and show how the response to stationary forcing explains the form of the global circulation in GCM simulations. This shows that the “hot-spot shift” is a result of the interaction of forced stationary waves with the zonal flow, rather than simple advection of heat by the zonal flow.

Chapter 5, “Linking the Climate and Thermal Phase Curve of 55 Cancri e”, is adapted from [Hammond and Pierrehumbert \(2017\)](#). It compares simulations of the atmosphere of the tidally locked planet 55 Cancri e to the observations of [Demory et al. \(2016\)](#), to constrain the properties of the atmosphere. The observed day-night contrast can be matched with one set of parameters, and the observed hot-spot shift can be matched with another simulation. It is only possible to match the observations completely by adding an estimate of the effect of night-side cloud formation.

In Chapter 6, “Phase-Resolved Emission Spectra of Potential Climates on 55 Cancri e”, I use an improved model with more realistic radiative transfer to follow up the work in Chapter 5. The new realistic simulations still obey the scaling relations

in Chapter 5, and are qualitatively similar to the simulation results in the idealised grey-gas model. I show that the simulations with surface pressures of 10 bar do not have phase shifts in their thermal emission at any wavelength, but that a simulation with a surface pressure of 100 bar does have an observable hot-spot shift. I suggest that terrestrial atmospheres with a hot-spot shift will not have a peak offset in their thermal phase curve, unless their atmospheres are sufficiently thick. The chapter concludes that the hot-spot shift observed by [Demory et al. \(2016\)](#) is evidence for an atmosphere thicker than 10 bar and with a higher molecular weight than H<sub>2</sub>.

The conclusions in Chapter 7 summarise the results of each chapter, and discuss their significance and the possibility of further work. The first part of the thesis shows how the global circulation of tidally locked planets is governed by their meridional circulation and the stationary waves produced by day-night forcing. I will conclude that the shallow-water models of the formation of zonal flow and a hot-spot shift on a tidally locked planet match GCM simulations, and suggest how the predictions of these models could be tested by observations. The second part of the thesis shows that the observed thermal phase curve of 55 Cancri e is evidence for a thick atmosphere with a surface pressure over 10 bar, with a mean molecular weight greater than H<sub>2</sub>. I will conclude that this thesis has produced a consistent description of the formation of the global circulation of tidally locked terrestrial planets, and suggest future directions for modelling and observations.

## CHAPTER 2

# *The Atmospheric Circulation of Tidally Locked Exoplanets*

---

This chapter reviews relevant work on the global circulation of tidally locked planets. It discusses the discovery and characterisation of exoplanets, focusing on the measurements that are relevant to their atmospheric composition and dynamics. It reviews the formation of a tidally locked state, and the resulting atmospheric circulation, then introduces the “lava planet” 55 Cancri e.

### **2.1 Exoplanets**

Exoplanets are planets orbiting stars other than our Sun. Several thousand exoplanets have been discovered, showing a large variety of planetary types including many unlike anything in the Solar System. I will use the word “exoplanet” when discussing specific planets or issues relating to observations, and “planet” in a more general context. It is possible to characterise the atmospheres of some exoplanets, measuring their composition or even the effects of their global circulation.

Figure 2.1 shows all the exoplanets from the NASA Exoplanet Archive<sup>1</sup> for which radii and orbital periods were available at the time of writing. It shows several distinct populations. The first divide is between the rocky planets in the lower part below

---

<sup>1</sup>[exoplanetarchive.ipac.caltech.edu](http://exoplanetarchive.ipac.caltech.edu)

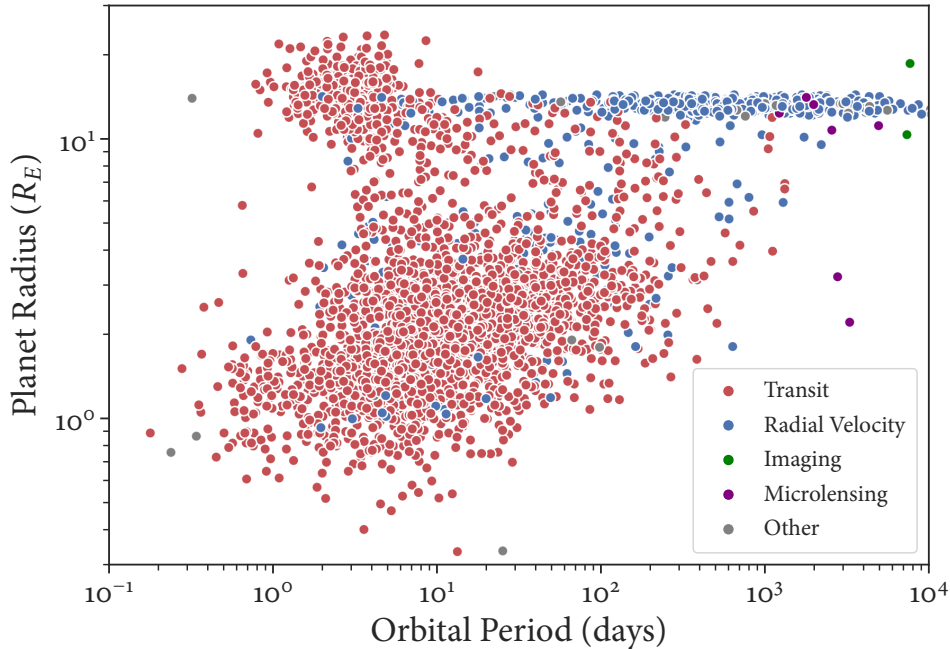


Figure 2.1: The population of known exoplanets plotted by planetary radius and orbital period, labelled by discovery method. The discovery methods are biased towards planets with particular properties.

approximately  $R = 3R_E$  and the gaseous planets above this. The division between these two classes is by no means exact (Perryman, 2018). In the lower left-hand corner are the terrestrial tidally locked planets considered in this thesis, including the hot “lava planets” discussed later. The rocky planets with longer orbital periods are more similar to the inner planets in the Solar System. At larger radii are the “super-Earths”, and then the gaseous “mini-Neptunes” – again, there is no exact division between the populations. At the top of the plot are the gas giants. The hot Jupiters on the left have short orbital periods, and provide the best observations of the atmospheres of tidally locked planets.

### 2.1.1 Discovering Exoplanets

Most exoplanets discovered to date have been found using either a “radial velocity” method or a “transit” method (Perryman, 2018). In the radial velocity (Doppler spectroscopy) method, the motion of a star around its common centre of mass with an orbiting planet is detected by measuring the Doppler-shift of emission lines of the star. The magnitude and period of this motion give the period of the planet’s orbit, and a lower limit on its mass, owing to the degeneracy between the mass and the inclination in their effect on the signal.

In the transit method, an observer measures the reduction in flux from the star when the planet crosses the line of sight from the observer to the star (its “primary transit”). The time between successive transits gives the orbital period of the planet, and the depth of the transit gives the radius of the planet at the wavelength observed. Combining the mass and period from a radial velocity measurement with the radius and period from a transit observation also gives the density and equilibrium temperature of the planet, which are vital for understanding planetary composition and important for atmospheric modelling.

Figure 2.1 shows how different discovery methods are biased towards the detection of different types of planet. The red dots show planets discovered by the transit method, which are currently the most common due to the success of the *Kepler* telescope. These planets are clustered to the left of the plot, as transits are more likely to be detected for close-in planets in short-period orbits, which reduce the flux from their star more strongly when they transit. The blue dots show planets detected by the radial velocity method, which produces stronger signals for higher-mass planets like the gas giants at the top of the plot.

The planets shown in green were detected by direct imaging, in which the light from their host star is blocked with a coronagraph and the planet is directly observed.

This is currently only possible for young, large, self-luminous planets orbiting far from their star, so these planets are found to the top right of the plot. Direct imaging will become possible for more planets in the coming decade ([Perryman, 2018](#)).

### 2.1.2 Characterising Exoplanets

The atmospheres of exoplanets can be characterised with transmission and emission spectroscopy. Transmission spectroscopy measures the spectrum of light from the host star that passes through the atmosphere of the exoplanet as it transits. Measuring the depth of the transit at different wavelengths gives the radius of the planet and its atmosphere at those wavelengths, which depends on the opacity of the atmosphere. This allows the absorption spectrum of the gases in the atmosphere to be reconstructed, which can then be used to estimate the composition of the atmosphere ([Tsiaras et al., 2016](#)).

Emission spectroscopy measures the spectrum of the thermal emission of the planet and its atmosphere. Hotter planets are better suited to this method as they emit more strongly at thermal wavelengths. The thermal emission depends on the composition of the atmosphere and its thermal structure, meaning that it can be used to reconstruct the vertical structure of the atmosphere ([Stevenson et al., 2014](#)).

Features of the atmospheric circulation of exoplanets are starting to be measured. The bulk wind speed of the atmosphere of an exoplanet can be measured via the Doppler-shift of absorption lines in its transmission spectrum ([Louden and Wheatley, 2015](#); [Brogi et al., 2016](#)). Phase curve observations of the thermal emission of an exoplanet over its whole orbit have been used to infer the atmospheric circulation on hot Jupiters ([Zellem et al., 2014](#); [Parmentier and Crossfield, 2017](#)), which I will discuss in more detail later.

## 2.2 Tidally Locked Planets

An asynchronously rotating planet like the Earth has a different rotation period (1 day) to its orbital period (1 year). A synchronously rotating, or “tidally locked”, planet has the same rotation period as its orbital period. This means that it always presents the same face to its host star, so it has a permanent day-side and a permanent night-side. I explained previously that planets orbiting close to their star are more likely to be detected, and are better suited to atmospheric characterisation. This section will show that these close-in planets are more likely to be tidally locked. This means that tidally locked planets should make up many of the best targets for atmospheric observations ([Crossfield, 2015](#)).

### 2.2.1 Formation

All planets are affected by tidal stress due to their gravitational interaction with their host star. At the centre of mass of the planet, the gravitational force exactly balances the centrifugal force. The gravitational attraction is stronger than the centrifugal force for the part of the planet closest to the star, and the opposite is true for the part of the planet further from the star. This produces a stress that elongates the planet along the axis between it and the star. If the planet is not tidally locked, the long axis of the resulting ellipse will rotate away from this axis, and the stress will deform the planet further. This continual deformation removes rotational kinetic energy from the planet, until it reaches a tidally locked state where the long axis of the ellipsoid points towards the star permanently and no more energy is dissipated. Stable spin-orbit resonances are also possible, such as the 3:2 resonant orbit of Mercury, so not all planets affected by these stresses will reach a 1:1 tidally locked state.

The gravitational tidal stress acting on a planet is  $\Sigma = 2GM_*/r^3$ , where  $M_*$  is the mass of the star and  $r$  is the distance between the planet and the star ([Pierrehumbert](#)

and Hammond, 2019). The cubic dependence on  $r$  makes the tidal locking timescale very sensitive to the semi-major axis. Pierrehumbert and Hammond (2019) estimate the time for a planet to become tidally locked to be:

$$t_{\text{lock}} = 3.01 \times 10^8 \frac{\rho \Omega_0 r^6}{M_*^2} \frac{Q}{k_2}, \quad (2.1)$$

where  $r$  is the mean orbital distance in AU,  $\rho$  is the mean density of the planet in units of Earth density, and  $\Omega$  is the angular velocity of the planet in units of Earth angular velocity.  $Q$  corresponds to the effect of the dissipation of energy from tidal stresses (Goldreich and Soter, 1966), and  $k_2$  is the Love number, which depends on the rigidity of the planet (Barnes, 2017). Pierrehumbert and Hammond (2019) use values for Earth and Venus to estimate the ratio for a generic terrestrial planet as  $Q/k_2 \approx 1000$ .

Pierrehumbert and Hammond (2019) use this formula to estimate that the rocky Earth-sized planet Trappist-1d would become tidally locked in 4000 years, assuming that it forms with the same initial angular velocity as Earth. By the same approximation, the super-Earth lava planet 55 Cancri e would take 6 years to reach this state. These short timescales suggest that the planets are very likely to be tidally locked. It is less clear whether planets with estimated tidal locking timescales of millions or billions of years will actually have reached this state.

Leconte et al. (2015) showed how atmospheric thermal tides oppose the gravitational tides discussed above, and slow the progress towards tidal locking. Thermal tides are caused by the thermal inertia of the atmosphere creating an excess of mass in the atmosphere which lags behind the substellar point of an asynchronously rotating planet. The gravitational pull of the star on this mass excess produces a torque on the atmosphere, which acts on the planet in the opposite direction to the torque from the gravitational tide. Figure 2.2 shows that this could inhibit tidal locking

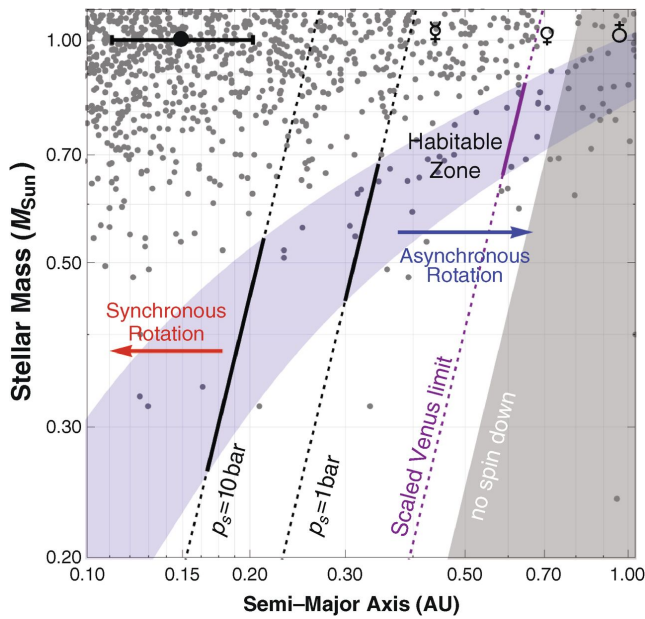


Figure 2.2: A parameter space of stellar mass versus semi-major axis for discovered exoplanets, with lines showing the regions expected to have tidally locked planets with atmospheres of different thicknesses, from [Leconte et al. \(2015\)](#). The thermal tide of the atmosphere may prevent Earth-like planets from becoming tidally locked.

on Earth-mass planets. This effect would not be important for hot Jupiters, or the lava planets investigated in this thesis, but it is worth remembering that the simple estimate of a “tidal locking timescale” is not the whole story for many planets.

### 2.2.2 Lava Planets and 55 Cancri e

Chapters 5 and 6 investigate the atmospheric dynamics of “lava planets”. These are hot rocky planets with a partially or fully molten surface, known as a “magma ocean”. Lava planets are well suited to atmospheric observations due to their high temperatures and proximity to their stars, so are useful case studies for understanding the atmospheric dynamics of tidally locked planets.

55 Cancri e is the best-characterised example of a lava planet. It is a super-Earth with radius  $1.95 R_E$  and orbital period 0.737 days ([Crida et al., 2018](#)). [McArthur et al. \(2004\)](#) first detected the planet via the radial velocity method with an incorrect

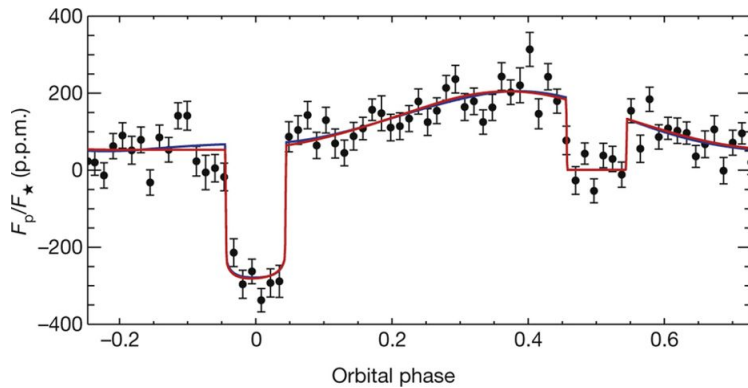


Figure 2.3: The thermal phase curve observed in the  $4.5\text{ }\mu\text{m}$  *Spitzer* bandpass by [Demory et al. \(2016\)](#), showing an offset of the maximum flux from the secondary eclipse (the second dip), corresponding to a hot-spot shift possibly caused by atmospheric circulation. Reproduced from [Demory et al. \(2016\)](#) with permission.

period of 2.808 days. [Dawson and Fabrycky \(2010\)](#) showed that this period was due to spurious aliasing caused by gaps in the observations and corrected the period. It is expected to be tidally locked due to the short tidal locking timescale estimated above, and the observations of [Demory et al. \(2016\)](#).

[Demory et al. \(2011\)](#) and [Winn et al. \(2011\)](#) detected transits of the planet at infrared and visible wavelengths, opening the possibility of atmospheric characterisation. [Demory et al. \(2015\)](#) measured variable day-side thermal emission from 55 Cancri e over eight secondary eclipses, and suggested that this could be due to large-scale changes on the surface caused by strong tidal interactions with the star. [Tsiaras et al. \(2016\)](#) reported the detection of an atmosphere with the WFC3 instrument on the Hubble Space Telescope, which appeared to be hydrogen-rich with a possible detection of HCN. The possibility of observing the composition of an atmosphere of the planet with emission spectroscopy has been explored by [Miguel \(2018\)](#) and [Ito et al. \(2015\)](#), who simulated a variety of spectra of potential atmospheres of different compositions and thicknesses.

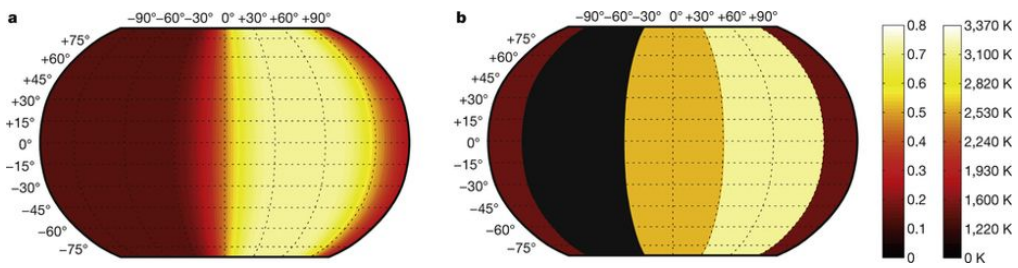


Figure 2.4: The temperature map reconstructed by [Demory et al. \(2016\)](#) from the phase curve in Figure 5.2, showing a hot-spot shift of  $41^\circ$ , a day-side temperature of  $(2700 \pm 270)$  K, and a night-side temperature of  $(1380 \pm 400)$  K. Reproduced from [Demory et al. \(2016\)](#) with permission.

### 2.2.3 A Thermal Phase Curve of 55 Cancri e

A “phase curve” is the radiation received from a planet over one complete orbit of its star. They contain information about how the emission or albedo of the planet varies with longitude, showing features such as day-night temperature differences. Phase curves measured at thermal wavelengths correspond to the radiating temperature of the planet or its atmosphere, so show features such as day-night temperature contrasts on tidally locked planets. Phase curves measured at optical wavelengths show the light from the host star reflected by the planet, so can show how the albedo of the planet varies due to heterogeneous features such as clouds ([Parmentier et al., 2016](#); [Parmentier and Crossfield, 2017](#)). The phase curve has no latitudinal resolution, as the flux at any orbital phase only depends on the longitude at which the planet is observed. Techniques such as “eclipse mapping” can also retrieve latitudinal information, but require stronger emission from the planet ([Majeau et al., 2012](#)).

Phase curves are especially relevant to the atmospheric dynamics investigated in this thesis as the longitudinal variation of temperature on a planet can depend strongly on its global circulation. Figure 2.3 shows the thermal phase curve of 55 Cancri e measured by [Demory et al. \(2016\)](#) using the  $4.5\text{ }\mu\text{m}$  channel of the *Spitzer* space telescope. Figure 2.4 shows the map of brightness temperature inferred from this phase curve. The phase curve implies a night-side temperature of 1300 K, implying a

significant warming of the night-side by atmospheric heat transport. It also shows a hot-spot shifted  $41^\circ$  east of the substellar point, which would be the hottest part without any atmospheric circulation. This hot-spot shift is similar to the phase shift in the optical phase curve measured by [Dragomir et al. \(2012\)](#) with the *MOST* space telescope, which set an upper limit of 0.6 on its geometric albedo.

[Angelo and Hu \(2017\)](#) analysed this phase curve using a similar 1D energy balance model to [Zhang and Showman \(2017\)](#). They tuned the planetary Bond albedo, atmospheric surface pressure, heat redistribution efficiency, and greenhouse effect in this model, to match the observed phase curve. The parameters that fit best were a surface pressure of 1.4 bar and a heat redistribution efficiency of 1.47 (the ratio of radiative to advective timescales).

## 2.3 Atmospheric Dynamics

This section discusses current models of the dynamics of exoplanet atmospheres, and the theory of their global circulation. It introduces the concept of superrotation, which is a key part of the circulation of tidally locked planets.

### 2.3.1 Numerical Atmospheric Models

A General Circulation Model (GCM) is a three-dimensional fluid dynamical model of the atmosphere or the ocean of a planet, or both. They have been used to model the Earth, other planets in the Solar Systems, and are now used to simulate a wide variety of exoplanet atmospheres, often closely matching observations ([Heng and Showman, 2015](#); [Arcangeli et al., 2019](#)). GCMs typically consist of a dynamical core coupled to a representation of physical forcing such as radiative transfer or convective adjustment. The physics modelled in a GCM can range from very simple parameterisations capturing key processes ([Held and Suarez, 1994](#)) to highly detailed

models of interacting clouds, radiative transfer, or other small-scale processes (Lines et al., 2018; Drummond et al., 2018).

The GCM Exo-FMS used in this thesis based on the GFDL Flexible Modelling System<sup>2</sup> and the associated cubed-sphere dynamical core<sup>3</sup> (Ding and Pierrehumbert, 2016; Pierrehumbert and Ding, 2016; Hammond and Pierrehumbert, 2017, 2018). Appendix A outlines the overall structure of the model, the dynamical core and associated grids, and the physics modules that can be swapped in and out of the model.

In the field of exoplanet studies, GCMs have perhaps been applied most successfully to modelling the atmospheres of hot Jupiters (Showman and Guillot, 2002; Mayne et al., 2014; Parmentier et al., 2016; Amundsen et al., 2016; Mayne et al., 2017). Terrestrial planets have also been modelled to suggest potential circulation regimes or stable climate states (Merlis and Schneider, 2010; Showman et al., 2012; Boule et al., 2017; Noda et al., 2017). Other classes of exoplanet such as super-Earths or mini-Neptunes have been modelled in varying levels of detail (Carone et al., 2015; Charnay et al., 2015; Heng and Showman, 2015).

### 2.3.2 Superrotation

Superrotation refers to a state where an atmosphere has more angular momentum than the solid planet below it. There are different ways of defining this mathematically – I will use the definition of Read (1986), which defines superrotation as a positive “superrotation index”, corresponding to an excess of atmospheric angular momentum over solid-body rotation at the equator. The local superrotation index is:

$$s = \frac{m}{\Omega a^2} - 1, \quad (2.2)$$

---

<sup>2</sup>[gfdl.noaa.gov/fms/](http://gfdl.noaa.gov/fms/)

<sup>3</sup>[gfdl.noaa.gov/cubed-sphere-quickstart/](http://gfdl.noaa.gov/cubed-sphere-quickstart/)

where  $\Omega$  is the planetary angular velocity,  $a$  is the radius, and the specific angular momentum  $m$  is:

$$m = a \cos \phi (\Omega a \cos \phi + u), \quad (2.3)$$

where  $\phi$  is the latitude and  $u$  is the local zonal velocity. An atmosphere with an “ideal” meridional circulation would homogenise the angular momentum of the equatorial surface in its upper branch, so the local superrotation index would be zero at all latitudes in that layer. The meridional circulation does not achieve this in reality (as on the Earth) and the superrotation index will be negative in most places ([Read and Lebonnois, 2018](#)). A process transporting angular momentum towards the equator, such as the stationary waves on tidally locked planets that produce an equatorial jet ([Showman and Polvani, 2011](#)), can produce an excess of angular momentum. This gives a positive local superrotation index at the equator.

The global superrotation index is a mass-weighted integral of the local superrotation index, and corresponds to a global measure of the magnitude of superrotation in the atmosphere:

$$S_m = \frac{\iiint \rho m dV}{\iiint \rho \Omega a^2 \cos^2 \phi dV} - 1, \quad (2.4)$$

where  $\rho$  is the local density, and  $\iiint dV$  is an integral over the total volume of the atmosphere. Hide’s Theorem states that the local  $s$  and global  $S_m$  cannot be positive anywhere without up-gradient angular momentum fluxes ([Hide, 1969](#)). Superrotation is found in the atmosphere of Earth and other planets in the Solar System such as Venus and Titan ([Laraia and Schneider, 2015](#); [Read and Lebonnois, 2018](#); [Sugimoto et al., 2019](#)). In this thesis, eastward angular momentum is transported towards the equators of tidally locked planetary atmospheres, producing a superrotating equatorial jet ([Showman and Polvani, 2011](#)).

### 2.3.3 Dynamics of Tidally Locked Atmospheres

The atmospheres of tidally locked planets are forced by their star in a very different way to the planets in the Solar System. The main source of atmospheric dynamics is the strong contrast in heating and cooling between the day-side and the night-side. This could be expected to drive an isotropic flow from the substellar point on the day-side to the antistellar point on the night-side, which can sometimes appear in simulations of very slowly rotating or strongly damped atmospheres (Pierrehumbert and Hammond, 2019; Arcangeli et al., 2019). In more realistic cases with faster rotation, the day-night forcing excites stationary waves that pump eastward momentum towards the equator, producing a superrotating jet that transports heat from the day-side to the night-side (Showman and Polvani, 2011). I will investigate the formation of this zonal flow in Chapter 3.

This equatorial superrotation was predicted by GCM simulations of terrestrial and gaseous tidally locked planets before its effects were observed (Joshi et al., 1997; Showman and Guillot, 2002). These simulations predicted that the jet would shift the hottest part of the planet to the east of the substellar point, which was found to be true in thermal phase curves measured for many hot Jupiters (Parmentier and Crossfield, 2017). Figure 2.5 shows a typical global temperature map from a simulation of a tidally locked planet, with the hot-spot shifted east of the substellar point. This shift was initially thought to be caused by pure advection of heat by the flow, but Tsai et al. (2014) showed that the eastward jet could shift the stationary waves excited by the day-night forcing eastwards, producing the hot-spot shift. Perez-Becker and Showman (2013) also showed that the wave timescale is more important to this shift than the advective timescale of a hot Jupiter. I will discuss this in more detail in Chapter 4, and will show how a latitudinally sheared equatorial jet produces the global circulation pattern and hot-spot shift.

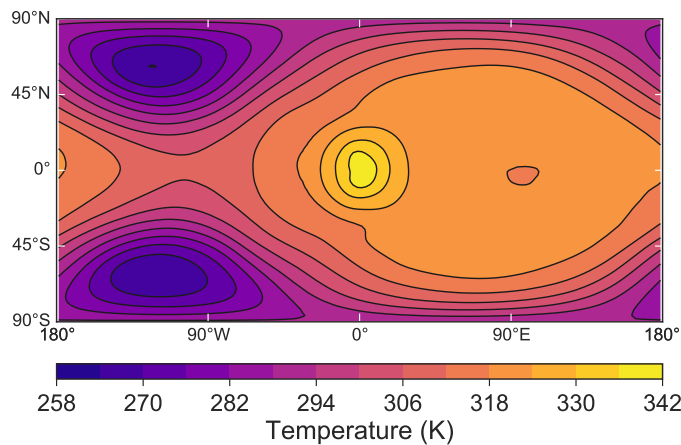


Figure 2.5: The global temperature field at 500 mbar of a simulation of a tidally locked Earth-sized planet with a 10 day rotation period and a 1 bar  $\text{N}_2$  atmosphere, showing an eastward shifted hot-spot and night-side cold stationary waves, reproduced from [Pierrehumbert and Hammond \(2019\)](#).

The formation of the superrotating jet is still not fully understood. Studies such as [Kataria et al. \(2015\)](#) compared real observations to the results of GCM simulations of tidally locked hot Jupiters, expecting that the global circulation formed by the GCM was reasonably accurate. However, [Thrastarson and Cho \(2010\)](#) suggested that simulations of the atmospheres of hot Jupiters depended strongly on initial conditions, and that the equilibrium states were not necessarily unique. [Liu and Showman \(2013\)](#) suggested that this was not the case if a bottom drag was applied to the atmosphere, which they justified as an interaction with a deeper layer not represented in the GCM. Their simulations reached the same equilibrium state regardless of the initial conditions. However, [Cho et al. \(2015\)](#) demonstrated that the short timescale of this drag removed the variability otherwise present in the simulations, and concluded that while a bottom drag may remove sensitivity, it may also remove physically important processes from the atmosphere. [Polichtchouk et al. \(2014\)](#) further cast doubt on the results of other GCM simulations by showing significant differences between the results of different GCMs modelling the same exoplanets. More recent simulations such as [Mendonça et al. \(2016\)](#) have successfully modelled hot Jupiters

without applying a bottom drag, suggesting that the earlier discrepancies may have been problems with the specific models. The question of the sensitivity to initial conditions and role of bottom drag is still not fully resolved, which motivates the investigation of the basic dynamics forming this global circulation in Chapter 3.

It is becoming possible to predict and test scaling relations of atmospheric circulation against observations of many exoplanets in a large parameter space. [Komacek and Showman \(2016\)](#), [Komacek et al. \(2017\)](#), and [Zhang and Showman \(2017\)](#) used a 1D model balancing the advection of heat against radiation to model the circulation of a tidally locked planet. These models were used to explain scaling relations between the observed atmospheric circulation and the bulk composition and parameters of the atmosphere. Chapters 5 and 6 will compare simulations of the atmospheric dynamics of the tidally locked planet 55 Cancri to observations of its temperature distribution, to constrain its potential atmospheric properties.



## CHAPTER 3

# *The Gierasch-Rossow-Williams Mechanism on Tidally Locked Planets*

---

The global atmospheric circulation of tidally locked planets is driven by day-side heating and night-side cooling. This forcing drives a flow from the day-side atmosphere to the night-side. The flow normally takes the form of single, or multiple, eastward zonal jets. This flow is of primary importance to the temperature distribution, observable features, and climate stability of these planets ([Stevenson et al., 2014](#); [Louden and Wheatley, 2015](#); [Pierrehumbert and Hammond, 2019](#)).

[Showman and Polvani \(2011\)](#) used a linear shallow-water model to represent the atmosphere of a tidally locked planet, showing that equatorward momentum transport produces the eastward jet ([Matsuno, 1966](#)). This linear model requires westward flow at high latitudes to conserve angular momentum when an eastward jet forms on the equator. However, GCM simulations often have eastward flow at all latitudes at the level of their equatorial jet, which is inconsistent with the linear model ([Showman et al., 2015](#); [Kataria et al., 2015](#); [Pierrehumbert and Hammond, 2019](#)).

This chapter uses the Gierasch-Rossow-Williams (GRW) mechanism to describe the formation of the zonal flow on tidally locked planets, and to explain the eastward flow at all latitudes seen in GCM simulations. This mechanism has been used to explain the formation of zonal flow on Venus and Titan ([Gierasch, 1975](#); [Rossow and](#)

Williams, 1979; Read and Lebonnois, 2018). The GRW mechanism combines a mean meridional circulation with an equatorward momentum transport, to produce the equatorial jet while accelerating subtropical jets at high latitudes.

I will recreate this mechanism in linear and non-linear shallow-water models, and show how the effect of the meridional circulation on a tidally locked planet can be approximated by its zonal mean only. I will show that the momentum fluxes governing the equilibrium flow in the shallow-water models are the same as those produced by GCM simulations. The balance of fluxes will predict scaling relations for the relative strengths and directions of the equatorial and high-latitude flow. I will conclude that the new mechanism requires sub-rotating flow at high latitudes – which can be eastward or westward – rather than the westward flow required by the linear model of Showman and Polvani (2011).

### 3.1 Linear Shallow-Water Model of a Tidally Locked Atmosphere

This section reviews the linear shallow-water model used by Matsuno (1966) to model equatorial waves in the Earth's tropics. I will show how Showman and Polvani (2011) used this model to explain the formation of equatorial superrotation in tidally locked planetary atmospheres.

#### 3.1.1 Linear Shallow-Water Equations

Matsuno (1966) constructs a single-layer shallow-water model representing a single layer of fluid with a free upper surface on an equatorial beta-plane:

$$\begin{aligned} \frac{\partial u}{\partial t} - \beta y v + \frac{\partial h}{\partial x} &= 0, \\ \frac{\partial v}{\partial t} + \beta y u + \frac{\partial h}{\partial y} &= 0, \\ \frac{\partial h}{\partial t} + c^2 \left( \frac{\partial u}{\partial x} + \frac{\partial v}{\partial y} \right) &= 0, \end{aligned} \tag{3.1}$$

where  $u$  is the zonal velocity,  $v$  is the meridional velocity,  $h$  is the height,  $t$  is time, and  $c = \sqrt{gH}$  is the gravity wave speed. The “beta-plane” approximates the Coriolis parameter as  $f = \beta y$ , where  $\beta$  is the “Rossby parameter” and  $y$  is the meridional coordinate. Appendix B describes the pseudo-spectral method used to solve these equations.

Non-dimensionalising with time scale  $\sqrt{1/c\beta}$  and length scale  $\sqrt{c/\beta}$  (the equatorial Rossby radius of deformation  $L_R$ ), and assuming all quantities have the form  $f(y)e^{i(kx-\omega t)}$ , the equations describing free perturbations are:

$$\begin{aligned} -i\omega u - yv + ik_x h &= 0, \\ -i\omega v + yu + \frac{\partial h}{\partial y} &= 0, \\ -i\omega h + iku + \frac{\partial v}{\partial y} &= 0. \end{aligned} \tag{3.2}$$

[Matsuno \(1966\)](#) solves these equations analytically to find the dispersion relation of the free modes, and discusses the latitudinal structure of each mode. This chapter focuses on the response to stationary forcing rather than the free modes, but understanding their behaviour is important as their structures and eigenfrequencies will determine their magnitudes and positions in the forced response. The free modes could also be important to the time-variable behaviour of the atmosphere.

The wave-1 forcing on a tidally locked planet is stationary and symmetric about the equator, so it will preferentially excite the lowest-order symmetric modes – the Rossby and Kelvin modes. Figure 3.1a shows the free Rossby mode with zonal wavenumber 1. Its positive eigenvalue  $\omega$  means that the free Rossby mode travels westwards (following the convention in [Matsuno \(1966\)](#) for the relation between eigenvalue and direction of travel). Figure 3.1b shows the free Kelvin mode with zonal wavenumber 1. This is a special solution of the equations with zero meridional velocity, which has a negative eigenvalue so travels eastward as a free wave.

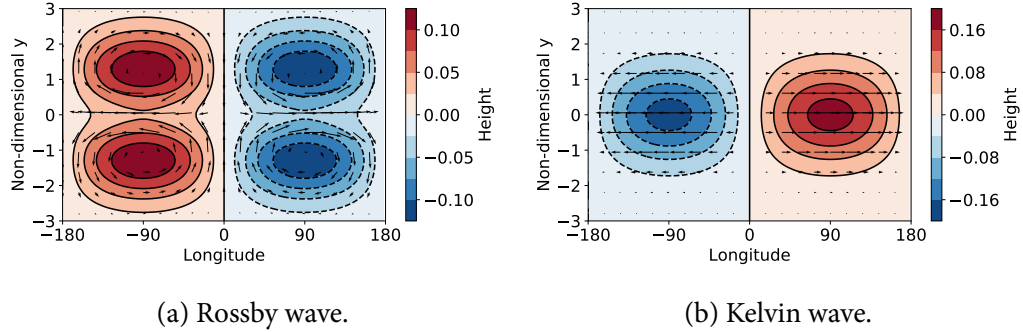


Figure 3.1: The non-dimensional height and velocity fields of the lowest order free modes of a shallow-water system on an equatorial beta-plane. The response to forcing on a tidally locked planet is composed mainly of forced Rossby and Kelvin modes.

### 3.1.2 Linear Response to Forcing

[Showman and Polvani \(2011\)](#) use this linear shallow-water model to represent the atmosphere of a tidally locked planet. A tidally locked planet is constantly heated on its day-side and cooled on its night-side, giving a stationary forcing very similar to the forcing used in [Matsuno \(1966\)](#). This forcing  $Q(x, y)$  acts on the  $h$  field, giving the equations:

$$\begin{aligned} \alpha_{dyn}u - \beta y v + \frac{\partial h}{\partial x} &= 0, \\ \alpha_{dyn}v + \beta y u + \frac{\partial h}{\partial y} &= 0, \\ \alpha_{rad}h + c^2 \left( \frac{\partial u}{\partial x} + \frac{\partial v}{\partial y} \right) &= Q(x, y), \end{aligned} \quad (3.3)$$

where both the dynamical and radiative damping rates  $\alpha_{dyn}$  and  $\alpha_{rad}$  are often set to a uniform damping  $\alpha$  for a simpler solution. The boundary conditions are

$$u, v, h \rightarrow 0 \quad \text{for} \quad y \rightarrow \pm\infty. \quad (3.4)$$

[Matsuno \(1966\)](#) shows how the response of Equation 3.3 to a forcing  $Q(x, y) = Q_0 \sin(x) e^{-y^2/2}$  and uniform damping  $\alpha_{rad} = \alpha_{dyn} = \alpha$  can be found analytically as a sum of the free modes of the system.

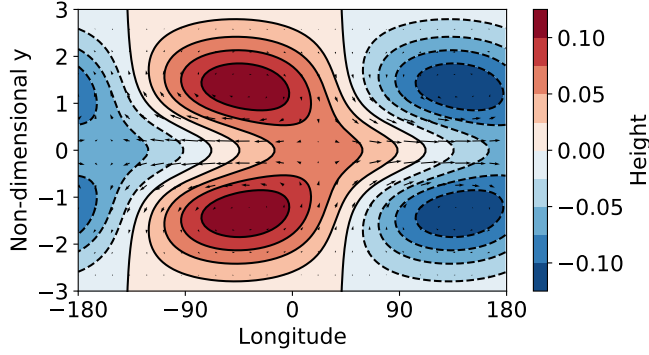


Figure 3.2: Non-dimensional response of Equation 3.3 to forcing  $Q(x, y) = Q_0 \sin(x) e^{-y^2/2}$ , showing the maximum of the Rossby wave west of the maximum of the forcing (the substellar point) and the maximum of the Kelvin wave east of this point.

The forced response  $\chi = (u, v, h)$  is a sum of the free modes  $\xi_m = (u_m, v_m, h_m)$ , weighted by coefficients  $a_m$ :

$$\chi = \sum a_m \xi_m, \quad (3.5)$$

where the coefficients are

$$a_m = \frac{1}{\alpha - i\omega_m} b_m, \quad (3.6)$$

where  $\omega_m$  is the eigenvalue of the mode  $m$ , and the projection of each mode onto the forcing is

$$b_m = \left[ \int \bar{\xi}_m(y) \sigma(y) dy \right] / \left[ \int |\xi_m(y)|^2 dy \right]. \quad (3.7)$$

Figure 3.2 shows the response to the forcing  $Q(x, y) = Q_0 \sin(x) e^{-y^2/2}$ , where all the coefficients  $a_m$  are zero apart from the Kelvin wave and  $n = 1$  Rossby wave. The Rossby wave appears west of the substellar point due to its positive eigenvalue  $\omega_m$ , and the Kelvin wave appears east of the substellar point due to its negative eigenvalue.

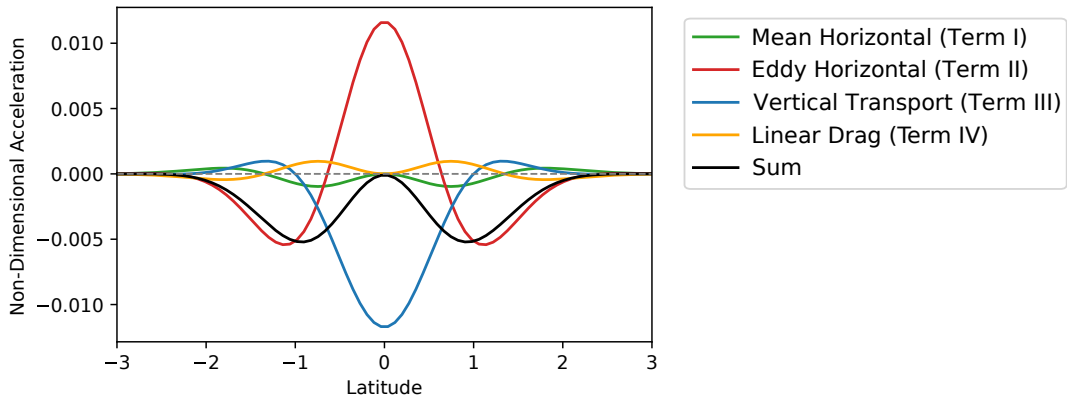


Figure 3.3: Terms in the zonal-mean zonal momentum equation (Equation 3.8) without the correction  $R$  to the momentum. The acceleration terms cancel exactly at the equator, which is why [Showman and Polvani \(2010\)](#) introduced the correction  $R$  to explain the formation of superrotation on tidally locked planets.

### 3.1.3 Equatorial Acceleration

The phase shift between the Rossby and Kelvin waves in the response to forcing produces an equatorward momentum transport that would be expected to produce equatorial superrotation ([Showman and Polvani, 2011](#); [Tsai et al., 2014](#)). Zonally averaging the zonal momentum equation in Equation 4.8 gives the latitudinal acceleration profile ([Thuburn and Lagneau, 1999](#)):

$$\frac{\partial \bar{u}}{\partial t} = \underbrace{\bar{v}^* \left[ f - \frac{\partial \bar{u}}{\partial y} \right]}_{I} - \underbrace{\frac{1}{\bar{h}} \frac{\partial}{\partial y} \left[ \overline{(hv)'u'} \right]}_{II} + \underbrace{\frac{1}{\bar{h}} \overline{u'Q'}}_{III} - \underbrace{\frac{\bar{u}^*}{\tau_{\text{drag}}}}_{IV} - \underbrace{\frac{1}{\bar{h}} \frac{\partial (\overline{h'u'})}{\partial t}}, \quad (3.8)$$

where for a variable  $X$ ,  $\bar{X}^* = \overline{hX}/\bar{h}$ . Figure 3.3 plots the terms in Equation 3.8 for the response to forcing in Figure 3.2. It shows that the horizontal convergence of eastward momentum at the equator due to stationary eddies (term II) is exactly cancelled by the removal of eastward momentum from the equator by vertical momentum transport (term III). This means that the forced linear shallow-water model of [Matsuno \(1966\)](#) does not accelerate at the equator, so a modification is needed to model the atmosphere of a tidally locked planet.

This can be explained by rewriting Equation 3.8 in terms of the relative vorticity  $\tilde{\zeta} = (\nu_x - u_y) \hat{k}$  (Showman and Polvani, 2011):

$$\frac{\partial \bar{u}}{\partial t} = \overline{\nu' \zeta'} + \bar{\nu}(f + \bar{\zeta}) - \frac{\bar{u}}{\tau_{\text{drag}}}, \quad (3.9)$$

For forcing that is symmetric about the equator, the solutions are symmetric about the equator in  $u$  and antisymmetric in  $\nu$ , so are also antisymmetric in  $\zeta$ .  $\nu$  and  $\zeta$  are therefore zero at the equator, so the first two terms in Equation 3.12 are zero. This results in zero acceleration at the equator, for an atmosphere at rest with  $\bar{u} = 0$ .

Showman and Polvani (2010) resolved this problem by introducing a correction  $R$  to the mean vertical momentum transport. The correction represents the effect of advection between the active upper layer and quiescent lower layer (Shell and Held, 2004). Showman and Polvani (2010) explain:

*“Air moving out of the upper layer ( $Q < 0$ ) does not locally affect the upper layer’s specific angular momentum or wind speed, hence  $R = 0$  for that case. But air transported into the upper layer carries lower-layer momentum with it and thus alters the local specific angular momentum and zonal wind in the upper layer.”*

Following Shell and Held (2004), they impose conservation of momentum between the stationary lower layer and the active upper layer, resulting in the correction:

$$R(\lambda, \phi, t) = \begin{cases} -\frac{Q\nu}{h}, & Q > 0 \\ 0, & Q < 0 \end{cases} \quad (3.10)$$

Shell and Held (2004) consider an axisymmetric planet where the air is rising at the equator and falling at the poles. In the tidally locked case, the air is rising at the substellar point and falling at the antistellar point. Figure 3.2 shows that this term produces a net westerly acceleration at the equator. On the day-side where  $Q > 0$ , the equatorial winds are mostly easterly, so  $R$  is non-zero and positive, giving a westerly

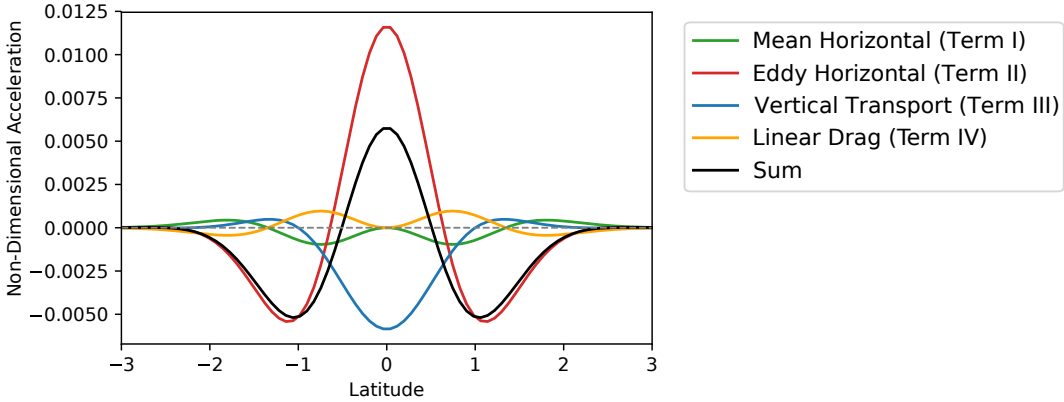


Figure 3.4: Terms in the zonal-mean zonal momentum equation (Equation 3.11) with the correction  $R$  to the momentum. The correction reduces the “Vertical Transport” term in Figure 3.3, giving a net eastward acceleration at the equator.

acceleration. On the night-side,  $Q < 0$  so there is no effect from  $R$ . This asymmetry in  $R$  produces a net westerly acceleration at the equator.

Including the correction  $R$ , the zonal-mean momentum equation becomes:

$$\frac{\partial \bar{u}}{\partial t} = \underbrace{\bar{v}^* \left[ f - \frac{\partial \bar{u}}{\partial y} \right]}_{I} - \underbrace{\frac{1}{\bar{h}} \frac{\partial}{\partial y} \left[ \overline{(hv)' u'} \right]}_{II} + \underbrace{\left[ \frac{1}{\bar{h}} \overline{u' Q'} + \overline{R_u}^* \right]}_{III} - \underbrace{\frac{\bar{u}^*}{\tau_{\text{drag}}}}_{IV} - \underbrace{\frac{1}{\bar{h}} \frac{\partial (\overline{h' u'})}{\partial t}}_{V}, \quad (3.11)$$

and in vorticity form, it is:

$$\frac{\partial \bar{u}}{\partial t} = \overline{v' \zeta'} + \bar{v}(f + \bar{\zeta}) - \frac{\bar{u}}{\tau_{\text{drag}}} + \overline{R_u}. \quad (3.12)$$

Therefore, there is a positive acceleration on the equator unlike in Equation 3.12. Figure 3.4 shows the net positive acceleration at the equator due to the reduced “Vertical Transport” term (Term III in Equation 3.11). This explains the formation of eastward equatorial flow in the atmospheres of tidally locked planets. However, Figure 3.4 shows that this eastward equatorial flow requires westward flow at high latitudes, which is inconsistent with some GCM simulations. The next section will introduce the GRW mechanism to resolve this problem.

## 3.2 Linear Model of the GRW Mechanism

The meridional circulation of an atmosphere is driven by a difference in forcing between its equator and pole. On the Earth, it consists of multiple overturning cells that are approximately zonally uniform. The instellation on tidally locked planets is not zonally uniform so the meridional circulation should vary with longitude. Some studies have measured aspects of the meridional circulation of tidally locked planets in simulations of hot Jupiters and sub-Neptunes ([Charnay et al., 2015](#); [Showman et al., 2015](#); [Mendonça et al., 2018](#)). These studies did not consider the effect of the meridional circulation on the zonal flow, which I will discuss here.

The previous section showed that the linear shallow-water model of [Showman and Polvani \(2010\)](#) explains the formation of equatorial superrotation, but requires westward flow at high latitudes to conserve angular momentum. This is not consistent with many GCM simulations that have eastward flow at all latitudes at the level of their equatorial jet ([Kataria et al., 2015](#); [Showman et al., 2015](#); [Pierrehumbert and Hammond, 2019](#)). The shallow-water model is also not consistent with the evolution of angular momentum seen in GCM simulations. It predicts that the jet layer must lose angular momentum, as the only exchange of momentum out of the layer is a net loss to the lower layer via term III in Equation 3.11. Many simulations of tidally locked planets have positive net angular momentum at the level of their jet (and in total in their atmosphere) so contradict the linear model ([Heng and Showman, 2015](#); [Pierrehumbert and Hammond, 2019](#)).

Both of these problems could be resolved by a process that adds eastward acceleration to the jet layer at high latitudes. This section will suggest that the meridional circulation is this process, forming eastward subtropical jets via the “Gierasch-Rossow-Williams” mechanism that also produces the equatorial jet. I will demonstrate this mechanism in a linear and non-linear shallow-water models and an idealised GCM.

### 3.2.1 The GRW Mechanism on a Tidally Locked Planet

The “Gierasch-Rossow-Williams” (GRW) mechanism was developed by [Gierasch \(1975\)](#) and [Rossow and Williams \(1979\)](#) to describe the formation of zonal flow in the atmosphere of Venus ([Read and Lebonnois, 2018](#)). Figure 3.5 shows the GRW mechanism with the momentum fluxes particular to a tidally locked planet.

The solid arrows in Figure 3.5 show the momentum transport of the mean meridional circulation. I will explain later why this is treated as a zonal-mean process when it varies with longitude in reality. Hot air rises at the equator and travels towards the poles, accelerating eastward to conserve angular momentum. It falls at the poles, and then returns to the equator, accelerating westward to conserve momentum again. Drag from the surface applies a westerly torque to this lower branch, adding prograde eastward momentum to the entire atmosphere. The net effect of this mean meridional circulation is to produce eastward subtropical jets at high latitudes, and a total positive eastward atmospheric angular momentum. The ideal mechanism applies to a planet with a global Hadley cell, avoiding the multiple cells and jets seen on Earth.

The dashed lines in Figure 3.5 show the momentum transport due to the wavenumber-1 “eddy” stationary wave response to day-night forcing ([Showman and Polvani, 2011](#)). The horizontal momentum flux in Figure 3.4 transports angular momentum towards the equator. This produces the eastward equatorial jet and applies a westward acceleration at high latitudes, which is opposed by the eastward acceleration at high latitudes due to the meridional circulation. I will show later that the horizontal and vertical transports balance at the equator in equilibrium, and the horizontal eddy transport balances the mean meridional transport at high latitudes.

This mechanism can resolve the problems introduced at the start of this section. The atmosphere and jet layer gain positive net angular momentum from the drag on the lower branch of the mean meridional circulation. The jet layer can have

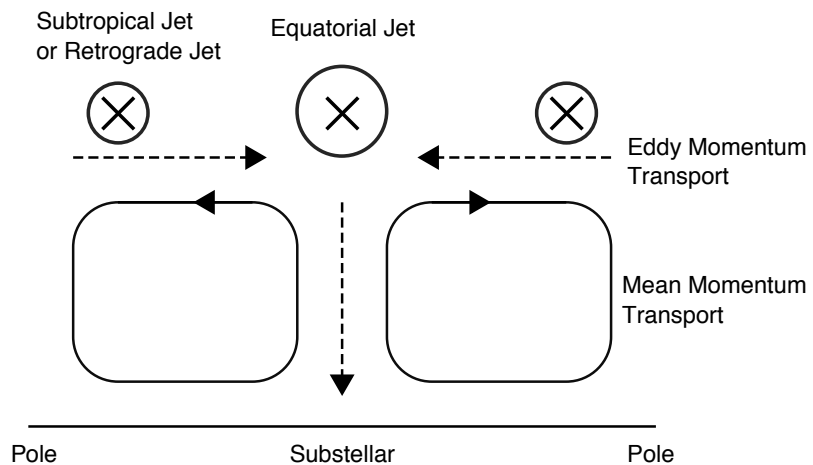


Figure 3.5: The Giersch-Rossow-Williams (GRW) mechanism (Read and Lebonnois, 2018), applied to the atmosphere of a tidally locked terrestrial planet. The solid line shows the mean momentum transport, which produces subtropical jets at high latitudes. The dashed lines show the horizontal and vertical momentum transports, which accelerate and decelerate the equatorial superrotation respectively.

eastward flow at all latitudes, as the due to the westward acceleration at high latitudes in Figure 3.4 is opposed by the eastward acceleration from the meridional circulation. Instead of requiring westward flow at high latitudes to balance the eastward flow at the equator, this mechanism requires subrotating flow at high latitudes to balance the superrotating flow at the equator – but, the subrotating flow can still be eastward.

The idealised GRW mechanism in Figure 3.5 assumes that the meridional circulation has the same zonal-mean effect on a tidally locked planet as on an asynchronously rotating planet like Venus. This ignores the longitudinal variation in this circulation due to the longitudinal variation in the equator-pole temperature gradient. In reality, the meridional circulation will be strongest at the substellar longitude, and negligible or even reversed on the night-side (Charnay et al., 2015). However, I will show that in the linear limit only the zonal mean of the meridional circulation is relevant to the momentum transport and jet formation discussed above.

Held and Hou (1980) show that the properties of the meridional circulation – zonal and meridional velocities, meridional momentum flux etc. – are linear with

response to the forcing. This holds separately at every longitude. The linearity of any property  $X$  with respect to the forcing  $Q(\phi, \lambda)$  means that for axisymmetric forcing, the zonal mean of  $X$  has the property:

$$\bar{X} \sim \bar{Q} = Q_0 \cos \phi. \quad (3.13)$$

For the same forcing on a tidally locked planet, the forcing is  $Q(\phi, \lambda) = Q_0 \cos \phi \sin \lambda$  on the day-side, plus a uniform relaxation on the night-side. So, the zonal mean is:

$$\bar{X} \sim \bar{Q} = Q_0 \cos \phi \overline{\sin \lambda}, \quad (3.14)$$

where the mean of the  $\sin \lambda$  is only taken over the day-side, giving:

$$\bar{X} \sim Q_0 \cos \phi, \quad (3.15)$$

The zonal mean of the meridional circulation therefore depends on the zonal mean of the forcing, when the local meridional circulation depends linearly on the local forcing. It is therefore possible to consider the zonal-mean effect of the meridional circulation on a tidally locked planet as entirely due to the wave-0 (zonal mean) component of the forcing. It is possible that non-linear effects from high forcing magnitudes or interactions with the zonal flow will make this assumption invalid.

### 3.2.2 Demonstration in a Linear Shallow-Water Model

This section demonstrates the GRW mechanism on a tidally locked planet in a modified version of the linear shallow-water model of [Showman and Polvani \(2011\)](#). The model is modified by adding a zonally uniform meridional velocity  $\bar{V}(y) = V_0 \sin y / y_0 e^{-y^2/y_0^2}$  to represent the poleward branches of the meridional circulation.

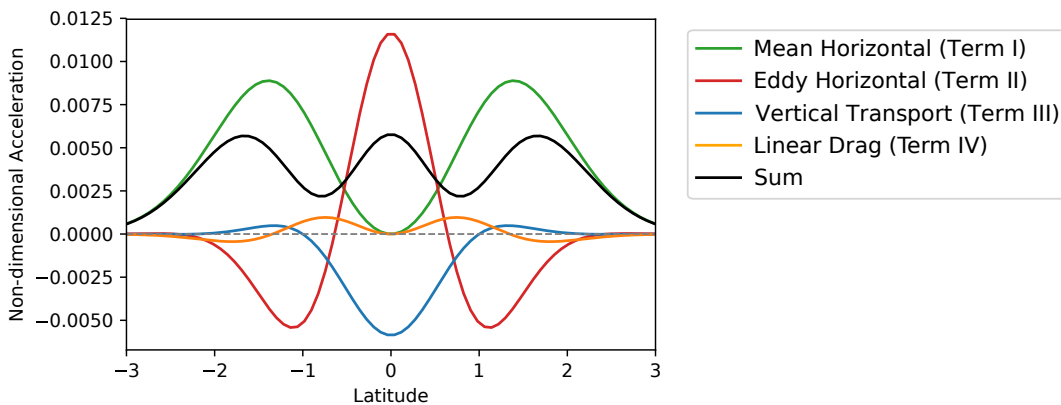


Figure 3.6: Acceleration terms in the zonal-mean zonal momentum equation (Equation 3.11), with an imposed uniform zonal-mean meridional velocity  $\bar{V}(y) = V_0 \sin y / y_0 e^{-y^2/y_0^2}$ , showing prograde westerly acceleration at all latitudes.

The meridional scale is  $y_0 = \sqrt{2}$  as before and in [Matsuno \(1966\)](#), and the scale of the velocity is  $V_0 = 0.02$ , chosen to produce an appropriate acceleration magnitude for this demonstration.

The imposed meridional velocity affects Term I in Equation 3.11, producing a westerly acceleration at high latitudes around the peak of the imposed meridional flow  $\bar{V}(y)$ . This opposes the easterly acceleration due to horizontal momentum transport from stationary eddies in the previous linear model, producing westerly prograde acceleration at all latitudes if the meridional velocity is large enough. In the GRW mechanism, this reflects the fact that the equatorward momentum transport from stationary eddies is moving momentum from a region that is already accelerated eastward by the meridional circulation.

So, rather than requiring easterly flow above a certain latitude as in the linear model of [Showman and Polvani \(2011\)](#), this model requires sub-rotating flow above a certain latitude – but, the flow can still be eastward. Next, I will use a non-linear shallow-water model and a GCM to demonstrate the mechanism without needing to impose the meridional circulation, as it will emerge naturally from the forcing in the models.

### 3.3 Non-Linear Model of the GRW Mechanism

This section demonstrates the GRW mechanism in a non-linear time-stepped shallow-water model. The meridional circulation and the acceleration at high latitudes will emerge naturally from the forcing field, unlike in the linear model where the meridional velocity was imposed. I will show that the equilibrium zonal flow is governed by the balance of momentum fluxes predicted by the GRW mechanism.

#### 3.3.1 Non-Linear Shallow-Water Model

The GFDL Spectral Dynamical Core<sup>1</sup> solves the equations describing the fluid dynamics of a model atmosphere by representing the solution as a series of spherical harmonic functions (Polvani et al., 2004). In this section, it is configured to solve the non-linear shallow-water equations in a single layer (Showman and Polvani, 2011). The non-linear shallow-water equations in this model<sup>2</sup> retain the terms that are discarded by the linear shallow-water equations in the previous section. The model is forced by relaxation to a radiative equilibrium height field  $h_{eq}$ , where a tendency  $\Delta h$  is applied to the height field  $h$  at every timestep:

$$\Delta h = \Delta t(h - h_{eq})/\tau_{rad}, \quad (3.16)$$

where  $\Delta t$  is the timestep and  $\tau_{rad}$  is the thermal damping timescale. The only other forcing is the correction  $R$  to the zonal momentum (Shell and Held, 2004). The model could apply dynamical damping to the velocity fields of the shallow-water layer, but I chose not to use this damping in order to match the GCM simulations better. Section 3.4 will show that dynamical damping is not part of the balance of forces on the jet in the GCM.

---

<sup>1</sup>[gfdl.noaa.gov/idealized-spectral-models-quickstart/](http://gfdl.noaa.gov/idealized-spectral-models-quickstart/)

<sup>2</sup>[gfdl.noaa.gov/wp-content/uploads/files/user\\_files/pjp/shallow.pdf](http://gfdl.noaa.gov/wp-content/uploads/files/user_files/pjp/shallow.pdf)

I ran three simulations in the model which were forced by relaxation to different radiative equilibrium height fields  $h_{eq}$ . The models were run for 100 days, and the results taken over the last 10 days after a steady state had formed. All the tests in this section have  $h_o = 10 \text{ km}$ ,  $\Delta h = 1 \text{ km}$ , and a thermal damping time  $\tau_{rad} = 0.1 \text{ days}$ . Figures 3.7, 3.8, and 3.9 show the height fields and zonal-mean zonal and meridional velocities of each test.

### 3.3.2 Test A: Sinusoidal Forcing

Test A was forced by relaxation to a radiative-equilibrium height field that varies sinusoidally with longitude:

$$h_{eq} = h_o + \Delta h \sin \lambda \cos \phi. \quad (3.17)$$

This is the same as the forcing field used in the linear model of [Matsuno \(1966\)](#) and the non-linear model of [Showman and Polvani \(2011\)](#). It is a simple representation of day-side heating and night-side cooling, but does not produce a mean meridional circulation as it has zero zonal mean.

Figure 3.7a shows the resulting height field in equilibrium, which is similar to the non-linear simulations in Figure 8 of [Showman and Polvani \(2011\)](#). The model is forced in the same way as the linear response in Figure 3.2, but the non-linearity produces a day-night asymmetry in this case. The stationary waves created by the forcing transport eastward momentum towards the equator, producing an eastward equatorial jet and westward flow at high latitudes shown in Figure 3.7b. Note that there is some meridional velocity due to the small day-night asymmetry from the non-linear terms, but it is not strong enough to produce eastward subtropical jets. The stationary waves are partly shifted eastwards by this zonal-mean zonal velocity. As shown in Section 3.1, the sinusoidal forcing must produce westward flow at high

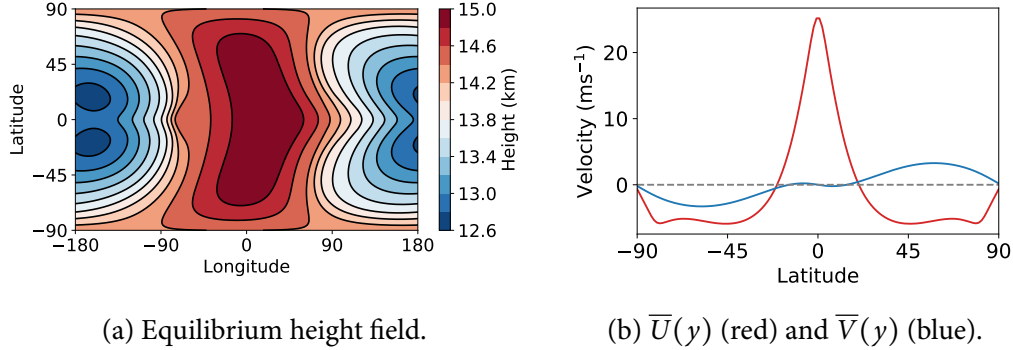


Figure 3.7: Test A with sinusoidal day-night forcing, showing the equilibrium height field, the zonal-mean zonal velocity  $\bar{U}(y)$  (red), and the zonal-mean meridional velocity  $\bar{V}(y)$  (blue). The height field shows the stationary wave response that produces an eastward equatorial jet and westward flow at high latitudes.

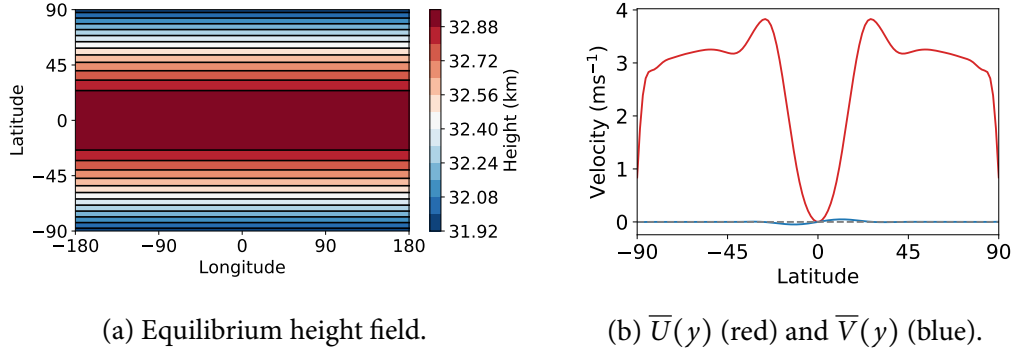


Figure 3.8: Test B with axisymmetric forcing, showing the axisymmetric height field and the meridional velocity that produces eastward subtropical jets.

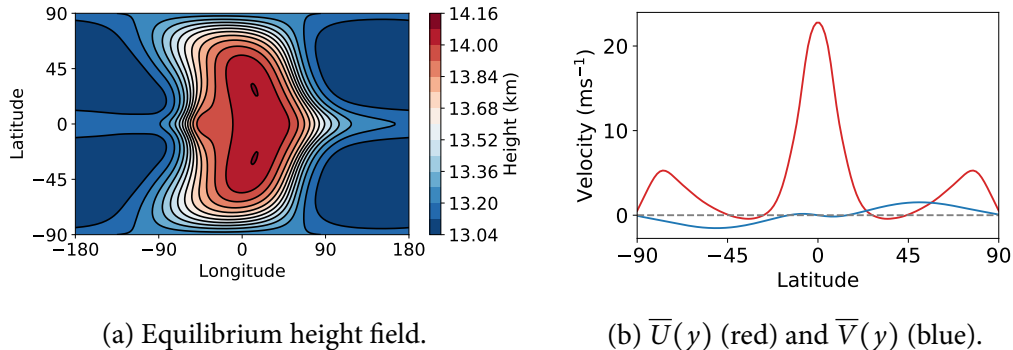


Figure 3.9: Test C with realistic forcing, showing the stationary wave response and the meridional velocity, which together produce eastward flow at all latitudes by the GRW mechanism.

latitudes to balance the eastward flow at the equator, so is inconsistent with GCM simulations that can have eastward flow at all latitudes at the level of the jet ([Showman et al., 2015](#); [Kataria et al., 2015](#); [Pierrehumbert and Hammond, 2019](#)).

### 3.3.3 Test B: Axisymmetric Forcing

The GRW mechanism requires a meridional circulation that produces eastward flow at the level of the jet at high latitudes. [Shell and Held \(2004\)](#) model the meridional circulation of the Earth in a non-linear shallow-water model with an axisymmetric forcing with an equator-pole gradient. This produces a meridional velocity and eastward subtropical jets. The single-layer model does not represent the lower branch of the circulation, which would produce westward zonal flow. This will be represented in the GCM simulations later, where the westward surface flow will be a source of eastward atmosphere angular momentum due to Rayleigh drag.

Test B uses a simplified axisymmetric field to qualitatively reproduce the Earth-like circulation in [Shell and Held \(2004\)](#), and to show that a forcing field with a non-zero zonal mean produces an acceleration at high latitudes. The axisymmetric field is:

$$h_{eq} = h_o + \Delta h \cos \phi / \pi. \quad (3.18)$$

Figure 3.8a shows the axisymmetric height field in equilibrium, with a small equator-pole height gradient due to the forcing. The height gradient produces the meridional velocity shown in Figure 3.8b, that results in eastward zonal subtropical jets. Note that there is zero zonal flow at the equator. The next test will show how these subtropical jets are modified by equatorward momentum transport from the stationary wave forcing in Test A.

### 3.3.4 Test C: Realistic Forcing

Test C uses a more realistic forcing field to show how the GRW mechanism can produce eastward flow at all latitudes. The forcing field in Test A is not realistic because the night-side should cool uniformly, rather than preferentially at the antistellar point. A more realistic radiative-equilibrium field is:

$$h_{eq} = \begin{cases} h_o + \Delta h \sin \lambda \cos \phi & (|\lambda| < \pi/2) \\ h_o & (|\lambda| > \pi/2) \end{cases} \quad (3.19)$$

[Perez-Becker and Showman \(2013\)](#) used a similar height field in a model of a tidally locked planetary atmosphere. Unlike the field in Test A, the field in Test C has a non-zero zonal mean. The zonal mean of this forcing is the same as the axisymmetric forcing in Test B, so it should produce a similar meridional circulation. The day-side component of this realistic field is the same as the day-side of Test A, so it should give similar stationary waves and equatorward momentum transport. Together, these components drive the GRW mechanism – the zonal-mean forcing field produces eastward zonal flow at high latitudes, then the stationary waves transport eastward momentum towards the equator. The forcing fields of Tests A and B are essentially the lowest-order Fourier components of Test C, where Test B is the zeroth-order component and Test A is the first-order component.

Figure 3.9a shows the equilibrium height field of Test C, which is similar to the height field of Test A. The stationary waves are weaker on the night-side than the day-side, which may be due to the uniform forcing on the night-side. Figure 3.9b shows the key result of this section – eastward zonal flow at all latitudes, as predicted by the GRW mechanism. This is a result of the meridional circulation producing acceleration at high latitudes, which is too strong to be reversed by the equatorward momentum transport that creates the equatorial jet.

The GRW mechanism modifies the requirement of [Showman and Polvani \(2011\)](#) of westward flow at high latitudes to a requirement of subrotating flow at high latitudes (see 2.3.2 for the definition of subrotation). The next section will investigate the balance of sources of acceleration at different latitudes in Test C.

### 3.3.5 Equilibrium Zonal Flow

The mechanism in Figure 3.5 predicts the balance of momentum fluxes that determine the equilibrium state of the zonal flow. At the equator, the horizontal momentum transport from the stationary waves should balance the vertical momentum transport from rising and subsiding air at the substellar and antistellar points. At high latitudes, the horizontal momentum transport from the stationary waves should be balanced by the eastward acceleration of the poleward branch of the meridional circulation. This section will test this prediction in the non-linear shallow-water model.

The zonal-mean momentum equation in a spherical geometry is ([Showman and Polvani, 2011](#)):

$$\frac{\partial \bar{u}}{\partial t} = \underbrace{\bar{v}^* \left[ f - \frac{1}{a \cos \phi} \frac{\partial (\bar{u} \cos \phi)}{\partial \phi} \right]}_{\text{I}} - \underbrace{\frac{1}{h a \cos^2 \phi} \frac{\partial}{\partial \phi} \left[ (\bar{h} v)' u' \cos^2 \phi \right]}_{\text{II}} + \underbrace{\left[ \frac{1}{h} \bar{u}' Q' + \bar{R}_u^* \right]}_{\text{III}} - \underbrace{\frac{\bar{u}^*}{\tau_{\text{drag}}} - \frac{1}{h} \frac{\partial (\bar{h}' u')}{\partial t}}_{\text{IV}}, \quad (3.20)$$

where  $\phi$  is longitude, and all other variables are the same as before. Figure 3.10 shows each of these terms for the steady-state flow in Test C. The “Mean horizontal” term is Term I, which produces an acceleration at high latitudes due to the mean meridional velocity. This is primarily balanced by the “Eddy Horizontal” flux of Term II, which produces a westward acceleration at high latitudes as it transports eastward momentum towards the equator. This is the balance predicted by Figure 3.5 and

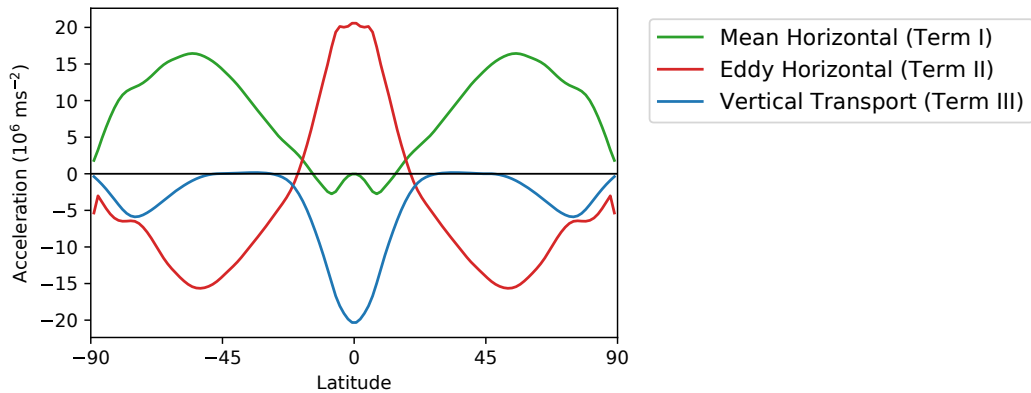


Figure 3.10: The terms in the zonal-mean zonal momentum equation (Equation 3.20) for Test C with realistic forcing in the non-linear shallow-water model, showing how equilibrium is achieved at the equator and at high latitudes. Note the same balance of forces as in Figures 3.6 and 3.18.

shown in the linear model in Section 3.2.2. There is also a westward acceleration at high latitudes from the “Vertical Transport” flux of Term III, as the eastward flow subsides in the descending branch of the meridional circulation. At the equator, the balance is between eastward acceleration due to the “Eddy Horizontal” transport from the stationary waves, and westward acceleration due to the “Vertical Transport” term discussed in Section 3.1. Term I is zero at the equator as there is zero meridional velocity. This agrees with the mechanism in Figure 3.5 and Section 3.2.2.

These non-linear shallow-water simulations have shown how the sinusoidal day-night forcing produces an equatorward momentum transport, how a non-zero zonal-mean forcing produces a meridional circulation, and how a realistic forcing combines these processes to drive the GRW mechanism. The realistic forcing field in Test C produces eastward flow at all latitudes, matching the GCM simulations that could not be explained by the model with sinusoidal day-night forcing. The balance of momentum fluxes at the equator and at high latitudes matched the balance predicted by the GRW mechanism. In the next section, I will show this is also the case in idealised GCM simulations of the atmosphere of a tidally locked planet.

### 3.4 GCM Simulations of the GRW Mechanism

This section shows the formation of zonal flow in the GCM Exo-FMS. I will compare an idealised simulation of a tidally locked planet to a simulation of an asynchronously rotating planet, and show that the balance of momentum fluxes in the GCM is same as the shallow-water models in the previous section. The next section will use this mechanism to predict the scaling behaviour of the zonal flow in a suite of tests in the non-linear shallow-water model and the GCM.

Test 1 is a tidally locked planet with a pure  $N_2$  atmosphere with radius  $1.0 R_E$ , rotation rate  $\Omega_E/10$ , surface pressure 1 bar, longwave optical thickness 1.0, shortwave optical thickness 0.0, and instellation  $1000 \text{ W m}^{-2}$ . This test is an idealised, general example of a tidally locked terrestrial planet orbiting an M-dwarf, using Exo-FMS with semi-grey radiative transfer and dry convective adjustment.

Figure 3.11a shows the equilibrium global circulation of Test 1, time-averaged from 1000 to 2000 days of the simulation. The global temperature and wind fields show the typical superrotating jet and hot-spot shift seen on tidally locked planets ([Showman et al., 2012](#); [Pierrehumbert and Hammond, 2019](#)). The zonal-mean zonal wind is dominated by a single equatorial jet, which is shown in Chapter 4 to produce the hot-spot shift by shifting the stationary planetary waves eastward. Note that there is prograde eastward flow at all latitudes of the jet in this test, which is the situation that this chapter aims to explain.

Test 2 is an asynchronously rotating planet with otherwise the same properties as Test 1. Its instellation is zonally uniform but has the same zonal-mean instellation as Test 1. I will show that this produces the same meridional circulation on the first day of the test when the response to forcing is small and linear. Figure 3.12 shows the global circulation of the equilibrium state of Test 2, time-averaged from 1000 to 2000 days of the simulation. This atmosphere has an zonally uniform temperature field,

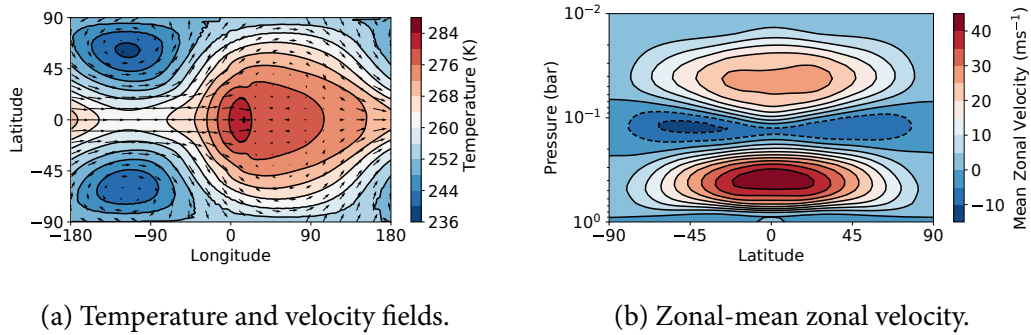


Figure 3.11: The global circulation of Test 1, time-averaged from 1000 to 2000 days of the simulation. The temperature field is at the half-surface pressure level. This is a typical tidally locked Earth-sized planet, with prograde zonal flow at all latitudes at the level of maximum jet flow.

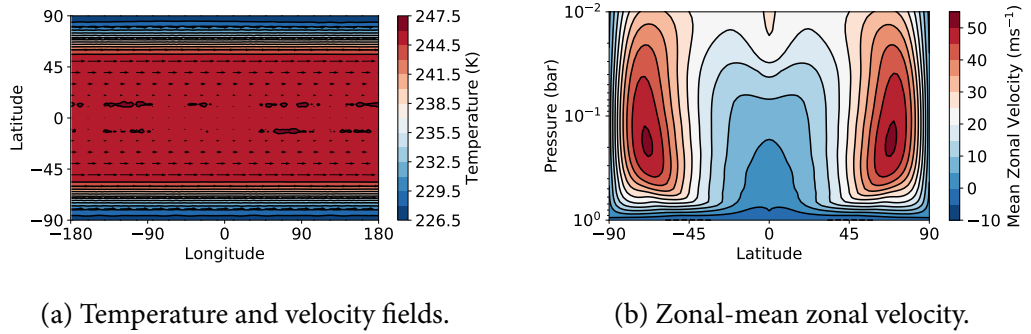


Figure 3.12: The global circulation of Test 2, time-averaged from 1000 to 2000 days of the simulation. The temperature field is at the half-surface pressure level. This is an idealised asynchronously rotating Earth-sized planet, with subtropical jets formed by the mean meridional circulation.

and two subtropical jets produced by its meridional circulation. Its “Hadley” cells are global due to its 10 day rotation period, unlike the more rapidly rotating Earth with its multiple cells.

These two tests will show how the meridional circulation on a tidally locked planet produces subtropical jets before the stationary waves from the day-night forcing produce equatorial acceleration, as described by the GRW mechanism. [Norton \(2006\)](#) used similar simulations to these two tests to show the formation of superrotation by tropical heating on the Earth.

### 3.4.1 Initial Meridional Circulation

Section 3.2.1 suggested that the meridional circulation on a tidally locked planet primarily depends on the zonal mean of the instellation. This means that the longitudinal variation of the instellation and circulation does not greatly affect the GRW mechanism. Figure 3.13 shows that this is true for the early stages of Tests 1 and 2, when the response to forcing is small and linear. The first column shows the zonal velocity in the first day at the surface of each test, where Test 1 has diverging flow from the substellar point and Test 2 has weak surface westerlies forming as part of a meridional circulation.

The second column shows the zonal-mean zonal velocity on the first day. The two tests have almost exactly the same zonal-mean zonal velocity, despite their different longitudinal variation. The third column shows that they also have almost the same streamfunction. This supports the argument in Section 3.2.1 that only the zonal mean of the forcing (the same in Tests 1 and 2) affects the zonal-mean meridional circulation in the linear limit of weak forcing. The meridional circulation only enters the zonal-mean zonal momentum equation (Showman and Polvani, 2011) as a zonal-mean quantity, so the GRW mechanism can be applied to the zonal-mean circulation without considering the actual longitudinal variation of the instellation. In reality, as each test spins up the assumption of linearity will become less accurate as the perturbations increase and the zonal flow affects the meridional circulation.

These tests support the use of the GRW mechanism to explain the formation of zonal flow on tidally locked planets. They show that the meridional circulation primarily affects the zonal flow through its zonal mean only. The next section will show how the equatorward momentum transport on tidally locked planets modifies the subtropical jets and produces equatorial superrotation.

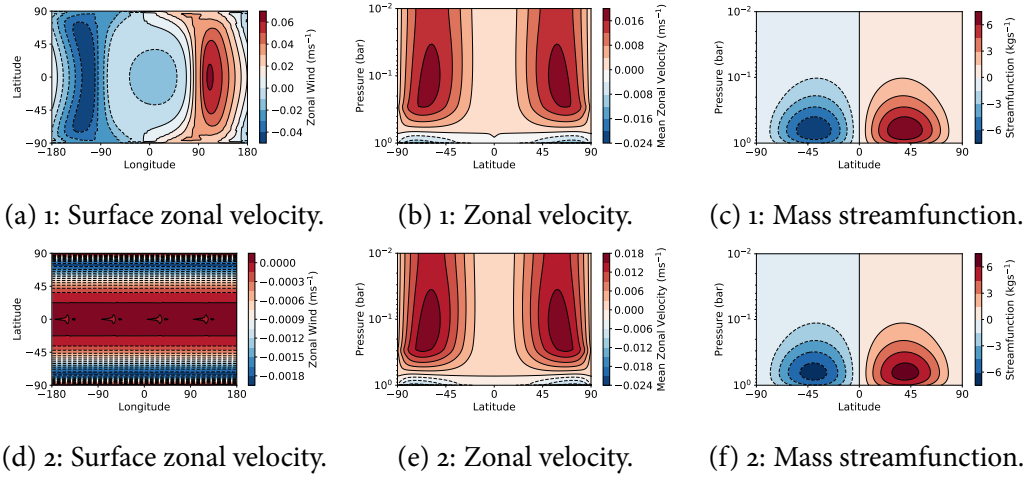


Figure 3.13: Time-mean results from Tests 1 and 2, for the first day after initialisation from rest. The top row shows the tidally locked planet Test 1, and the bottom row shows Test 2, a planet with axisymmetric forcing with the same zonal mean. The zonal mean zonal velocity and mean mass streamfunction are the same in both cases, despite the large differences in the longitudinal distribution of the forcing.

### 3.4.2 Demonstration of GRW Mechanism

This section shows the formation of zonal flow in Tests 1 and 2, demonstrating how the GRW mechanism adds angular momentum to the atmosphere in Test 1 and creates eastward flow at all latitudes. The total atmospheric angular momentum is (Lebonnois et al., 2012):

$$M = \int_V ua \cos \theta dm \quad (3.21)$$

where  $\int_V$  is the integral of mass over the whole atmosphere,  $u$  is the local zonal velocity,  $a$  is the planetary radius, and  $\theta$  is the latitude.

Figure 3.14a shows the total atmospheric angular momentum in Test 1 as it spins up from rest. The only source or sink of angular momentum apart from numerical error is the linear Rayleigh drag applied to the winds in the boundary layer near the surface. It gains angular momentum as the surface drags the winds in the boundary layer, then reaches equilibrium when there is sufficient eastward wind and westward torque

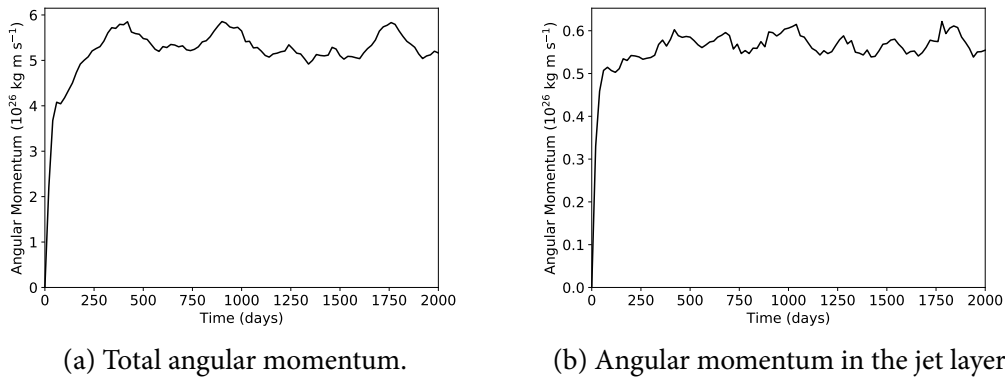


Figure 3.14: The spin-up in Test 1 of angular momentum globally and at the pressure level where the jet is strongest, showing how both regions gain momentum over time then equilibrate.

for no net effect. The total angular momentum varies over a period of hundreds of days, with fluctuations that are small compared to the large variability in the angular momentum of similar simulations of superrotation on Venus ([Lebonnois et al., 2012](#)).

Figure 3.14b shows the angular momentum in Test 1 in the model level of the maximum zonal-mean zonal flow. The angular momentum in this level increases as the model spins up, then reaches a positive value at equilibrium. This contradicts the shallow-water model in [Showman and Polvani \(2011\)](#) which loses angular momentum from the level of the jet. The positive net angular momentum is explained by the GRW mechanism, which transports angular momentum from the surface to the atmosphere, and to the upper branch of the meridional circulation.

Figures 3.15 and 3.16 show the development of the zonal flow in Tests 1 and 2. Figure 3.16 shows the evolution of the flow in Test 2, where subtropical jets form immediately due to the mean meridional circulation, then strengthen and reach equilibrium. Figure 3.15 shows that the same subtropical jets form initially in Test 1, but then the stationary waves transport angular momentum towards the equator ([Showman and Polvani, 2011](#)). Test 1 reaches an equilibrium state with a single equatorial jet and eastward flow at high latitudes due to acceleration from the meridional circulation.

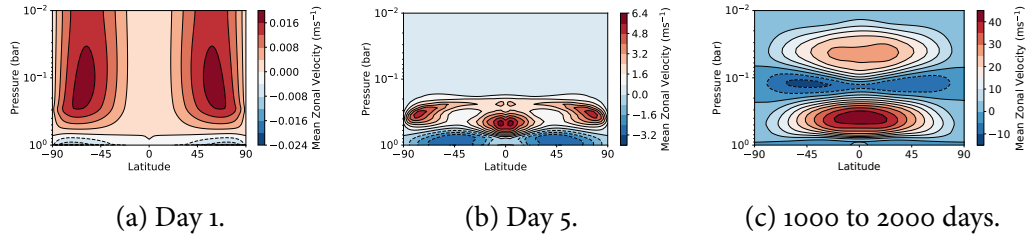


Figure 3.15: The zonal-mean zonal velocity of the tidally locked planet in Test 1 as it spins up from rest, forming subtropical jets before the equatorward momentum transport produces the equatorial jet. The time-mean fields on day 1, on day 5, and from day 1000 to 2000 are plotted.

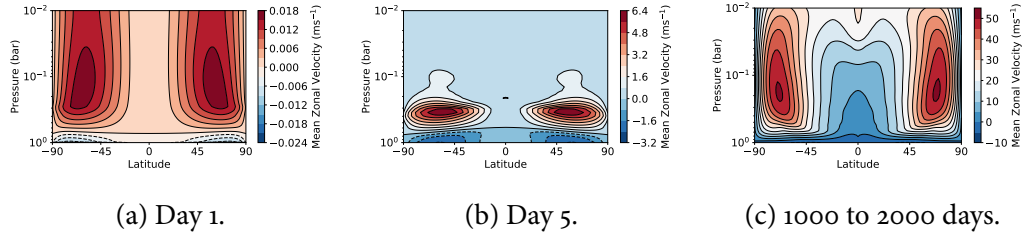


Figure 3.16: The zonal-mean zonal velocity of the axisymmetrically forced planet in Test 2 as it spins up from rest, forming subtropical jets. The time-mean fields on day 1, on day 5, and from day 1000 to 2000 are plotted.

### 3.4.3 Zonal Momentum Fluxes

This section shows that the GRW mechanism explains the equilibrium zonal momentum budget in Test 1. The steady-state zonal-mean momentum equation is (Lutsko, 2018):

$$\frac{\partial \bar{u}}{\partial t} = f[\bar{v}] - \underbrace{\frac{[\bar{v}]}{a \cos \phi} \frac{\partial}{\partial \phi}([\bar{u}] \cos \phi)}_{Ia} - \underbrace{[\bar{w}] \frac{\partial [\bar{u}]}{\partial p}}_{Ib} - \underbrace{\frac{1}{a \cos^2 \phi} \frac{\partial}{\partial \phi}([\bar{u}' \bar{v}'] \cos^2 \phi)}_{IIa} - \underbrace{\frac{\partial}{\partial p} [\bar{u}' \bar{w}']}_{IIb} + \underbrace{[\bar{F}_x]}_{III} \quad (3.22)$$

where  $\omega$  is the vertical velocity, and all other variables are the same as before.

Terms Ia and Ib are the mean horizontal and vertical momentum transport due to the mean meridional circulation. Term IIa is the eddy horizontal momentum transport

from the stationary wave response to the stellar forcing, and Term IIb is the eddy vertical momentum transport due to vertical motion. This vertical motion is mostly due to air rising at the substellar point and subsiding on the night-side. Term III is the forcing applied to the zonal winds, which in this case is the Rayleigh drag in the boundary layer near the surface.

Figure 3.17 shows each of the momentum transport terms in Equation 3.22. Term Ia is plotted in Figure 3.17a, which shows how the mean meridional circulation produces an acceleration in the midlatitudes in its poleward branch and has no effect at the equator. There is a westward acceleration at the surface due to the lower branch of the mean meridional circulation. This produces the westward surface flow that results in an eastward torque on the atmosphere from the Rayleigh drag in the boundary layer.

Figure 3.17b shows Term Ib, where the primary effect is the ascending branch of the mean meridional circulation moving the equatorial jet upwards, as shown by the deceleration below the centre of the jet and the acceleration above the centre of the jet. This term has zero effect where there is zero vertical gradient in the mean zonal flow, so it does not affect the maximum zonal flow at the centre of the jet, and is not as important as the other terms to the equilibrium state.

Figure 3.17c plots Term IIa, and shows how the stationary waves excited by the stellar forcing transport eastward momentum horizontally towards the equator. This produces an acceleration at the equator and a deceleration at higher latitudes. Term IIb in Figure 3.17d shows how the vertical momentum transport decelerates the jet. It moves stationary air up on the day-side, reducing the specific westerly angular momentum of the jet. There is an additional deceleration on the jet from the subsiding air on the night-side moving eastward angular momentum down and out of the jet layer. This produces eastward flow at the surface, which results in a westward drag that opposes the eastward drag on the lower branch of the meridional circulation, resulting eventually in equilibrium.

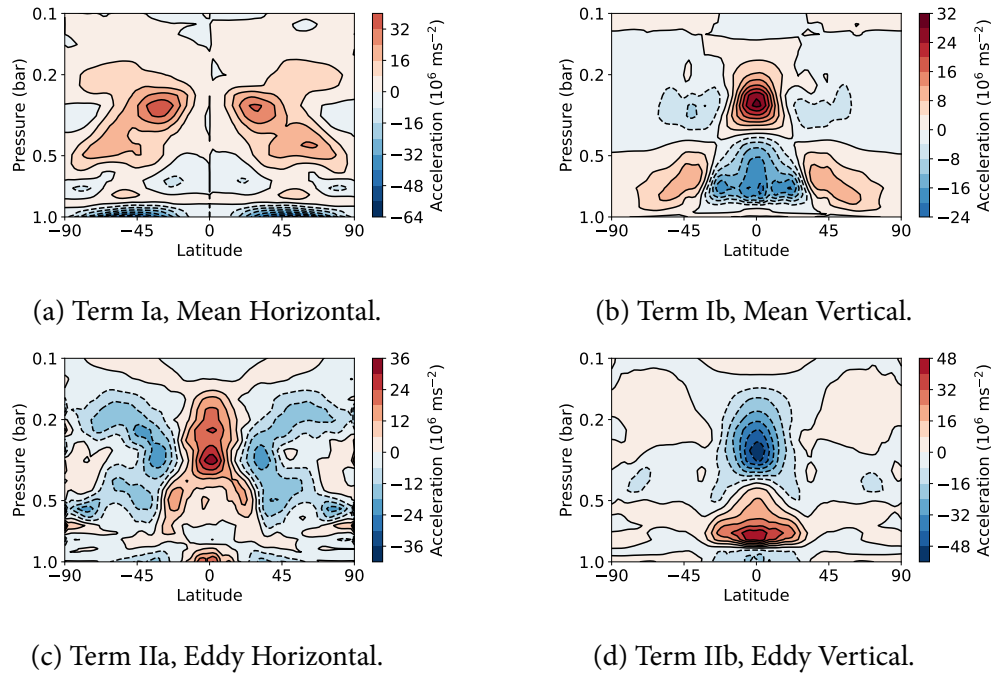


Figure 3.17: The sources of zonal acceleration in Equation 3.22, showing how different terms accelerate and decelerate zonal flow at the equator and at high latitudes. Figure 3.18 plots these terms at 0.3 bar.

Figure 3.18 shows each term in Figure 3.17 at 0.3 bar, near the centre of the jet. It shows that the Terms Ia and IIa balance at high latitudes, and that Term IIb balances Term IIa at the equator, as shown in the linear model in Figure 3.6. Terms Ia and IIa become weak at very high latitudes, unlike the shallow-water model in Figure 3.10 where both terms are strong almost until the pole. This is because the meridional circulation does not extend all the way to the pole in the GCM, unlike in the idealised shallow-water model. The balance of fluxes governing the equilibrium flow is still the same in both models.

The “Mean Vertical” acceleration of Term Ib is also different to the shallow-water models. It contributes to the eastward acceleration at the equator, opposing Term IIb. This appears to be different to the fluxes in the shallow-water models, where the mean vertical acceleration has no effect. However, Figure 3.17b showed that the mean vertical acceleration has a negligible net effect on the strength of the jet, with

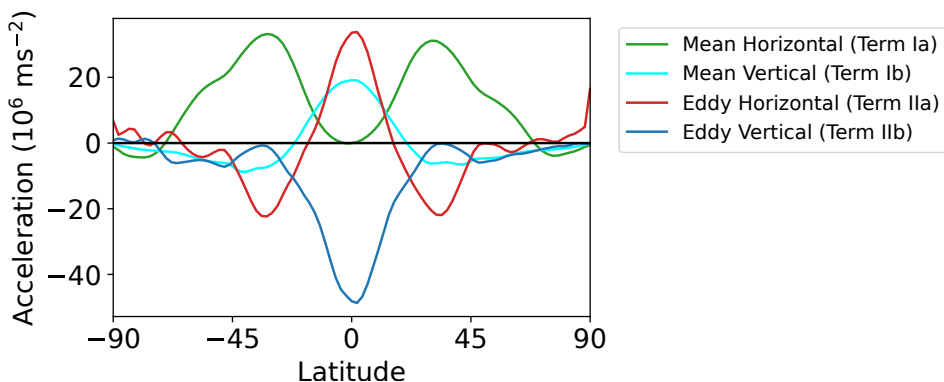


Figure 3.18: Acceleration terms in the zonal-mean zonal momentum equation at 0.3 bar in Test 1 in Exo-FMS, showing how Terms Ia and IIa in Equation 3.22 balance at high latitudes, and that Term IIb balances Terms IIa and Ib at the equator. This matches the shallow-water models in Figures 3.6 and 3.10, except for the presence of Term Ib, which is explained in the text.

an acceleration above its centre but a deceleration below its centre. This means that it has no net effect on the strength of the jet, so does not need to be considered when comparing to the single-layer shallow-water models. The balance of acceleration terms in Figure 3.18 for the GCM is therefore qualitatively the same as the balance of terms in Figure 3.10 for the non-linear shallow-water model, matching the GRW mechanism.

### 3.5 Scaling Behaviour of Zonal Jets on Tidally Locked Planets

In this section, I will use the ideas developed so far to predict how the strengths and positions of the zonal jets in the atmospheres of tidally locked planets could scale with planetary parameters. Perez-Becker and Showman (2013) use a similar non-linear model to derive scaling relations for the global height field and associated day-night contrast. This section will focus on the scaling behaviour of the strength and position of the jets formed on tidally locked planets.

### 3.5.1 Non-Linear Model Scaling Relations

Equation 3.20 shows how each source of acceleration scales with the planetary parameters. Term II drives the equatorial jet, suggesting that the jet speed should scale like  $\frac{1}{h} \frac{\partial}{\partial y} \left[ \overline{(hv)'u'} \right] \sim u'v' \sim Q^2\alpha^2$ . Term I in Equation 3.20 drives the subtropical jets, suggesting that they should scale like  $\bar{v}^* \left[ f - \frac{\partial \bar{u}}{\partial y} \right] \sim v'f \sim Q\alpha f$ .

Figure 3.19 shows the scaling of the zonal-mean equatorial and subtropical jet speeds with the forcing strength  $\delta h$ . Each test has the same parameters as Test C in Section 3.3, except for the magnitude of the forcing. The figure shows that for low forcing values, the equatorial jet does scale quadratically with the forcing (as identified by [Showman and Polvani \(2011\)](#)), and the subtropical jets scale linearly. For forcing values higher than  $\Delta h/h_o = 0.01$ , the jets increases more slowly than linearity, as non-linear effect become more important. For realistic forcing values of order 0.01 ([Showman and Polvani, 2011](#)), the jets still obey this linear scaling trend.

This predicts that increasing the forcing (instellation) on a tidally locked planet will increase both the equatorial and subtropical jet speeds, and will increase the equatorial jet speed relative to the subtropical jets. In addition, the equatorial acceleration comes at the expense of the subtropical jets due to the equatorward momentum transport, so for very strong forcing the subtropical jets may be replaced by easterly flow.

### 3.5.2 Qualitative GCM Scaling Relations

This section will qualitatively apply the scaling relations from the non-linear shallow-water model to a suite of GCM simulations. Figure 3.20 shows the zonal-mean zonal velocity of nine GCM simulations with different rotation rates and instellation values, adapted from [Pierrehumbert and Hammond \(2019\)](#). These tests have a range of zonal flow patterns, with one, two, or three jets of varying strengths and positions, which can be explained with the scaling relations of the previous section.

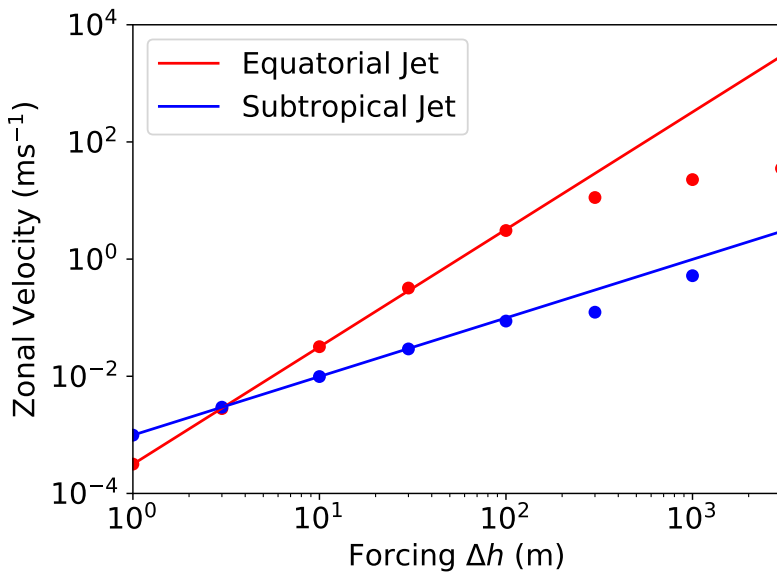


Figure 3.19: The equatorial and subtropical jet speeds in the non-linear shallow-water model, versus the magnitude  $Q = \delta h / h_o$  of the realistic forcing field in Test C, where  $h_o = 1 \times 10^4$  m. The lines show fits of the predicted quadratic scaling of the equatorial jet, and linear scaling of the subtropic jets.

Increasing the instellation in the GCM increases the forcing  $Q$ , and raises the damping rate  $\alpha$  due to the higher temperature. I showed previously that increasing the forcing  $Q$  and damping  $\alpha$  in the shallow-water model increases the strength of all the zonal jets, and increases the strength of the equatorial jet relative to the subtropical jets. This explains why the GCM tests with higher instellation have strong, single equatorial jets, with all the “hot” tests having one single jet centred on the equator. The “hot, 2 day” test has easterly flow at high latitudes, as the high forcing increases the prograde momentum transport towards the equator.

The GRW mechanism predicts that increasing the rotation rate of the planet should strengthen the subtropical jets, and move them to lower latitudes. This is confirmed by the GCM tests, and is shown most clearly by the “cold” cases, where increasing the rotation rate gives faster jets than are closer together. In the “hot” simulations, the subtropical jets merge with the equatorial jet and there appears to

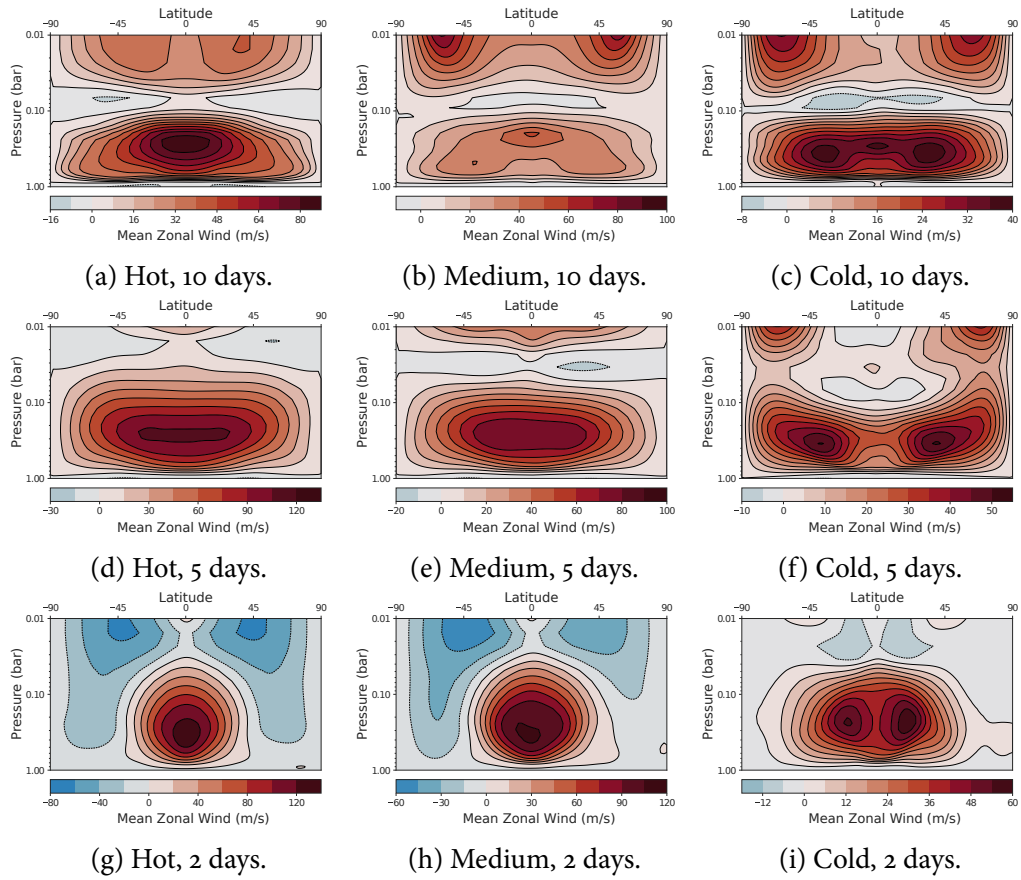


Figure 3.20: Time-mean zonal-mean zonal flow of a suite of tests in the GCM ExoFMS, showing how the equatorial and subtropical jet speeds and positions depend on instellation and rotation rate. Reproduced with data from [Pierrehumbert and Hammond \(2019\)](#).

only be one jet. The GRW mechanism therefore explains the qualitative behaviour of this suite of simulations, and provides an understanding of why GCM simulations of the atmospheres of tidally locked terrestrial planets can have one, two, or three zonal jets of varying strengths.

## 3.6 Discussion

This section discusses some complicating aspects of applying the GRW mechanism to real tidally locked planets. The GRW mechanism in Figure 3.5 assumes that the meridional circulation is global, transporting air from the equator to the pole. This

is not the case for a rapidly rotating planet like the Earth, which contains multiple cells of meridional circulation. If a tidally locked planet rotated rapidly enough to limit the meridional extent of these cells, the GRW mechanism might only operate below a certain latitude. This may be the case in the more rapidly rotating tests in Figure 3.5.2, where the subtropical jets are closer to the equator and there is easterly flow at high latitudes. However, these tests show that a global meridional circulation is not strictly necessary for the GRW mechanism to function. A limited meridional circulation still receives westerly angular momentum from the surface and conveys it to the jet layer. The subtropical jets will be closer to the equator, and the behaviour at high latitudes may be different.

The meridional circulation is more complicated on tidally locked gas giants like hot Jupiters, which do not have a surface to bound the meridional circulation and apply drag to its lower branch. [Heng et al. \(2011\)](#) and [Mendonça et al. \(2018\)](#) showed that the meridional circulation of a hot Jupiter has a direct Hadley-cell like circulation above a certain pressure level, with indirect cells below it, which is similar to some models of Venus ([Sugimoto et al., 2019](#)). The equatorial superrotation in these hot Jupiter simulations is still in the same region as the direct cells, so the GRW mechanism may still describe the formation of the zonal flow. Hot Jupiter simulations still often apply drag to their lower boundary ([Liu and Showman, 2013](#)), which could add angular momentum to the atmosphere and produce a meridional circulation. The deep atmosphere may fulfil the same role as a surface if there is no explicit bottom drag, providing a reservoir for retrograde flow deep down.

Finally, this chapter has not considered an important mechanism discussed in detail for hot Jupiters by [Showman et al. \(2015\)](#) – the formation of westerly midlatitude jets by baroclinic instability. This can transport enough westerly momentum away from the equator to reduce the strength of the equatorial jet, and even to reverse its direction. This could be added to the GRW mechanism as another source of horizontal

transport of zonal momentum in the layer of the jet. [Laraia and Schneider \(2015\)](#) considered a similar situation on non-tidally locked planets, estimating the effect of both equatorward momentum transport due to equatorial waves, and transport away from the equator due to baroclinic instability. This additional transport is only important for more rapidly rotating planets, and so is not important for planets such as those simulated earlier with 10 day periods. However, in a full consideration of the formation of zonal flow on tidally locked planets it cannot be ignored, especially for hot Jupiters or more rapidly rotating terrestrial planets. It may be possible to classify planets into different regimes, where either the meridional circulation, stationary wave forcing, or baroclinic instability dominates the formation of zonal jets ([Showman et al., 2015](#)).

## 3.7 Conclusions

This chapter has shown how the Gierasch-Rossow-Williams mechanism describes the formation of the zonal flow at all latitudes in the atmospheres of tidally locked terrestrial planets. I demonstrated this mechanism in a linear shallow-water model, a non-linear shallow-water model, and the GCM Exo-FMS. All these models predicted that equilibrium was produced by the same balance of sources of acceleration in the zonal-mean zonal momentum equations. This mechanism correctly predicted how the zonal flow at the equator and at high latitudes scaled with forcing in the non-linear shallow-water model. It also explained the qualitative scaling behaviour of the strength and position of the zonal jets formed in a suite of idealised GCM simulations.

Further work should consider the role of this mechanism in the formation of zonal flow in the atmospheres of hot Jupiters, which have observable features that depend on their zonal flow ([Showman et al., 2015](#)). The role of the surface drag in the GRW

mechanism suggests that the presence of drag in a hot Jupiter GCM may be vital to the form and strength of its equilibrium zonal flow (Cho et al., 2015). Understanding the formation process in detail would also help to understand the approximations that are possible in accurate simulations (Mayne et al., 2019), and to predict the scaling behaviour of observable features such as the jet speed or hot-spot shift (Zellem et al., 2014; Louden and Wheatley, 2015).

In conclusion, the GRW mechanism can explain the formation and equilibration of the zonal flow on terrestrial tidally locked planets. It allows for eastward flow at all latitudes, unlike the shallow-water model of Showman and Polvani (2011) that does not match some GCM simulations. The next chapter will investigate the effect of this zonal flow on the global circulation and observable temperature distribution of the atmospheres of tidally locked planets.



## CHAPTER 4

# *Wave-Mean Flow Interactions in Tidally Locked Atmospheres*

---

*Most of the results in this chapter are published in [Hammond and Pierrehumbert \(2018\)](#).*

Strong zonal eastward jets are seen in simulations of tidally locked planetary atmospheres, and their effects on the temperature distribution in the atmosphere have been observed on many planets ([Parmentier and Crossfield, 2017](#)). This chapter shows how a shallow-water model linearised around a zonal jet  $\bar{U}(y)$  reproduces the global circulation of simulated tidally locked planets. This zonal flow creates their distinctive global circulation pattern, and controls their temperature distribution. I will show that the eastward hot-spot shift, which has been observed on many planets, is due to a Doppler-shift of the stationary waves excited by the day-night forcing difference ([Tsai et al., 2014](#)).

Sections 4.1 and 4.3 will show how the zonal flow discussed in Chapter 3 affects the free and forced modes in the linear shallow-water model of [Showman and Polvani \(2011\)](#). In Section 4.3, I will linearise the shallow-water model about a shear zonal flow  $\bar{U}(y)$  and its associated geostrophic height perturbation  $\bar{H}(y)$ . This differs from [Showman and Polvani \(2011\)](#), who used zero background flow  $\bar{U}(y) = 0$  and a uniform background height  $\bar{H}(y) = H_0$ . It also differs from [Tsai et al. \(2014\)](#), who used

a uniform background flow  $\bar{U}(y) = U_0$  and a uniform background height  $\bar{H}(y) = H_0$ . Chapter 3 justifies the eastward flow  $\bar{U}(y)$  imposed at all latitudes, which would otherwise contradict the predicted acceleration in [Showman and Polvani \(2011\)](#).

In Section 4.4, I will construct the same linear model on a sphere rather than on a beta-plane, for direct comparison with GCM simulations and real planets. I will then use this model to predict how the observable features of the global circulation qualitatively scale with different planetary parameters. Finally, I will discuss the mechanism behind the observable ‘‘hot-spot shift’’ on tidally locked planets. I will conclude that the shallow-water model linearised about the jet  $\bar{U}(y)$  and its height perturbation  $\bar{H}(y)$ , matches the results of GCM simulations and explains the form of the global circulation and temperature distribution.

## 4.1 Linear Shallow-Water Model in Zonal Flow

Chapter 3 introduced the linear shallow-water equations and the stationary wave response to the day-night forcing on a tidally locked planet. This chapter shows how the zonal flow produced by this response affects the stationary waves themselves. In this section, I will linearise the equations about a uniform eastward zonal flow  $\bar{U}(y) = U_0$ , and show how the flow Doppler-shifts the maximum of the forced response eastwards ([Tsai et al., 2014](#)).

The linear shallow-water equations in zero background flow (as used in Section 3) are:

$$\begin{aligned} \frac{\partial u}{\partial t} - \beta y v + \frac{\partial h}{\partial x} &= 0, \\ \frac{\partial v}{\partial t} + \beta y u + \frac{\partial h}{\partial y} &= 0, \\ \frac{\partial h}{\partial t} + c^2 \left( \frac{\partial u}{\partial x} + \frac{\partial v}{\partial y} \right) &= Q(x, y). \end{aligned} \quad (4.1)$$

where  $u$  and  $v$  are the zonal and meridional velocities,  $h$  is the height, and  $c = \sqrt{gH}$

is the gravity wave speed (Matsuno, 1966). As before, these are non-dimensionalised with time scale  $\sqrt{1/c\beta}$  and length scale  $\sqrt{c/\beta}$ , and all quantities will be assumed to have the form  $f(y)e^{i(kx-\omega t)}$ .

Linearising about the background flow  $U(x, y) = U_o$ , as an approximation to a zonal equatorial jet, gives the following equations (Tsai et al., 2014):

$$\begin{aligned} \frac{\partial u}{\partial t} + U_o \frac{\partial u}{\partial x} - \beta y v + \frac{\partial h}{\partial x} &= 0, \\ \frac{\partial v}{\partial t} + U_o \frac{\partial v}{\partial x} + \beta y u + \frac{\partial h}{\partial y} &= 0, \\ \frac{\partial h}{\partial t} + U_o \frac{\partial h}{\partial x} + c^2 \left( \frac{\partial u}{\partial x} + \frac{\partial v}{\partial y} \right) &= Q(x, y). \end{aligned} \quad (4.2)$$

These correspond to Equation 4.8 in a moving frame, with the time derivative  $\partial/\partial t$  replaced by the material derivative  $\partial/\partial t + U_o \partial/\partial x$  (hence the Doppler shift analogy). With explicit damping  $\partial/\partial t = \alpha$  and zonal derivatives  $\partial/\partial x = ik_x$ , these become:

$$\begin{aligned} (\alpha_{dyn} + ik_x U_o)u - \beta y v + ik_x h &= 0, \\ (\alpha_{dyn} + ik_x U_o)v + \beta y u + \frac{\partial h}{\partial y} &= 0, \\ (\alpha_{rad} + ik_x U_o)h + c^2 ik_x u + \frac{\partial v}{\partial y} &= Q(x, y), \end{aligned} \quad (4.3)$$

for a forcing  $Q(x, y) = Q_o \sin(x) e^{-y^2/2}$ , and a uniform background flow  $\bar{U}(y) = U_o$ . Chapter 3 showed how the forced response  $\chi = (u, v, h)$  is a sum of the free modes  $\xi_m = (u_m, v_m, h_m)$ , weighted by coefficients  $a_m$ :

$$\chi = \sum a_m \xi_m. \quad (4.4)$$

The solutions are now the same as before, except that the complex coefficient  $a_m$  (which determines the position of each mode in the forced response) is affected by the background flow:

$$a_m = \frac{1}{\alpha - i(\omega_m - U_o k_x)} b_m. \quad (4.5)$$

As  $U_o$  increases, the imaginary part of the denominator increases. The relative magnitudes of the components of the denominator of  $a_m$  set the position of each mode  $m$ , as shown in Figure 4.1.

Figure 4.1a shows how for a large damping  $\alpha$ ,  $a_m$  is mostly real and positive, and the mode has its maximum close to the maximum of the forcing – at the substellar point. For a large background flow  $U_o$ , Figure 4.1c shows that  $a_m$  is mostly imaginary and positive, so the maximum of the mode is close to  $90^\circ$  – this gives the hot-spot shift later on. Figure 4.1b shows the standard forced solution of Matsuno (1966), with zero background flow and relatively weak damping. In this case, the eigenvalues of each mode sets the position of that mode – the lowest-order Rossby mode is close to  $-90^\circ$ , and the Kelvin mode is slightly to the east of the substellar point.

Equation 4.5 gives an estimate of the parameters needed for a significant eastward hot-spot shift. The denominator of  $a_m$  must have a positive imaginary part for the forced response to appear east of the substellar point. This imaginary part must also have a greater magnitude than the real part  $\alpha$ . So, for the system with  $\alpha = 0.2$ , and the dominant lowest-order Rossby mode having  $\omega_m \approx 0.254$ , an eastward hot-spot shift requires  $U_o > 0.254$  and  $U_o - 0.254 > 0.2$ . This means that a significant hot-spot shift requires a zonal flow of  $U_o$  with a non-dimensional magnitude  $\sim 1$ .

## 4.2 Free Modes in Shear Flow on the Beta-Plane

This section investigates the free modes of the shallow-water equations linearised about a shear background flow  $\bar{U}(y)$  and the associated geostrophically balanced height perturbation  $\bar{H}(y)$ . I will show how the flow affects these free modes, which will be important later in understanding the response to forcing in a shear flow.

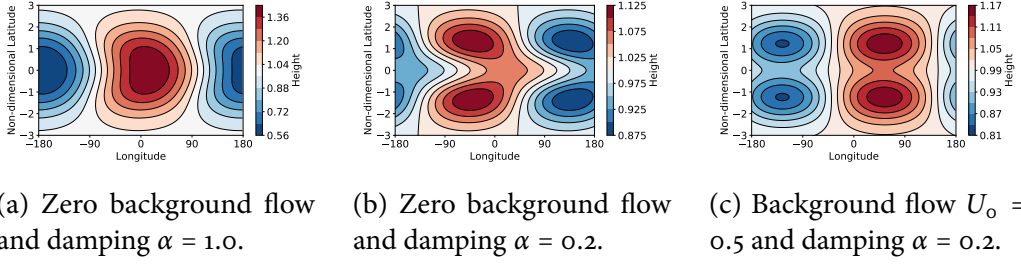


Figure 4.1: The linear responses to a forcing with magnitude  $Q_o = 1.0$  and  $\alpha = 0.2$  unless specified. The positions of the various modes depends on the terms in the denominator of Equation 4.5.

The shallow-water systems in this section have a forcing magnitude  $Q_o = 1$  and equal radiative and dynamical damping rates  $\alpha_{rad} = \alpha_{dyn} = 0.2$  ([Matsuno, 1966](#)). Section 4.3.2 will show the effect of varying these damping rates. The tests in this section show the effect of a zonal flow with a maximum non-dimensional speed between 0 and 1, which was shown previously to be the speed required for a significant zonal shift of the stationary waves. The value of  $Q_o = 1$  in the forcing  $Q(y) = Q_o \sin(x) e^{-y^2/2}$  was chosen to be the same as [Matsuno \(1966\)](#) and [Showman and Polvani \(2011\)](#), and also to produce stationary waves with similar magnitudes to the strength of the imposed zonal jet.

Section 4.1 showed how an exact solution for the response to a forcing can be written as a sum of the free modes of the system. An exact solution is not possible when the system is linearised about a background flow  $\bar{U}(y)$  and  $\bar{H}(y)$ , but it is still useful to interpret the approximate solution in terms of the fundamental free modes. I will write the free solutions to the shallow-water equations as complex functions of latitude  $A(y)$ , and the forced solutions as functions of both latitude and longitude in the form  $A(y) e^{i\delta(y)x}$ . The function  $\delta(y)$  determines the longitudinal structure of the forced response, and is equivalent to the phase shift  $(\omega_m - k_x \bar{U})$  derived earlier for a uniform background flow.

The response to forcing can still be interpreted as a sum of the free modes of

the system. The free modes of this system linearised about a shear flow have a different latitudinal structure  $u(y), v(y), h(y)$  and different eigenvalues  $\omega_m$ , so will have different longitudinal positions in the forced response. Linearised around the background flow  $\bar{U}(y)$  and height  $\bar{H}(y)$ , the shallow-water equations are:

$$\begin{aligned} \frac{\partial u}{\partial t} + \alpha_{dyn} u + \frac{\partial \bar{U}(y)u}{\partial x} + \left( \frac{\partial \bar{U}(y)}{\partial y} - y \right) v + \frac{\partial h}{\partial x} &= 0, \\ \frac{\partial v}{\partial t} + \alpha_{dyn} v + \frac{\partial \bar{U}(y)v}{\partial x} + yu + \frac{\partial h}{\partial y} &= 0, \\ \frac{\partial \bar{H}' u}{\partial x} + \bar{H}' \frac{\partial v}{\partial y} - y\bar{U}(y)v + \frac{\partial h}{\partial t} + \alpha_{rad} h + \frac{\partial \bar{U}(y)h}{\partial x} &= Q(y), \\ \bar{H}' &= 1 + \bar{H}(y). \end{aligned} \quad (4.6)$$

The free modes of Equation 4.6 are found by setting  $Q(y) = 0$  and  $\partial/\partial t = -i\omega$ , and writing  $u, v, h$  in the form  $A(y)e^{i(k_x x - \omega t)}$ . Casting the resulting equations in a matrix form gives:

$$\begin{pmatrix} \alpha_{dyn} + ik_x \bar{U}(y) & \frac{\partial \bar{U}(y)}{\partial y} - y & ik_x \\ y & \alpha_{dyn} + ik_x \bar{U}(y) & \frac{\partial}{\partial y} \\ ik_x \bar{H}' & -y\bar{U}(y) + \bar{H}' \frac{\partial}{\partial y} & \alpha_{rad} + k_x \bar{U}(y) \end{pmatrix} \begin{pmatrix} u \\ v \\ h \end{pmatrix} = i\omega \begin{pmatrix} u \\ v \\ h \end{pmatrix}, \quad (4.7)$$

$$\bar{H}' = 1 + \bar{H}(y).$$

The background state of  $\bar{U}(y)$  and  $\bar{H}(y)$  must satisfy Equation 4.6 by itself. On the beta-plane, this means that the shear flow  $\bar{U}(y)$  is geostrophically balanced by the height perturbation  $\bar{H}(y)$ . The second line of Equation 4.6 requires that for a background flow  $\bar{U}(y)$ , the background state is:

$$\begin{aligned} \bar{U}(y) &= U_0 e^{-y^2/2} \\ \bar{V}(y) &= 0 \\ \bar{H}(y) &= U_0 e^{-y^2/2} \end{aligned} \quad (4.8)$$

In this model, the perturbations in the forced system apply to a single shallow-water layer of height  $H_o$  (which is non-dimensionalised to unity). The vertically varying heating profile in a planetary atmosphere technically excites a continuum of vertical modes, each defining a shallow-water system of different  $H_o$ . However, Tsai et al. (2014) showed that almost all the energy is confined to the lowest-order vertical mode in this forced shallow-water system, so this approximation by a single layer is reasonable.

#### 4.2.1 Free Mode Eigenvalues

Appendix B describes the methods used to find the free modes of the shallow-water system defined by Equation 4.7 for a background flow  $\bar{U}(y) = U_o e^{-y^2/2}$  (Hammond and Pierrehumbert, 2018). Figure 4.2 shows the real parts of the eigenvalues of the lowest-order (i.e. largest magnitude) modes excited by the symmetric, stationary forcing. These are the free Kelvin mode and the symmetric free Rossby modes of Equation 4.7 (Matsuno, 1966). The value and sign of these eigenvalues determine the position of the free mode in the forced response, as discussed in Section 4.1.

As the magnitude  $U_o$  of the equatorial jet  $\bar{U}(y)$  increases in Figure 4.2, all the eigenvalues of the free modes become more positive. This corresponds to an eastward shift in their position in the forced response up to a maximum of  $90^\circ$  east, as in Equation 4.5. The Kelvin mode has a positive eigenvalue for  $U_o = 0$ , so is already east of the substellar point. This eigenvalue becomes larger as  $U_o$  increases, so the Kelvin mode moves further east in the forced response.

The Rossby modes of different order  $m$  shift by different amounts. Tsai et al. (2014) showed that in a uniform background flow, the  $n = 1$  Rossby mode is shifted eastwards towards  $90^\circ$ , producing the hot-spot shift (reproduced in Figure 4.1). In fact, Figure 4.2 shows that in this non-uniform flow  $\bar{U}(y)$ , the  $n = 1$  Rossby mode eigenvalue becomes less negative but does not become positive for  $U_o = 1.0$ . This

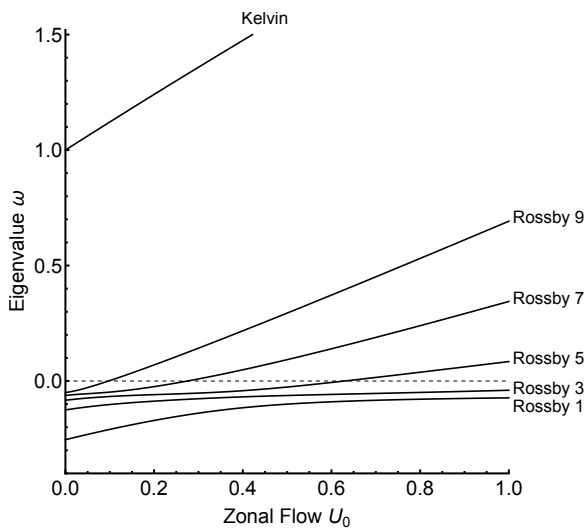


Figure 4.2: The eigenvalues of the free modes of Equation 4.7, showing how eastward flow makes the eigenvalues more positive, corresponding to an eastward shift in the response to forcing.

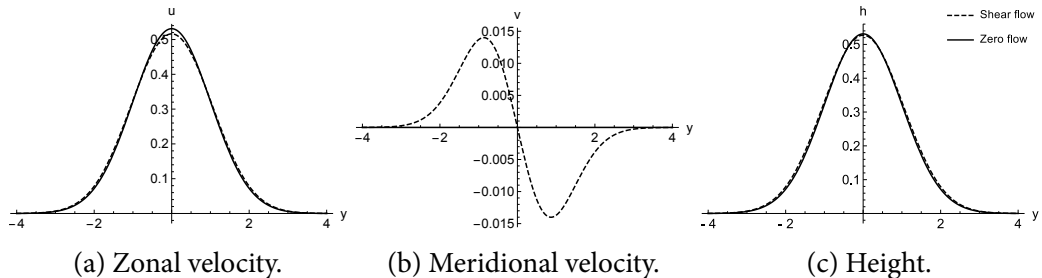


Figure 4.3: The meridional structure of the free Kelvin mode, with and without a background shear flow ([Hammond and Pierrehumbert, 2018](#)). The flow introduces a non-zero meridional velocity.

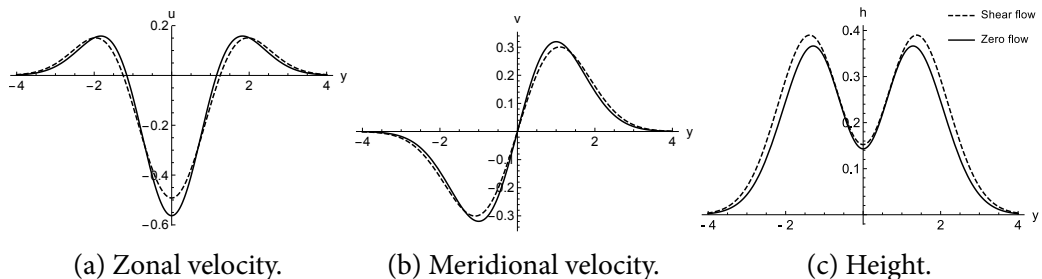


Figure 4.4: The meridional structure of the free Rossby mode, with and without a background shear flow ([Hammond and Pierrehumbert, 2018](#)). The shear affects the meridional structure, effectively changing the  $y$  coordinate ([Boyd, 1978](#)).

means that it is shifted east from its original position in the forced response, but is not shifted past the substellar point.

The higher order Rossby modes are shifted further past the substellar point by the flow  $\bar{U}(y)$ , as shown by their positive eigenvalues for high enough flow speed  $U_0$ . The modes of higher order are shifted further, but contribute less strongly to the forced response ([Matsuno, 1966](#)). Therefore, the response to forcing calculated below will be interpreted in terms of the free modes up to the  $n = 5$  symmetric Rossby mode, as the contribution of the higher-order modes is negligible.

The background shear flow also changes the latitudinal structure of each free mode. Figures 4.3 and 4.4 show the lowest-order free solutions of Equation 4.7. These Kelvin and Rossby modes are slightly different to the free modes in zero background flow ([Matsuno, 1966](#)). The shear flow changes these solutions by adding higher order meridional structure, as discussed in more detail in [Boyd \(1978\)](#). In summary, the free modes respond to a shear zonal flow in a qualitatively similar way to the uniform zonal flow in Section 4.1, but the details of their structure and shifts vary depending on the mode  $m$ .

### 4.2.2 Unstable Modes

The eigenvalues of the free modes of this system come in pairs, if there is no damping. They have equal and opposite positive and negative imaginary parts. The modes with positive imaginary parts will grow unstably ([Wang and Mitchell, 2014](#); [Ribstein et al., 2014](#)). For non-zero damping, the imaginary parts will become more negative, making some free modes stable for large enough damping.

Technically, these unstable modes mean that any linear initial value problem in this system is not well posed, as it will eventually be dominated by the most unstable modes rather than the stationary response discussed elsewhere. However, the non-linear shallow-water calculations and GCM simulations in other chapters show that

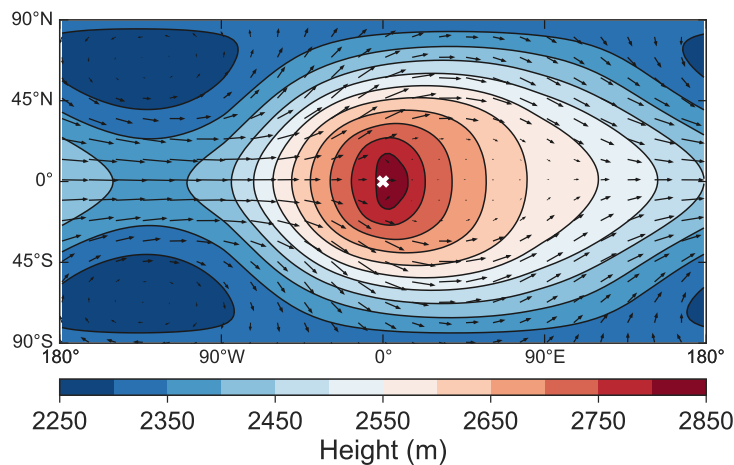


Figure 4.5: The time-mean height field from a simulation of a tidally locked planet in the GCM Exo-FMS, showing the typical eastward equatorial jet, shifted hot-spot, and night-side stationary Rossby waves.

the linear stationary response still appears to dominate. This suggests that in reality the unstable modes are strongly damped or reach equilibrium due to nonlinear effects. The free modes could cause time-variable behaviour in the atmospheres of tidally locked planets (Armstrong et al., 2017; Pierrehumbert and Hammond, 2019).

### 4.3 Forced Response in Shear Flow on the Beta-Plane

This section shows the effect of a background shear flow on the response to forcing in this linear model, which is the main result of this chapter. I will show the forced solutions with and without a background shear flow, discuss the form of the global circulation, and compare the shallow-water solutions to GCM simulations.

Figure 4.5 shows a GCM simulation of a tidally locked planet, with the features typical to such atmospheres. This planet is an idealised example of a terrestrial planet orbiting an M-dwarf, with radius  $1.0 R_E$  and orbital period of 10 Earth days. It has an  $N_2$  atmosphere with surface pressure 1 bar. In the semi-grey radiative transfer scheme, it has a longwave optical thickness of 1 and a shortwave optical thickness of 0. The large-scale features of the global circulation are not sensitive to these parameters, and

similar circulation patterns are seen in simulations of very different types of tidally locked planet (Showman et al., 2012; Heng and Showman, 2015).

#### 4.3.1 Response to Forcing

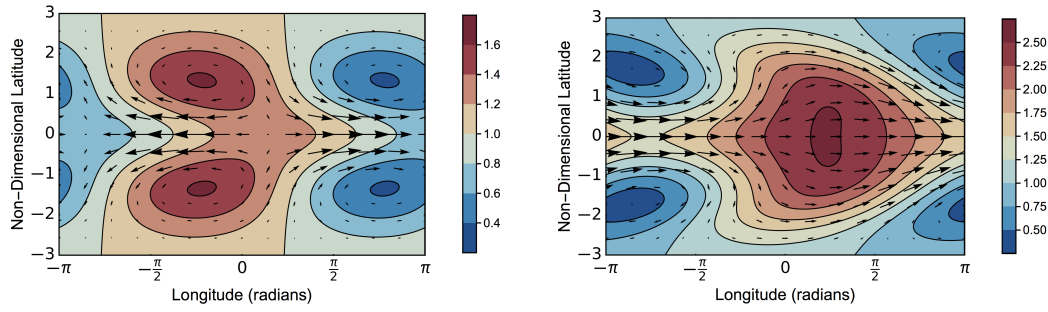
The stationary response to steady forcing of Equation 4.6 is found by setting  $Q(y) = Q_0 e^{-y^2/2}$  (Matsuno, 1966) and  $\partial/\partial t = 0$ , giving the linear system of equations:

$$\begin{pmatrix} \alpha_{dyn} + ik_x \bar{U}(y) & \frac{\partial \bar{U}(y)}{\partial y} - y & ik_x \\ y & \alpha_{dyn} + ik_x \bar{U}(y) & \frac{\partial}{\partial y} \\ ik_x \bar{H}' & -y \bar{U}(y) + \bar{H}' \frac{\partial}{\partial y} & \alpha_{rad} + k_x \bar{U}(y) \end{pmatrix} \begin{pmatrix} u \\ v \\ h \end{pmatrix} = \begin{pmatrix} 0 \\ 0 \\ Q(y) \end{pmatrix}, \quad (4.9)$$

$$\bar{H}' = 1 + \bar{H}(y).$$

The eastward zonal flow is  $\bar{U}(y) = U_0 e^{-y^2/2}$ , where  $U_0$  is a free parameter. The equatorial Rossby radius of the planet sets the meridional scale of the beta-plane system, and by extension the scale of the forcing and width of the jet. This means that this beta-plane solution is limited to planets where the equatorial Rossby radius is comparable to the planetary radius and the width of the jet. These conditions are met on many realistic tidally locked planets, making the beta-plane solution a useful approximation (Pierrehumbert and Hammond, 2019). I will extend the solution to a spherical geometry without these limitations later in this chapter.

For the stationary solutions in this section, the non-dimensional damping rate is  $\alpha = 0.2$  (Matsuno, 1966) and the non-dimensional forcing magnitude is  $Q_0 = 1.0$ . The magnitude of the zonal flow  $U_0$  is varied between 0 and 1, as it was shown earlier that  $U_0 \sim 1$  is required for a significant hot-spot shift. As in Section 4.3, the geostrophically balanced background state is  $\bar{U}(y) = U_0 e^{-y^2/2}$  and  $\bar{H}(y) = U_0 e^{-y^2/2}$ . Solving Equation 4.9 with the method described in Appendix B gives the  $u$ ,  $v$ , and  $h$  fields that satisfy these equations.

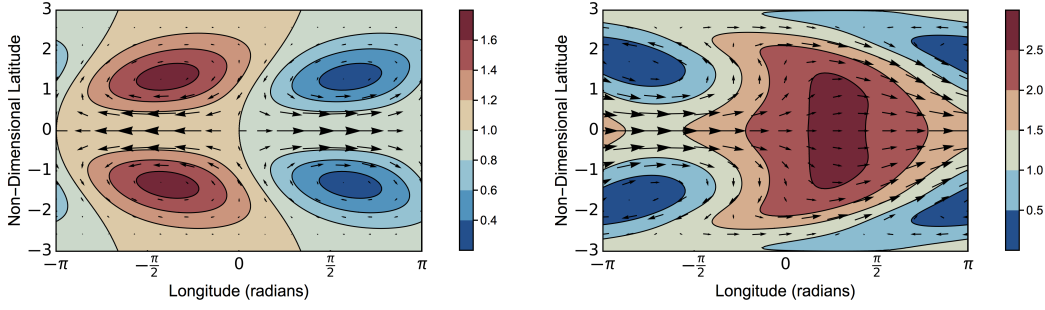


(a) The response to forcing in zero background flow ([Matsuno, 1966](#)). (b) The response to forcing in background flow  $\bar{U}(y) = U_0 e^{-y^2/2}$ ,  $U_0 = 1.0$ .

Figure 4.6: The effect of a background shear flow  $\bar{U}(y)$  on the forced solutions of Equation 4.9. The eastward flow Doppler-shifts the maximum of the response eastwards, producing the hot-spot shift seen in GCM simulations ([Tsai et al., 2014](#)).

Figure 4.6 shows the effect of the shear flow  $\bar{U}(y)$  on the response to day-night forcing. This is the main result of this chapter, as it shows how the flow produces the global circulation pattern on a tidally locked planet in Figure 4.5. The first plot, Figure 4.6a, shows the response to forcing in zero background flow. This is exactly the same as the linear solutions in [Matsuno \(1966\)](#) and [Showman and Polvani \(2011\)](#), which were used in Chapter 3 to calculate the initial acceleration of these atmospheres. This linear solution does not match the height field and velocities in Figure 4.5. In particular, the “hot-spot” and cold (low height) Rossby waves are in different places in the shallow-water solution and in the GCM simulation.

The second plot, Figure 4.6b, shows the response to forcing in the shear flow  $\bar{U}(y)$  and height field  $\bar{H}(y)$ , which models the equilibrium state of the atmosphere. This qualitatively matches the GCM simulations in Figure 4.5, with the “hot-spot” shifted east and the cold Rossby waves in the same places. I suggest that the solution in zero background flow in [Showman and Polvani \(2011\)](#) predicts the initial acceleration of the atmosphere, which forms a zonal jet that modifies the response to day-night forcing, producing the global circulation pattern and the hot-spot shift as in [Tsai et al. \(2014\)](#).



(a) Forced response in zero flow, with zero dynamical damping.  
 (b) Forced response in shear flow  $\bar{U}(y) = U_o e^{-y^2/2}$ ,  $U_o = 1.0$ .

Figure 4.7: The forced response in zero background flow and a shear background flow, for dynamical damping  $\alpha_{dyn} = 0$ . These plots have the same form as those in Figure 4.6, showing that the dynamical damping is not critical.

### 4.3.2 Effect of Damping

The linear shallow-water model has several free parameters. I discussed the choice of the forcing strength  $Q_o$  and jet speed  $U_o$  earlier. The strengths of the free parameters  $\alpha_{rad}$  and  $\alpha_{dyn}$ , the radiative and dynamical damping rates, affect the magnitude and form of the response to forcing. I previously showed that a very strong  $\alpha_{rad}$  gives a response to forcing centred at the substellar point, but that for realistic radiative damping rates (Showman and Polvani, 2011) the solution is similar to that in Figure 4.6. The solution in Figure 4.6 assumed that  $\alpha_{rad}$  and  $\alpha_{dyn}$  were equal, which allows an analytic solution but is not physically justified.

The linear radiative damping  $\alpha_{rad}$  has a realistic physical basis, but the linear dynamical damping  $\alpha_{dyn}$  does not. It could be considered an approximation to effects like eddy viscosity, magnetohydrodynamic damping, or the effect of nonlinear terms (Heng and Workman, 2014). This section tests the effect of varying this damping rate, motivated by the uncertainty in the realism of a linear dynamical damping.

Figure 4.7 shows the response to forcing when the dynamical damping rate  $\alpha_{dyn}$  is set to zero, with the same parameters as the solutions in Figure 4.6 otherwise. The first panel shows the solution in zero background flow, where the Kelvin response

(the peak on the equator, in the previous plot) is now much weaker than the Rossby response (off the equator). The second panel shows the response to forcing in the shear background flow  $\bar{U}(y) = U_0 e^{-y^2/2}$  and associated height field  $\bar{H}(y)$ . This response is similar to the previous case with strong dynamical damping, showing that this damping is not a crucial part of the mechanism.

The qualitative form of the forced solution does not depend strongly on the choice of the parameters  $\alpha_{rad}$  and  $\alpha_{dyn}$ . The dynamical damping  $\alpha_{dyn}$  does not have a clear physical basis, but is not strictly necessary to include to match the GCM simulations – however, it is useful to include for a simpler solution that is closer to the analytic result in [Matsuno \(1966\)](#).

#### 4.3.3 Hot-Spot Shift Mechanism

I have shown that the shallow-water response to forcing in a shear flow  $\bar{U}(y)$  qualitatively matches a GCM simulation of a tidally locked planet. This section shows how the flow modifies the global circulation.

Figure 4.8 explains how the solution in a shear flow is built up from two main effects. The first panel shows the response to forcing in zero flow, with the same solution as [Matsuno \(1966\)](#). The second panel shows the response to forcing in a uniform flow  $U_0$  (the same as the last panel of Figure 4.1). This flow shifts the Rossby and Kelvin modes eastwards, as explained in Section 4.3 ([Tsai et al., 2014](#)). The third panel shows the zonally uniform height perturbation  $\bar{H}(y)$  that geostrophically balances the zonal flow.

The fourth panel shows the sum of the second and third panels. East of the substellar point, the on-equator maximum and off-equator maxima combine to form a large, meridionally continuous “hot-spot”. West of the substellar point, the equatorial maximum and off-equator minima combine to increase the meridional height gradient. This preserves the off-equator cold Rossby lobes, unlike on the

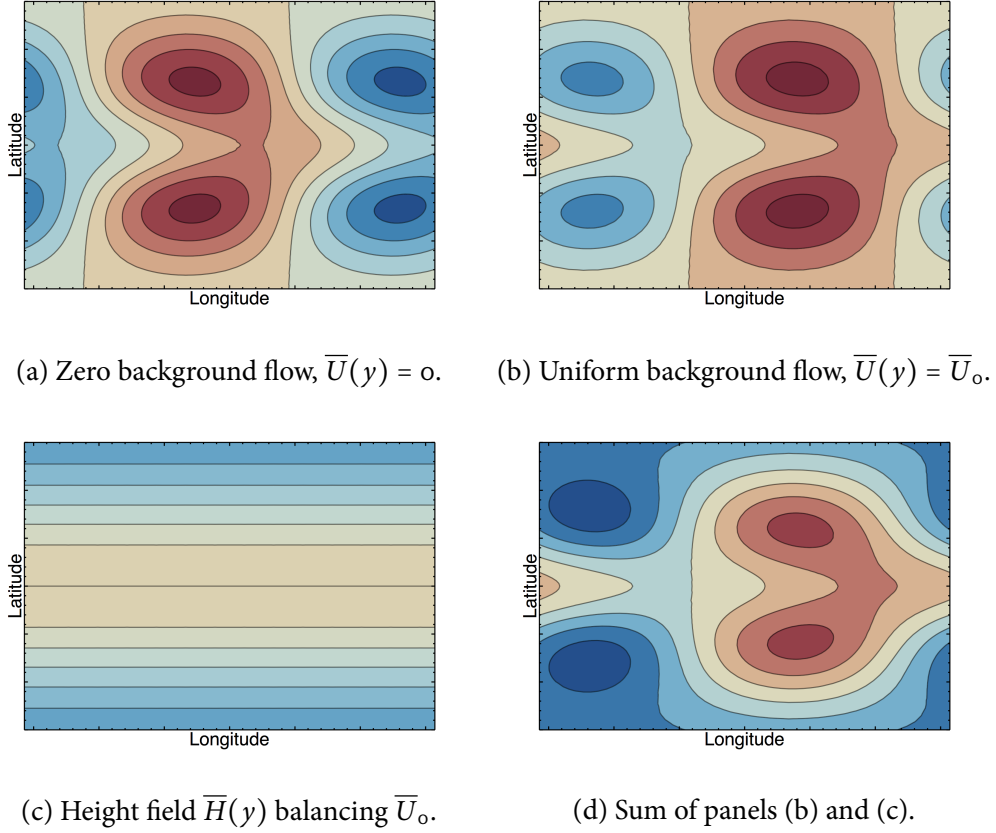


Figure 4.8: Height fields of various responses to forcing, showing how the sum of the Doppler-shifted height field and the height field due to the zonal jet produces the distinctive pattern in Figures 4.5 and 4.6.

day-side where the hot Rossby lobes are subsumed into the hot-spot. Both of these features are in the same place as in the GCM simulations in Figure 4.5.

This combination of effects also explains the velocities in Figure 4.5. On the equator west of the substellar point, the eastward Rossby wave velocities combine with the eastward zonal jet to give strong eastward flow. East of the substellar point, the westward Rossby wave velocities on the equator oppose the jet, leading to the region of weak zonal flow east of the substellar point in Figure 4.5. This simple model of the global circulation as the sum of the wave-0 jet and the wave-1 forced response will be used later to show how the observable temperature distribution scales with planetary parameters.

#### 4.4 Forced Response in Shear Flow on a Sphere

The forced linear system on a beta-plane is useful for an intuitive understanding of the wave-mean flow interactions, as it is closely linked to the simple analytic equatorial wave solutions of [Matsuno \(1966\)](#). The beta-plane is less useful for direct comparison with real planets or GCM simulations, as the assumption of a linear Coriolis parameter is inaccurate at high latitudes. It also does not directly represent the latitudinal direction or the effect of rotation rate, as the  $y$ -coordinate is non-dimensionalised to the equatorial Rossby radius. The system is therefore only appropriate for tidally locked planets where this radius is similar to the planetary radius.

This section shows the response to forcing for a shallow-water system in a spherical geometry. This represents the same physical system as the earlier beta-plane model, but is more directly comparable to GCM simulations, as it does not require that the equatorial Rossby radius is comparable to the planetary radius.

The shallow-water equations on a sphere, linearised about a zonally uniform background flow  $\bar{U}(\phi)$  and height  $\bar{H}(\phi)$  are ([Dunkerton, 1990](#); [Iga and Matsuda, 2005](#)):

$$\begin{aligned} \frac{\partial u'}{\partial t} + \frac{\partial (\bar{U}u')}{a \cos \theta \partial \lambda} + v' \frac{\partial \bar{U}}{a \partial \theta} - \frac{\bar{U}v' \tan \theta}{a} &= 2\Omega v' \sin \theta - \frac{g \partial h'}{a \cos \theta \partial \lambda}, \\ \frac{\partial v'}{\partial t} + \frac{\partial (\bar{U}v')}{a \cos \theta \partial \lambda} + \frac{2\bar{U}u' \tan \theta}{a} &= -2\Omega u' \sin \theta - \frac{g \partial h'}{a \partial \theta}, \\ \frac{\partial h'}{\partial t} + v' \frac{\partial \bar{H}}{a \partial \theta} + \bar{U} \frac{\partial h'}{a \cos \theta \partial \lambda} + \bar{H} \nabla_H \cdot \mathbf{v}' &= 0, \end{aligned} \quad (4.10)$$

where  $h$  is the height of the layer,  $\mathbf{v} = (u, v)$  is the velocity,  $\theta$  is latitude,  $\lambda$  is longitude,  $t$  is time,  $a$  is radius,  $g$  is gravity, and  $\Omega$  is angular velocity. The forcing due to the day-night instellation is  $F = F_0 \cos \theta \sin \lambda$ . Overbars denote zonal-mean quantities, which are the background zonal flow and the associated height field, and dashes denote perturbations to this background state.

The background state is stationary and in gradient wind balance, satisfying the meridional momentum equation in Equation 4.10, which gives a different condition to the background height on the beta-plane:

$$\frac{1}{a} \frac{\partial}{\partial \theta} (\bar{H} + h_g) = - \left( 2\Omega \bar{U} \sin \theta + \frac{\bar{U}^2}{a} \tan \theta \right). \quad (4.11)$$

The perturbed variables are wavelike in longitude and are uniformly damped, so are proportional to  $e^{i(m\lambda - \sigma t)}$ , where  $\sigma = i\alpha$ . All variables are non-dimensionalised with velocity scale  $2\Omega a$ , height scale  $(2\Omega a)^2/g$  and time scale  $1/(2\Omega)$ , and denoted as such by an asterisk. This gives the following non-dimensional shallow-water equations:

$$\begin{aligned} \alpha^* u_m^* + im \frac{\bar{U}^* u_m^*}{\cos \theta} + v_m^* \frac{\partial \bar{U}^*}{\partial \theta} - \bar{U}^* v_m^* \tan \theta &= v_m^* \sin \theta - \frac{im h_m^*}{\cos \theta}, \\ \alpha^* v_m^* + im \frac{\bar{U}^* v_m^*}{\cos \theta} + 2\bar{U}^* u_m^* \tan \theta &= -u_m^* \sin \theta - \frac{\partial h_m^*}{\partial \theta}, \\ \alpha^* h_m^* + im \bar{U}^* \frac{h_m^*}{\cos \theta} &= -\frac{\epsilon^*}{\cos \theta} \left[ imu_m^* + \frac{\partial}{\partial \theta} (\cos \theta v_m^*) \right], \end{aligned} \quad (4.12)$$

where  $\epsilon \equiv (2\Omega a)^2/gH$  is Lamb's parameter, which in this system determines the strength of the effect of the rotation of the planet (Longuet-Higgins, 1968). This parameter was not present in the beta-plane system, where the effect of the rotation rate on the system was non-dimensionalised out by setting the meridional coordinate to the equatorial Rossby radius. I will show the effect of varying the rotation rate later in this section.

Appendix B shows how these coupled equations can be combined into a version of Laplace's tidal equation for the variable  $\mu = \sin \theta$  (Dunkerton, 1990), modified to include the effect of the background shear flow:

$$\frac{\partial^2 \phi_m^*}{\partial \mu^2} - B(\sigma^*, \mu) \frac{\partial \phi_m^*}{\partial \mu} - A(\sigma^*, \mu) \phi_m^* = \frac{F(\theta, x)}{i\sigma}, \quad (4.13)$$

where

$$\begin{aligned}
 A(\sigma^*, \mu) &\equiv \frac{1}{1 - \mu^2} \left[ m(m+1) - m\mu \frac{1}{\Delta^*} \frac{\partial \Delta^*}{\partial \mu} + \epsilon \Delta^* \right. \\
 &\quad \left. + \frac{m}{\Delta^* \hat{\sigma}^*} \left( f_1^* \frac{\partial \Delta^*}{\partial \mu} - \Delta^* \frac{\partial f_1^*}{\partial \mu} \right) \right], \\
 B(\sigma^*, \mu) &\equiv \frac{1}{\Delta^*} \frac{\partial \Delta^*}{\partial \mu} + \frac{2\mu(m+1)}{(1 - \mu^2)}, \\
 \Delta^* &\equiv f_1^* \bar{\zeta}^* - \hat{\sigma}^{*2}.
 \end{aligned} \tag{4.14}$$

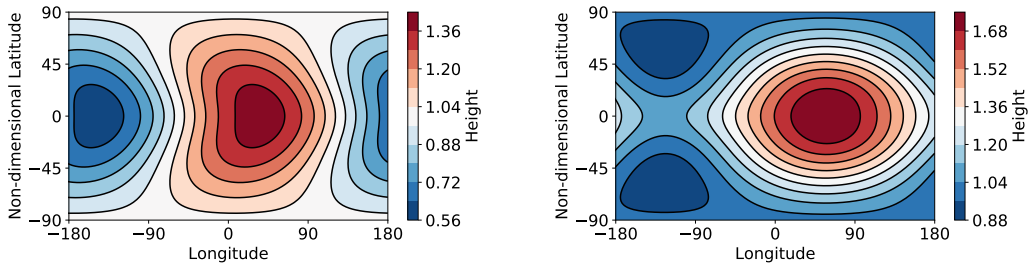
Appendix B shows how Equation 4.13 is solved with the Chebyshev pseudo-spectral collocation method used in Wang et al. (2016) to find the eigenfunctions of Laplace's tidal equation on a sphere (Longuet-Higgins, 1968; Dunkerton, 1990).

The free parameters of the system are the forcing strength  $F_o$ , damping rate  $\alpha$ , rotation rate  $\Omega$ , radius  $a$ , gravity  $g$ , and background height  $H_o$ . The background flow is set by the jet speed  $U_o$  and jet width  $L_{jet}$ , for a flow profile  $\bar{U} = U_o \exp(-\mu^2/L_{jet}) \cos \theta$  where  $\mu = \sin \theta$ . The default parameters of  $F_o = 0.3$ ,  $\alpha = 0.6$ ,  $\Omega = 1.0$ ,  $a = 1.0$ ,  $g = 2.0$ ,  $H_o = 1.0$ ,  $U_o = 0.75$ , and  $L_{jet} = \sqrt{3}$  were based on the GCM simulation in Figure 4.5.

Figure 4.9 shows the effect of the background zonal flow  $\bar{U}$  on the response to day-night forcing in a spherical geometry. The background flow Doppler-shifts the maximum of the wave response eastwards, as was the case in Figure 4.6 on the beta-plane, and adds a zonally uniform height perturbation centred on the equator. The resulting response to forcing is qualitatively similar to the simulation in Figure 4.5.

## 4.5 Scaling Relations

The previous section showed how the global circulation on a tidally locked planet is a combination of a wave-0 jet and a wave-1 response to day-night forcing. This section considers how each of these components depend on planetary parameters, to predict how the global circulation and temperature distribution scales with these parameters.



(a) The forced solution with zero background flow, similar to the beta-plane solution in [Matsuno \(1966\)](#).

(b) The forced solution with background flow  $U_0 \exp(-\mu^2/L_{jet}) \cos \theta$ ,  $U_0 = 0.75$ , matching the simulations in Figure 4.5.

Figure 4.9: The effect of a background shear flow  $\bar{U}(\phi)$  on the forced solutions of Equation 4.10, matching the form of the beta-plane solutions in Figure 4.6.

[Komacek and Showman \(2016\)](#) and [Zhang and Showman \(2017\)](#) produced 1D scaling relations based on a balance of advective and radiative timescales on the equator to predict how observables such as hot-spot shift and day-night contrast scale with planetary parameters. This section derives similar 1D scaling relations using the shallow-water model, discusses the 2D scaling of the global circulation, and compares these predictions to GCM simulations.

#### 4.5.1 1D Scaling Relations

Reducing the 2D shallow-water system to a 1D system on the equator gives an analytically solvable system, which provides simple predictions of the observable hot-spot shift and day-night contrast. Setting  $\phi = 0$  and retaining only the damping and advection terms, the third line of Equation 4.6,

$$\frac{\partial \bar{H}' u}{\partial x} + \bar{H}' \frac{\partial v}{\partial y} - y \bar{U}(y) v + \frac{\partial h}{\partial t} + \alpha_{rad} h + \frac{\partial \bar{U}(y) h}{\partial x} = Q(y), \quad (4.15)$$

becomes

$$\frac{\partial h}{\partial t} + \alpha h + \frac{\partial U_0 h}{\partial x} = Q_0. \quad (4.16)$$

The stationary wave-1 response is found by setting  $\partial/\partial t = 0$  and  $\partial/\partial x = ik_x$ :

$$-\alpha h(y=0) + ik_x U_0 h(y=0) = Q_0. \quad (4.17)$$

So, the on-equator height perturbation  $h(x, y=0) = h(y=0)e^{ik_xx}$  is:

$$h(x, y=0) = \frac{Q_0}{\alpha^2 + k_x^2 U_0^2} (-\alpha \cos(k_x x) + k_x U_0 \sin k_x x). \quad (4.18)$$

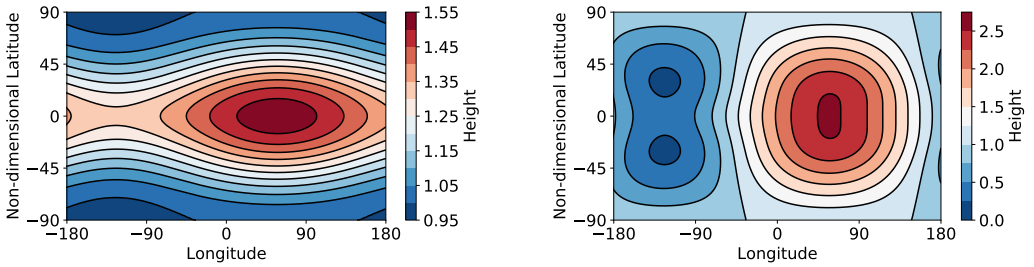
This is a sinusoidal height perturbation on the equator, with magnitude

$$h_0 = \frac{\alpha + k_x U_0}{\alpha^2 + k_x^2 U_0^2} Q_0. \quad (4.19)$$

The hot-spot shift  $x_0$  is at the maximum of this sinusoidal curve, where  $\partial h/\partial x = 0$ :

$$x_0 = \frac{1}{k_x} \tan^{-1}(k_x \frac{U_0}{\alpha}). \quad (4.20)$$

This is the same as the simplest approximation of the hot-spot shift calculated by [Zhang and Showman \(2017\)](#),  $\lambda_s = \tan^{-1}(\frac{\tau_{rad}}{\tau_{adv}})$ , (where  $\tau_{rad}$  corresponds to  $1/\alpha$  and  $\tau_{adv}$  corresponds to  $k_x/U_0$ ). Equation 4.20 predicts that the hot-spot shift varies between  $0^\circ$  and  $90^\circ$  east of the substellar point. There are two similar ways to interpret this physically. First, the size of the shift can be seen as a balance between the jet transporting heat eastwards according to the advective timescale  $\tau_{adv}$ , and the heat radiating away according to the radiative timescale  $\tau_{rad}$  ([Komacek and Showman, 2016](#); [Zhang and Showman, 2017](#); [Hammond and Pierrehumbert, 2017](#)). Or, as discussed above, they can instead be seen as a balance of the flow  $U_0$  shifting the stationary waves  $90^\circ$  out of phase with the forcing, versus the damping  $\alpha_{rad}$  bringing them in phase with the forcing ([Tsai et al., 2014](#); [Hammond and Pierrehumbert, 2018](#)). Section 4.6 discusses these two mechanisms in more detail.



(a)  $F_o = 0.1$ , giving a weak wave-1 component and a more zonally uniform field.

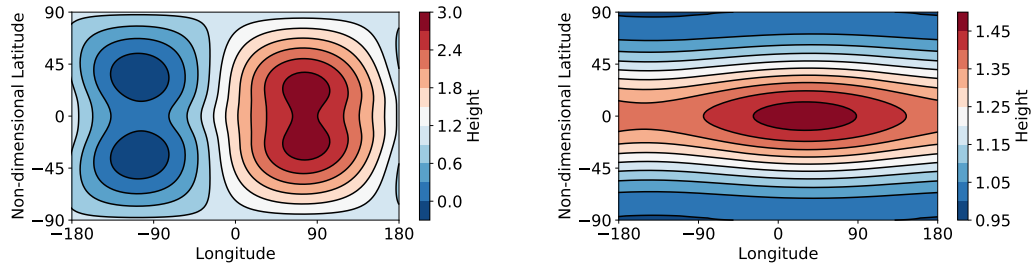
(b)  $F_o = 1.0$ , giving a strong wave-1 component and a less zonally uniform field.

Figure 4.10: Spherical solutions with low and high forcing  $F_o$ , showing how this affects the strength of the wave-1 component relative to the unchanged wave-0 jet component, affecting the longitudinal variation and day-night contrast.

### 4.5.2 2D Scaling Relations

This section shows how the forcing strength, damping rate, and rotation rate affect the global circulation in the linear shallow-water model on a sphere. The spherical shallow-water model is better suited to this than the beta-plane model, as it includes the effect of rotation rate. In the next section, I will show how this qualitatively explains the global circulation of a suite of GCM tests.

Figure 4.10 shows the effect of varying the forcing magnitude  $F_o$  in a system with all other parameters the same as those in Figure 4.9b. The case with low  $F_o$  has a weak wave-1 height field due to the day-night forcing compared to its wave-0 height field due to the jet, so the global height field is very zonally uniform. In contrast, the case with high  $F_o$  has a much stronger wave-1 height field so varies greatly with longitude. The hot-spot shifts are the same in both cases, as the Doppler-shift is not affected. If the atmosphere is in hydrostatic equilibrium, the height field corresponds to the temperature field, so is directly observable through the thermally emitted phase curve. The phase curve of the case with high  $F_o$  would have a much larger magnitude than weakly forced case, but their phase shifts would be the same. Chapter 5 investigates the behaviour of thermal phase curves in more detail for the planet 55 Cancri e.



(a)  $\alpha = 0.2$ , giving a strong wave-1 component and a large hot-spot shift.  
 (b)  $\alpha = 2.0$ , giving a weak wave-1 component and a smaller hot-spot shift.

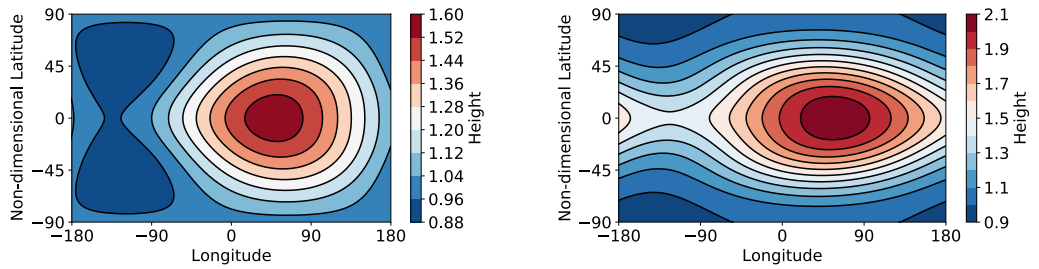
Figure 4.11: Spherical solutions with low and high damping  $\alpha$ , showing how this affects the strength of the wave-1 component and the magnitude of the Doppler-shift of the wave components.

Figure 4.11 shows the effect of varying the damping rate  $\alpha$  in the same system. The case with low damping is similar to the case with high forcing, as it also increases the strength of the wave-1 field relative to the zonally uniform field. The case with high damping has a weak wave-1 response, and a smaller hot-spot shift as the high damping rate brings the maximum more closely into phase with the forcing. The weakly damped case would have a phase curve with a large amplitude and large phase shift, while the strongly damped case would have a small amplitude and a small phase shift.

Figure 4.12 shows the effect of the rotation rate  $\Omega$ .  $\Omega$  scales the magnitude of the zonally uniform height perturbation due to the jet, due to the  $f$  dependence in Equation 4.11. This means that  $\Omega$  has the same leading-order effect as  $F_o$ , scaling the magnitude of the zonally uniform height perturbation relative to the wave-1 forced response. The case with low  $\Omega$  would have a phase curve with a large amplitude and large phase shift, while the case with high  $\Omega$  would have a smaller amplitude.

### 4.5.3 GCM Scaling Relations

These shallow-water solutions predict how the GCM should respond to changes in its input parameters. Figure 4.13 shows a suite of tests in Exo-FMS that vary



(a)  $\Omega = 0.3$ , giving a weak wave-o component and a large day-night contrast.

(b)  $\Omega = 3.0$ , giving a strong wave-o component and a small day-night contrast.

Figure 4.12: Spherical solutions with low and high rotation rate  $\Omega$ , showing how this affects the magnitude of the wave-o height perturbation  $\bar{H}(\phi)$  balancing the imposed shear flow  $\bar{U}(\phi)$ .

the instellation and rotation rate of the test plotted in Figure 4.5. The instellation corresponds to the forcing strength in the shallow-water model, and also indirectly affects the radiative damping rate via the atmospheric equilibrium temperature.

Changing the forcing, damping, and rotation rate has the same qualitative effects in these GCM tests as in the shallow-water model. Increasing the forcing makes the atmospheres hotter, giving larger day-night temperature differences (matching the shallow-water solutions with high forcing). The colder tests are more zonally uniform, as their jets dominate the global height field. The more rapidly rotating tests are also more zonally uniform, as this increases the zonally uniform height perturbation of the jet, due to its dependence on  $\Omega$  in Equation 4.11. This is especially clear in the “cold” tests, where the more rapidly rotating tests are very zonally uniform.

In the shallow-water model, an increased damping rate gave a smaller hot-spot shift, as it brought the wave response into phase with the forcing. In the GCM, the colder tests have a low damping rate so all have hot-spots shifted further east. The hotter tests have higher damping rates so have smaller hot-spot shifts – this is especially clear in the 2 day cases. Chapter 5 also shows the effect of damping, where varying the mean molecular weight of the atmosphere affects the damping rate and changes the hot-spot shift.

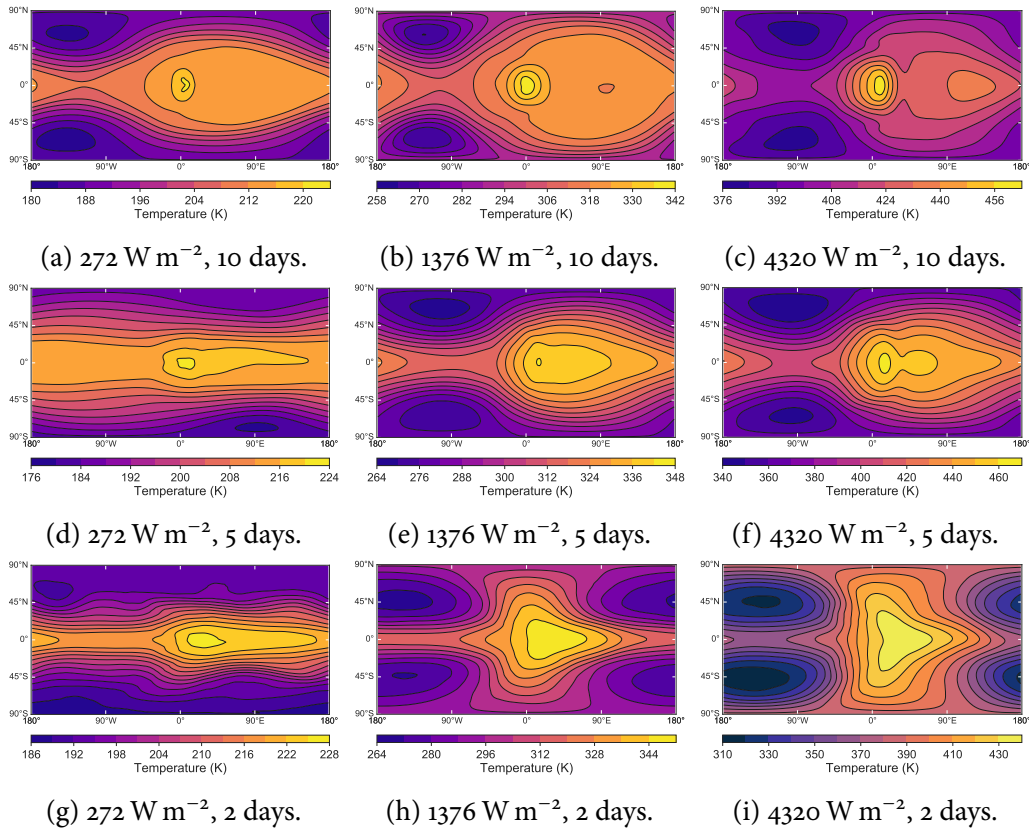


Figure 4.13: The temperature at the 500 mbar level from a suite of simulations of tidally locked planets with 1 bar atmospheres in the GCM Exo-FMS, with different stellar constants and rotation periods. All other parameters are the same as those in Figure 4.5. Reproduced with data from [Pierrehumbert and Hammond \(2019\)](#).

## 4.6 Discussion

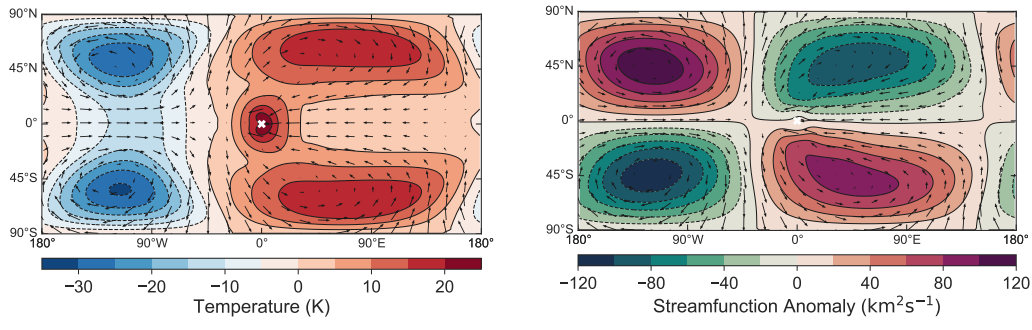
Section 4.5.1 showed how the hot-spot shift can be interpreted either as caused by advection of heat by the equatorial jet, or caused by a Doppler-shift of the stationary waves excited by the day-night forcing. These mechanisms are similar on some level, giving the same scaling behaviour on the equator as shown previously. However, they are physically different ideas and should have different effects. If advection by the jet produces the shift then the temperature and tracer fields in GCM simulations should be closely coupled. But, if the temperature field is instead set by the stationary wave pattern, it could be different to the distribution of tracers advected by the flow.

Comparing temperature distributions to cloud distributions via thermal and optical phase curves could help distinguish these mechanisms.

This chapter suggests that the Doppler-shift of the waves is the appropriate mechanism, as it explains the global temperature and velocity distribution of the GCM simulations. Figure 4.14 shows eddy fields (i.e. with the zonal mean subtracted at every latitude) from the GCM simulation of a tidally locked planet shown in Figure 4.5. This preserves the dominant wave-1 component forced by the day-night heating. Comparing Figure 4.14 with Figure 4.8 or Figure 4.9 shows how the wave solutions match the GCM results. The cold, anticlockwise Rossby waves are shifted to  $-90^\circ$  in the GCM, matching the shifted pattern in Figure 4.8b rather than the non-shifted pattern in Figure 4.8a. The wave-based mechanism also explains the weak zonal flow east of the substellar point in the GCM simulation in Figure 4.5 – the mean eastward zonal jet cancels with the local westward flow due to the waves shown in Figure 4.14

This Doppler-shift mechanism was first put forward for tidally locked planets by [Tsai et al. \(2014\)](#), for a zonally uniform flow. This chapter generalised the mechanism to the case of a zonally varying flow and an associated height perturbation, which was needed to fully match the global circulation in the GCM simulations. Advection of heat by the jet will still have some effect on the circulation, but the wave-based picture matches the circulation well enough that any advection effects appear to be minor. I have compared the shallow model to GCM simulations of a particular idealised planetary atmosphere, but very similar flow and wave patterns are seen in other studies of a variety of planets ([Charnay et al., 2015](#); [Heng and Showman, 2015](#); [Kataria et al., 2014](#); [Mayne et al., 2017](#); [Boutle et al., 2017](#)).

A compelling result of studying GFD on exoplanets is the possibility of plotting trends in atmospheric behaviour for classes of similar planets, as this is not possible with the individual data points of disparate Solar System planets. [Komacek et al. \(2017\)](#) showed that the fractional day-night contrast  $A = (T_{day} - T_{night})/T_{day}$  of



(a) Eddy temperature and velocities. (b) Eddy streamfunction and velocities.

Figure 4.14: The time-mean eddy temperature, velocity, and streamfunction fields (where the zonal mean at that latitude is subtracted from each point) on the half-surface pressure level of the GCM simulation shown in Figure 4.5. These plots match the “eddy” shallow-water response in Figure 4.8, before the zonally uniform jet is added.

many observed hot Jupiters increases with planetary equilibrium temperature. This is consistent with the discussion in Section 4.5.2, which shows in Figure 4.10 how increased forcing gives a stronger wave-1 response than the wave-0 jet height field, giving a larger day-night contrast.

[Komacek et al. \(2017\)](#) also showed that the hot-spot shift on hot Jupiters decreases with increasing equilibrium temperature. This is consistent with Section 4.5.2, which predicted a decreased hot-spot shift at higher temperatures due to increased radiative damping. It is also consistent with the GCM simulations in Figure 4.13, where the tests with higher temperature had smaller hot-spot shifts. [Komacek et al. \(2017\)](#) explained this trend as an increased damping rate giving a smaller shift as it dominates the heat transport via advection. This chapter instead explains the trend as due to the increased damping moving the stationary wave response into phase with the forcing, due to Equation 4.5. As the number and quality of these observations increase, it will become possible to test the predictions of different descriptions of global circulation, such as the advection-based versus wave-based mechanisms discussed here.

## 4.7 Conclusions

This chapter showed how the zonal flow discussed in Chapter 3 produces the hot-spot shift and global circulation pattern of the atmospheres of tidally locked planets. I used a shallow-water model linearised about an equatorial jet  $\bar{U}(y)$  to show how the flow Doppler-shifts the stationary waves excited by the day-night forcing. These waves combine with the zonally uniform jet to give the distinctive circulation pattern produced by GCM simulations.

Varying the parameters of the shallow-water model showed how the global circulation and temperature distribution scales with planetary parameters. This predicted scaling relations for observables such as day-night temperature contrast increasing with temperature, and hot-spot shift decreasing with temperature. These predictions are similar to the advection-based scaling of [Komacek et al. \(2017\)](#) and [Zhang and Showman \(2017\)](#), but have a different physical mechanism. I suggest that the wave-based mechanism is a better description of the global circulation and hot spot shift than the advection-based mechanism. Further observations could test the predictions of these mechanisms to find which is a better model.

The next step will be to the linear model to predict the equilibrium flow speeds and global temperature fields of tidally locked planets. The model could also be used to find the free modes in their atmospheres, then to compare these to the travelling waves and instabilities seen in simulations and observations ([Pierrehumbert and Hammond, 2019](#); [Armstrong et al., 2017](#)).

This chapter showed how the interaction between the equatorial jet and the stationary waves excited by the instellation produces the global circulation and temperature distribution in the atmosphere of a tidally locked planet. The rest of this thesis will apply this theory to a case study of the planet 55 Cancri e, comparing simple models and numerical simulations to observations of its temperature distribution.



## CHAPTER 5

# *Linking the Climate and Thermal Phase Curve of 55 Cancri e*

---

*Most of the results in this chapter are published in [Hammond and Pierrehumbert \(2017\)](#).*

The first thermal phase curve of a terrestrial exoplanet was measured by [Demory et al. \(2016\)](#) using the *Spitzer* space telescope to observe the thermal emission of the “lava planet” 55 Cancri e. This followed the measurement of transits in the visible ([Winn et al., 2011](#)) and infrared ([Demory et al., 2011](#)). It was the first observation directly linked to the global circulation of a terrestrial planet outside our solar system, and provides an opportunity to test the theory of atmospheric circulation of terrestrial tidally locked planets that was developed in the previous chapters.

This chapter aims to recreate the observed thermal phase curve of 55 Cancri e with simulations of an idealised atmosphere. I will use the GCM Exo-FMS to model a range of potential atmospheres, with parameters based on analytic predictions of how the phase curve depends on bulk atmospheric properties. The simulations will show that the observed phase curve could be explained by an atmosphere with specific properties. This chapter builds on studies such as [Cowan and Agol \(2011\)](#), [Menou \(2012\)](#), [Komacek and Showman \(2016\)](#), and [Zhang and Showman \(2017\)](#), which all explored the effect of atmospheric properties on the observable global circulation of

tidally locked planets.

Section 5.1 gives an overview of observations of 55 Cancri e to date, including the thermal phase curve (Demory et al., 2016). Section 5.2 discusses the general circulation of tidally locked planets, and introduces scaling relations from Zhang and Showman (2017) that will be used to interpret the phase curve and GCM simulations. Section 5.3 discusses the configuration of the simulations of 55 Cancri e in Exo-FMS. Section 5.4 shows the results of these simulations, focusing on their global temperature distribution and vertical structure. These simulations are post-processed to produce observations in Section 5.5. Section 5.6 discusses the constraints that this modelling can place on the likely atmospheric composition of this planet.

The model atmosphere that fitted the observations best, “Test 4”, had a surface pressure of 5 bar and a mean molecular weight of  $4.6 \text{ g mol}^{-1}$ . The phase curve of this test matched the day-side magnitude and phase of the observations, but the simulated night-side thermal emission was too high. Diagnostic estimates of cloud formation suggested that the night-side could be cold enough for SiO clouds to form high on the night-side, reducing the brightness temperature and matching the observations better. The simulations ruled out some atmospheric compositions. An  $\text{H}_2$  atmosphere could not fit the observations as it gave too small a day-night contrast in the simulations and scaling relations. An atmosphere with a very low surface pressure on the order of 1 bar would also not be possible, as it could not reproduce the observed hot-spot shift.

This chapter concludes that an atmosphere could explain the observed phase curve of 55 Cancri e, given a sufficiently high mean molecular weight and high surface pressure. The simulations require a process such as night-side cloud formation to lower the brightness temperature of their night-side, if they are to match the observations. These conclusions highlight the need for further measurements of the atmosphere of 55 Cancri e and other tidally locked planets.

## 5.1 Observations of 55 Cancri e

This section discusses observations of the planet 55 Cancri e, and considers its possible atmospheric states and composition. I will show the thermal phase curve observed by Demory et al. (2016), and introduce theoretical scaling relations used to interpret the phase curves of tidally locked exoplanets.

### 5.1.1 55 Cancri e

55 Cancri e is a “lava planet”, a rocky super-Earth with radius  $1.875 R_E$  orbiting close to its host star 55 Cancri A (Crida et al., 2018). It is expected to be tidally locked due to its proximity to its star (Pierrehumbert and Hammond, 2019), which is supported by the large day-night contrast shown by its thermal phase curve (Demory et al., 2016). Transits of 55 Cancri e in the visible (Winn et al., 2011) and infrared (Demory et al., 2011) presented the possibility of characterisation. 55 Cancri e is particularly amenable to observations for a terrestrial planet, owing to its high equilibrium temperature of approximately 2500 K and its large radius (Tinetti et al., 2016).

### 5.1.2 Thermal phase curve

A phase curve is a measurement of the flux from a planet and its star over one orbital period (or averaged over many orbital periods). A “thermal phase curve” is the flux at a thermal wavelength, corresponding to the emission of the atmosphere, which is determined by its temperature structure.

Figure 5.1 shows an idealised thermal phase curve of a tidally locked planet, and highlights the key features. At  $90^\circ$ , the planet passes in front of the star, for its transit or “primary eclipse”, causing a large dip in flux from the system. At  $270^\circ$ , the planet passes behind the star for its “secondary eclipse”, causing a small dip in flux. The flux above  $F/F_S = 1$  is due to the planet, and is approximately sinusoidal because of

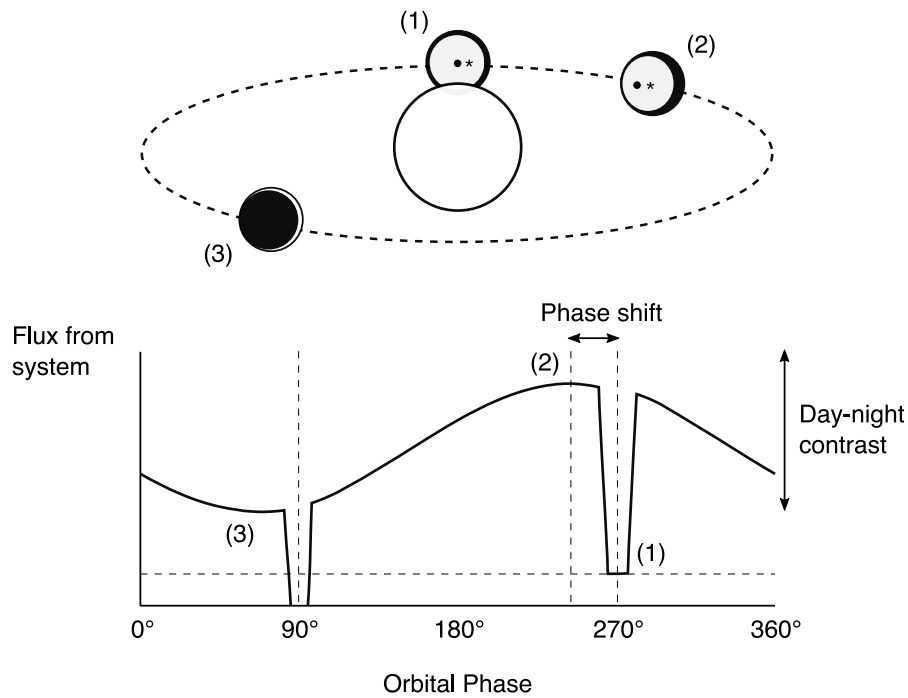


Figure 5.1: A schematic of the phase curve observed of the flux from a planet as it orbits its star. Position 1 is the secondary eclipse, 2 is the phase of the maximum thermal emission, and 3 is the phase of minimum thermal emission.

the day-side heating and night-side cooling of the planet. The difference in thermal emission between the maximum and minimum of the planet's flux gives the difference in brightness temperature between the day-side and the night-side – marked on Figure 5.1 as the “day-night contrast”.

The final key feature is the hot-spot shift, the offset between the peak of the thermal emission and the position of the secondary eclipse. This corresponds to a shift of the hottest part of the planet away from the substellar point. Position 1 in Figure 5.1 is the secondary eclipse, when the observer looks directly at the substellar point (or would, if the star was not in the way). On a bare rock planet, the substellar point (marked by a dot) and the centre of the hottest hemisphere (marked by an asterisk) would coincide, and there would be no phase offset. If a process redistributes heat around the planet, the hottest hemisphere does not have to coincide with the substellar point.

Chapter 4 shows how an atmosphere on a tidally locked planet can have a hot-spot shifted east of the substellar point. Figure 5.1 shows how the observer looks directly at this eastward shifted hot-spot (at position 2) before the secondary eclipse (position 1). So, the maximum flux is measured before the secondary eclipse, and the difference in orbital phase between these two points gives the longitudinal offset between the substellar point and the hottest part of the planet (or just the “hot-spot”).

Phase curves at optical wavelengths give similar information about the albedo of the planet, showing how features such as clouds affect the reflection of stellar light from the planet at different locations (Parmentier et al., 2016). Dragomir et al. (2012) measured an optical phase curve for 55 Cancri e with a similar form to the thermal phase curve in Demory et al. (2016). This raised the possibility that the reflectance and emission are coupled in some way, such as by temperature-dependent clouds.

Figure 5.2 shows the thermal phase curve measured by Demory et al. (2016) in the  $4.5\text{ }\mu\text{m}$  channel of the *Spitzer* telescope IRAC<sup>1</sup>. The phase curve has a hot-spot shift of  $41^\circ$ , a day-side temperature of  $(2700 \pm 270)$  K, and a night-side temperature of  $(1380 \pm 400)$  K. Figure 5.3 shows maps of brightness temperature reconstructed from the phase curve. Note that this phase curve is plotted by orbital phase, while the simulated curves later in this chapter are plotted by planetary longitude, meaning that they are reversed along the x-axis.

The combination of this large hot-spot shift and large day-night temperature contrast presents a puzzle. 1D analytic models of circulation on tidally locked planets suggest that a large hot-spot shift implies a strong heat redistribution from day-side to night-side (Zhang and Showman, 2017). But in the same models, a large day-night contrast implies weak heat redistribution. So, the solutions of Zhang and Showman (2017) cannot easily match both of these results.

Angelo and Hu (2017) reanalysed the phase curve and suggested a hot-spot shift

---

<sup>1</sup>Infrared Array Camera

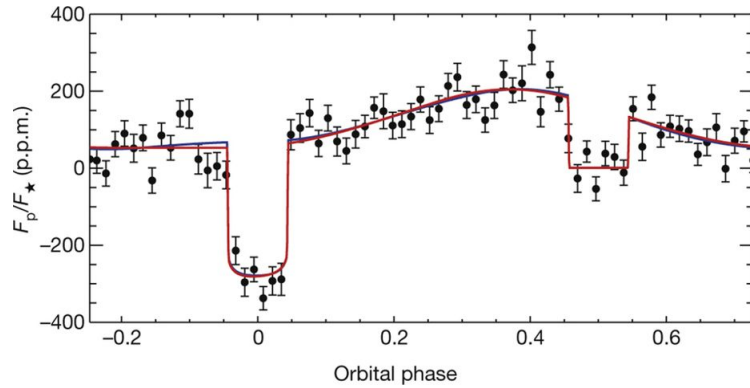


Figure 5.2: The thermal phase curve observed at  $4.5 \mu\text{m}$  by Demory et al. (2016), showing an offset of the maximum flux from the secondary eclipse, corresponding to a hot-spot shift. Reproduced from Demory et al. (2016) with permission.

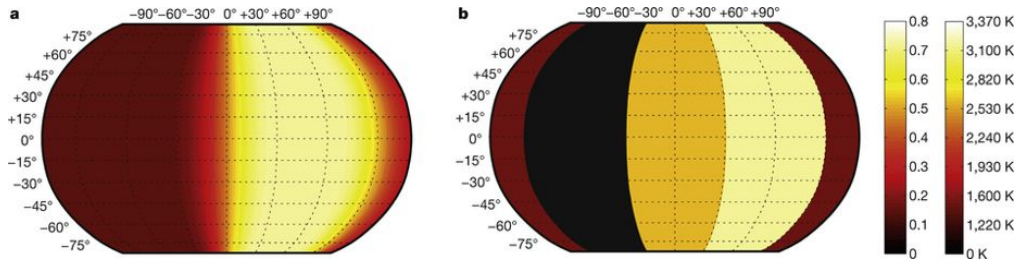


Figure 5.3: The temperature map reconstructed by Demory et al. (2016) from the phase curve in Figure 5.2, showing a hot-spot shift of  $41^\circ$ , a day-side temperature of  $(2700 \pm 270)$  K, and a night-side temperature of  $(1380 \pm 400)$  K. Reproduced from Demory et al. (2016) with permission.

of  $34^\circ$ , a day-side temperature of  $(2700 \pm 160)$  K, and a night-side temperature of  $(1600 \pm 140)$  K. These are both smaller than the hot-spot shift and day-night contrast reconstructed by Demory et al. (2016), although the two studies are still within error of each other. They are also more consistent with the GCM simulations in this chapter and the predictions of Zhang and Showman (2017), as the smaller hot-spot shift and day-night contrast require a less extreme atmospheric circulation.

### 5.1.3 Atmospheric Composition

It is not clear what sort of atmosphere, if any, to expect on a planet like 55 Cancri e. An atmosphere like a hot Jupiter with a low molecular weight seems unlikely, given the

planet's proximity to its star and correspondingly high temperatures and high-energy radiation, which would cause atmospheric escape of lighter components (Demory et al., 2016). Gillon et al. (2012) used the observational mass and radius to suggest that there is an atmosphere composed of high molecular weight volatiles.

Tsiaras et al. (2016) reported the detection of an atmosphere due to spectroscopic deviations from a bare-rock planet, using observations in the near-infrared with the WFC3 camera of the Hubble Space Telescope (HST). In this chapter, I avoid direct questions of atmospheric composition or origin, focusing on what bulk properties – surface pressure, mean molecular weight, and longwave optical thickness – could be consistent with the observed thermal phase curve.

## 5.2 Simplified Scaling Theory

The section applies scaling relations from the idealised 1D atmospheric models of Zhang and Showman (2017) to understand how the atmospheric properties affect the observed phase curve. The relations predict the effect of the bulk properties of the atmosphere on the main features of the phase curve – the hot-spot shift and day-night contrast. I will describe these scaling relations and show how they were used to select a parameter space of atmospheres that could fit the observed phase curve.

### 5.2.1 1D Circulation Model

Zhang and Showman (2017) model the circulation on a tidally locked planet with a 1D differential equation on the equator where heat transport is determined by a balance of the radiative timescale and advective timescale (Komacek and Showman, 2016). The resulting scaling relations are similar to those derived from the shallow-water system in Chapter 4. The important timescales in these relations are the radiative timescale  $\tau_{\text{rad}}$ , the wave timescale  $\tau_{\text{wave}}$ , and the advective timescale  $\tau_{\text{adv}}$ . The radiative

timescale is the typical timescale of changes due to radiative forcing:

$$\tau_{\text{rad}} \sim \frac{p_{\tau=1}}{\mu g} \frac{c_p}{4\sigma T^3}, \quad (5.1)$$

where  $p_{\tau=1}$  is the pressure at which the optical thickness is unity,  $\mu$  is the mean molecular weight,  $T$  is the equilibrium temperature of the planet, and  $c_p$  is the atmospheric molar heat capacity. The wave timescale is the time for planetary-scale equatorial waves to propagate horizontally:

$$\tau_{\text{wave}} = L/NH, \quad (5.2)$$

where  $L$  is the radius of the planet,  $N$  is the buoyancy frequency of the atmosphere, and  $H$  is the atmospheric scale height. The advective timescale is the time for the mean zonal flow (the equatorial jet) to advect air around the planet:

$$\tau_{\text{adv}} = L/U_{\text{eq}}. \quad (5.3)$$

Here,  $U_{\text{eq}}$  is the “wind speed that would result from acceleration of the wind from day to night due to the day-night pressure gradient if the day-night temperature difference were in radiative equilibrium and if the Rossby number exceeds unity” ([Zhang and Showman, 2017](#)):

$$U_{\text{eq}} = \left( R \Delta T_{\text{eq}} \Delta \ln p / 2\mu \right)^{1/2}, \quad (5.4)$$

where  $\Delta T_{\text{eq}}$  is the day-night temperature difference, and “ $\Delta \ln p$  is the difference in log pressure between some deep pressure where the day-night temperature difference is small (10 bars in the theory and simulations from [Komacek and Showman \(2016\)](#)) and some smaller pressure of interest in the observable atmosphere” ([Zhang and Showman, 2017](#)).

### 5.2.2 Hot-Spot Shift

The hot-spot shift is an observable consequence of the atmospheric circulation on a tidally locked planet. [Zhang and Showman \(2017\)](#) predict the longitude of the maximum temperature  $\lambda_m$  (i.e. the hot-spot shift) to be given by:

$$\sin(\lambda_s - \lambda_m) e^{\lambda_m/\xi} = \frac{\eta}{\xi \cos \lambda_s}, \quad (5.5)$$

where

$$\eta = \frac{\xi}{1 + \xi^2} \frac{e^{\frac{\pi}{2\xi}} + e^{\frac{3\pi}{2\xi}}}{e^{\frac{2\pi}{\xi}} - 1}, \quad (5.6)$$

for  $\xi = \tau_{\text{rad}}/\tau_{\text{adv}}$  and  $\lambda_s = \tan^{-1} \xi$ . When  $\lambda_m$  is small in this expression,  $\lambda_m \approx \lambda_s$  and it reduces to the same expression as in Chapter 4,  $\lambda_m = \tan^{-1}(\tau_{\text{rad}}/\tau_{\text{adv}})$ . This expression assumes that the hot-spot shift depends on a balance of eastward heat transport versus radiation to space. It does not represent the effect of the stationary waves that are so important to the global temperature distribution, so does not apply in regimes where these dominate or in regions away from the equator ([Perez-Becker and Showman, 2013](#); [Hammond and Pierrehumbert, 2018](#)).

### 5.2.3 Day-Night Contrast

The day-night contrast on a tidally locked planet refers to the fractional difference between the temperature difference between the day-side and the night-side, compared to the temperature difference that would be expected in radiative equilibrium.

[Zhang and Showman \(2017\)](#) use the 1D model to predict the day-night contrast to be:

$$A = \frac{\Delta T}{\Delta T_{\text{eq}}} \sim 1 - \frac{2}{\alpha + \sqrt{\alpha^2 + 4\gamma^2}} \quad (5.7)$$

where the non-dimensional parameters  $\alpha$  and  $\gamma$  are

$$\alpha = 1 + \frac{\left(\Omega + \frac{1}{\tau_{\text{drag}}}\right) \tau_{\text{wave}}^2}{\tau_{\text{rad}} \Delta \ln p} \quad (5.8)$$
$$\gamma = \frac{\tau_{\text{wave}}^2}{\tau_{\text{rad}} \tau_{\text{adv, eq}} \Delta \ln p}$$

A short radiative timescale  $\tau_{\text{rad}}$  gives a large day-night contrast  $A$ . This is because the heated air on the day-side radiates away its energy faster than it can be transported to the night-side by jet advection or wave transport ([Zhang and Showman, 2017](#); [Hammond and Pierrehumbert, 2017](#)). From the alternative point of view of a global circulation governed by stationary waves, this is because the high radiative damping rate brings the forced wave response into phase with the forcing and strengthens it, as discussed in Chapter 4 ([Hammond and Pierrehumbert, 2018](#)). Section 5.6 compares these mechanisms in more detail.

#### 5.2.4 Parameter Space of Simulations

Figure 5.4 shows a parameter space in atmospheric surface pressure and mean molecular weight, predicted by the 1D scaling relations to be potentially consistent with the observed thermal phase curve. The red line shows the region in which Equation 5.5 predicts the hot-spot shift is greater than  $20^\circ$ . The blue line shows the region in which the day-night contrast is predicted to be greater than 80% by Equation 5.7. The region shaded in green between these lines shows the parameter space that could support both a significant hot-spot shift and day-night contrast. The next section uses this parameter space to select a suite of GCM simulations to compare to the observed phase curve.

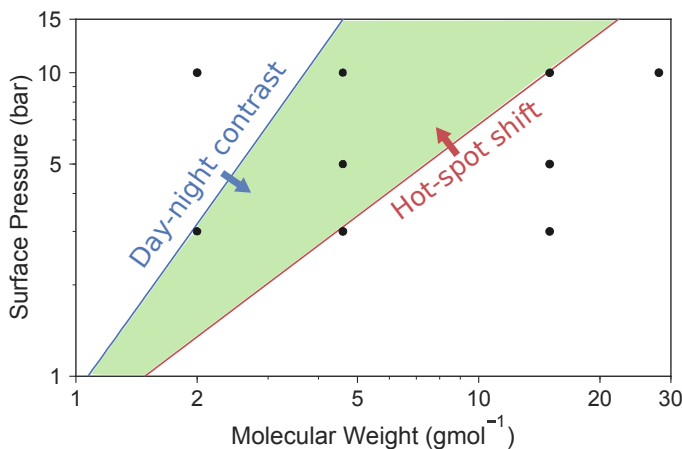


Figure 5.4: The atmospheric parameter space under consideration, where the green region is predicted by the relations of [Zhang and Showman \(2017\)](#) to support both a significant hot-spot shift and day-night contrast. The black points show the parameters of the GCM tests. The hot-spot shift and day-night contrast were calculated with a bulk wind speed of  $1000 \text{ m s}^{-1}$  and a mean temperature  $2000 \text{ K}$ . The two lines correspond to a hot-spot shift of  $20^\circ$  and a day-night contrast of  $80\%$ .

### 5.3 Exo-FMS Configuration

This section describes how the GCM Exo-FMS was configured to simulate a suite of idealised atmospheres on 55 Cancri e. The parameters of the simulations were selected using the scaling relations discussed above, to investigate the atmospheric parameter space that could be consistent with the observations.

Appendix A describes the structure and components of Exo-FMS in detail. It is based on the Flexible Modelling System structure and associated latitude-longitude dynamical core from the Geophysical Fluid Dynamics Laboratory (GFDL). Similar models based on the FMS structure have been used to investigate other terrestrial and tidally locked planets ([Merlis and Schneider, 2010](#); [Heng et al., 2011](#); [Koll and Abbot, 2015, 2016](#)). The general results of simulations of these tidally locked planets are not sensitive to the choice of model, as shown by the similar results of studies using different 3D atmospheric models ([Carone et al., 2014](#); [Kataria et al., 2014](#); [Charnay et al., 2015](#)).

The simulations were all configured with a radius  $r_p = 1.91 R_{Earth}$ , orbital period  $P = 0.737$  days, surface gravity  $g = 21.7 \text{ m s}^{-2}$  ([Demory et al., 2016](#)), incoming stellar flux  $3.55 \times 10^6 \text{ W m}^{-2}$  ([Von Braun et al., 2011](#)), and zero surface and atmospheric albedo. The model itself used a 144 by 96 by 40 grid, with vertical levels set by a hybrid sigma-pressure system, where the top pressure level was approximately  $10^{-5} p_s$  for surface pressure  $p_s$ . A dry convective adjustment scheme was applied to every column, with instantaneous adjustment to a dry adiabat where the profile was convectively unstable. The radiative transfer was modelled with a two-stream semi-grey scheme with variable longwave optical depth that scaled linearly with pressure, and zero shortwave optical depth. The default longwave optical depth of 10 was chosen to approximate the observed day-side temperature.

This optical depth was also consistent with the surface temperature achieved by a 10 bar H<sub>2</sub> atmosphere, using a one-dimensional radiative-convective model with two-stream radiative transfer calculated using the H<sub>2</sub> collisional opacity ([Pierrehumbert and Gaidos, 2011](#)). This corresponds to an opacity  $\kappa$  of  $22.4 \text{ cm}^2 \text{ kg}^{-1}$ , which I used in all the tests apart from those where the opacity was explicitly varied. In reality,  $\kappa$  could be different, and would not scale linearly with pressure – a more realistic representation such as that in Chapter 6 would be needed to interpret future observations.

The simulations were initialised from rest with every atmospheric column on a dry adiabat from a specified surface temperature, up to a given pressure level where the profile was set to an isothermal stratosphere. The simulation results were not sensitive to the initial conditions, owing to the short radiative timescale of the atmosphere. The atmosphere reached radiative equilibrium when the outgoing longwave radiation and top-of-atmosphere temperatures stopped evolving. Dynamical equilibrium was reached when the maximum zonal winds and total angular momentum stabilised. All the results presented are averaged over the final 10 days of simulation runs of at least 50 Earth days, after the model reached equilibrium.

| Test | Composition                     | $p_s$ | $\mu$ | $\tau_\infty$ | Hot-Spot Shift | Day-Night Contrast |
|------|---------------------------------|-------|-------|---------------|----------------|--------------------|
| 1    | H <sub>2</sub>                  | 10    | 2.0   | 8             | +45°           | 100 K              |
| 2    | N <sub>2</sub>                  | 10    | 28.0  | 8             | 0°             | 750 K              |
| 3    | H <sub>2</sub> + N <sub>2</sub> | 10    | 4.6   | 8             | +30°           | 200 K              |
| 4    | H <sub>2</sub> + N <sub>2</sub> | 5     | 4.6   | 8             | +25°           | 250 K              |
| 5    | H <sub>2</sub> + N <sub>2</sub> | 3     | 4.6   | 8             | +15°           | 300 K              |
| 6    | H <sub>2</sub> + N <sub>2</sub> | 10    | 15.0  | 8             | 0°             | 1500 K             |
| 7    | H <sub>2</sub> + N <sub>2</sub> | 5     | 15.0  | 8             | 0°             | 550 K              |
| 8    | H <sub>2</sub> + N <sub>2</sub> | 3     | 15.0  | 8             | 0°             | 600 K              |
| 9    | H <sub>2</sub> + N <sub>2</sub> | 5     | 14.6  | 2             | +20°           | 200 K              |
| 10   | H <sub>2</sub> + N <sub>2</sub> | 5     | 4.6   | 4             | +20°           | 250 K              |
| 11   | H <sub>2</sub> + N <sub>2</sub> | 5     | 4.6   | 8             | +25°           | 250 K              |

Table 5.1: The suite of GCM simulations, testing the effect of varying the atmospheric mean molecular weight  $\mu$ , surface pressure  $p_s$ , and optical thickness  $\tau_\infty$ . The hot-spot shifts are rounded to the nearest 5°, and the day-night contrasts to the nearest 50 K. The observed phase curve has a hot-spot shift of  $+41 \pm 12$ ° and a day-night contrast of  $(1300 \pm 670)$  K. Test 4 is the “best-fit” test discussed in Section 5.6.

The suite of GCM tests listed in Table 5.1 were chosen to cover the region that Figure 5.4 predicted to fit the observations, according to the scaling relations in Section 5.2,. Some simulations test the effect of a particular parameter in more detail, such as Tests 3, 4, and 5, which test the effect of changing the surface pressure  $p_s$ . The next section will discuss the simulations and show the effect of the surface pressure, mean molecular weight, and longwave optical depth on the global circulation and thermal phase curve.

## 5.4 Simulation Results

This section discusses the results of the simulations in Exo-FMS. I will show the effect of varying the mean molecular weight, surface pressure, and optical thickness of the atmosphere, and compare the results to the theory in Section 5.2. The simulations generally follow the scaling relations discussed above, but none of them exactly match the temperature distribution inferred from the observed phase curve.

### 5.4.1 Effect of Mean Molecular Weight

The first set of tests investigate the effect of the mean molecular weight  $\mu$  on the global circulation and thermal phase curve. I selected a range of molecular weights from  $2.0 \text{ g mol}^{-1}$  ( $\text{H}_2$ ) to  $28.0 \text{ g mol}^{-1}$  ( $\text{N}_2$ ) from the parameter space in Section 5.2.4.

Test 1 is a pure  $\text{H}_2$  atmosphere with  $\mu = 2.0 \text{ g mol}^{-1}$ , surface pressure  $p_s = 10 \text{ bar}$  and optical thickness  $\tau_\infty = 8.0$ . Section 5.2 predicts that this atmosphere will have a large hot-spot shift but a small day-night contrast, due to its high specific heat capacity, giving a long radiative timescale. Figure 5.5 confirms this prediction, showing that it has a large hot-spot shift in the second plot showing the mid-atmosphere, with the hottest hemisphere centred at about  $45^\circ$ . [Kataria et al. \(2014\)](#) also showed that a lower molecular weight atmosphere had a larger hot-spot shift in simulations of the atmosphere of a super-Earth. Figure 5.5 also shows that the day-night contrast is small, because of the highly efficient heat redistribution. The surface air temperature in the first plot does not show such a large hot-spot shift, as it is closely coupled to the incoming stellar flux. The third plot shows the brightness temperature, which is calculated directly from the outgoing longwave radiation of the semi-grey radiative transfer scheme. This corresponds to a very low pressure due to the high longwave optical depth of the atmosphere, meaning that the brightness temperature is almost homogeneous as it probes the upper atmosphere where the heat circulation is very efficient.

Test 2 is a pure  $\text{N}_2$  atmosphere with  $\mu = 28.0 \text{ g mol}^{-1}$ , surface pressure  $p_s = 10 \text{ bar}$  and optical thickness  $\tau_\infty = 8.0$ . Section 5.2 predicts that this atmosphere will have a large day-night contrast but a small hot-spot shift, due to its low specific heat capacity, giving a short radiative timescale. Figures 5.5 and 5.8 confirm this prediction, showing a large difference in day-side and night-side temperature at all pressure levels, and in the brightness temperature. The hot-spot is centred on the substellar point, also

confirming the prediction of a small or zero hot-spot shift.

These two extremes of  $\mu$  behave as predicted by Section 5.2, suggesting that an intermediate value of  $\mu$  may fit the observations better. Test 3 is a mixture of H<sub>2</sub> and N<sub>2</sub>, with  $\mu = 4.6 \text{ g mol}^{-1}$ , surface pressure  $p_s = 10 \text{ bar}$  and optical thickness  $\tau_\infty = 8.0$ . Figure 5.5 shows that at the half-surface-pressure level, and in the brightness temperature, there is a significant hot-spot shift and day-night contrast (although not as large as that observed by [Demory et al. \(2016\)](#)). I will simulate the thermal phase curves of these tests later for a more direct comparison to the observations.

The rest of this chapter will show the effect of the surface pressure and longwave optical thickness on the global circulation and simulated phase curve. Of these first three tests, Tests 1 and 2 reproduce the observed hot-spot shift or day-night contrast respectively – but not both. Test 3 has a significant hot-spot shift and day-night contrast, but neither is as large as the observations. All these tests qualitatively match the predictions of the scaling relations in Section 5.2.

#### 5.4.2 Effect of Surface Pressure

This section investigates the effect of the surface pressure on the global circulation. Section 5.2 predicts that the surface pressure has a similar effect to the mean molecular weight, as they both modify the radiative timescale. At low surface pressures, the radiative timescale is short so there should be a large day-night contrast and small hot-spot shift, and vice versa. The surface pressure and the specific heat capacity have a similar effect, as they both affect the radiative timescale in the same way in Section 5.2.

Figure 5.6 shows the temperature at the half-surface-pressure level for these tests. The first row shows Tests 4, 5, and 6, with  $\mu = 4.6 \text{ g mol}^{-1}$  and  $p_s = 10, 5, \text{ and } 3 \text{ bar}$ . As expected, the tests with higher  $p_s$  have a larger hot-spot shift and smaller day-night contrast. The second row shows Tests 7, 8, and 9 with  $\mu = 15.0 \text{ g mol}^{-1}$  and  $p_s = 10,$

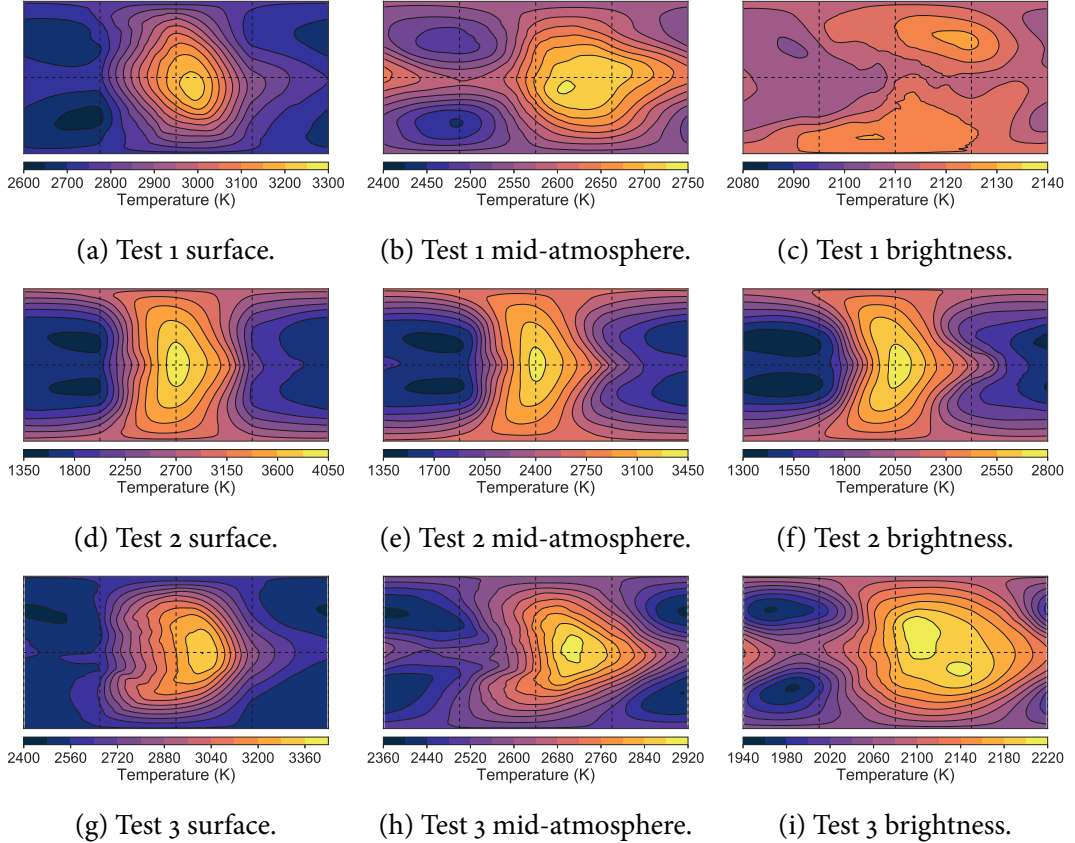


Figure 5.5: 10-day time-averaged maps of different temperature fields for Tests 1, 2, and 3. Each row is a different test. The first column shows the surface air temperature, which has the strongest day-night contrast as it is closely coupled to the surface temperature and stellar forcing. The second column is the temperature at the half-surface-pressure level, which can support both a large hot-spot shift and day-night contrast. The third column is the brightness temperature calculated from the semi-grey radiative transfer scheme, which generally corresponds to a low atmospheric pressure, due to the high optical thickness.

5, and 3 bar. Again, the tests with higher  $p_s$  have a larger hot-spot shift and smaller day-night contrast. In comparison with the corresponding tests in the first row, all these tests have a larger day-night contrast and smaller hot-spot shift due to their higher mean molecular weight.

Test 3, with  $\mu = 4.6 \text{ g mol}^{-1}$  and  $p_s = 10 \text{ bar}$ , is consistent with the hot-spot shift and day-night contrast of the observed phase curve, but has a hotter night-side than the observations. Test 4 with  $\mu = 4.6 \text{ g mol}^{-1}$  and  $p_s = 5 \text{ bar}$  is a better fit as it matches the day-side of the observations, and comes closer to matching the night-side. So, I will consider Test 4 with  $p_s = 5 \text{ bar}$  to be the “best-fit” test (although none of the simulations exactly matched the observations).

The simulations show that a low mean molecular weight of  $\mu = 2.0 \text{ g mol}^{-1}$  or below cannot be consistent with the observations as the day-night contrast would be too small, as predicted by the scaling relations of [Zhang and Showman \(2017\)](#). They also show that a high mean molecular weight of  $\mu = 28.0 \text{ g mol}^{-1}$  or above does not fit the observations (in this range of surface pressures) as the hot-spot shift would be too small. Chapter 6 will investigate a larger range of pressures and consider the possibility of a higher mean molecular weight atmosphere. In the current chapter, the simulations suggest an atmosphere which is heavier than  $\mu = 2.0 \text{ g mol}^{-1}$ , with a surface pressure in the range 1 to 10 bar. These conclusions are similar to other studies using different observations and models ([Winn et al., 2011](#); [Angelo and Hu, 2017](#)).

The rest of this chapter discusses the effect of the longwave optical thickness and other bulk parameters on the circulation and vertical structure of the atmosphere. I will suggest that night-side cloud formation could be responsible for the low temperatures observed on the night-side, which would explain why the GCM simulations are consistently too hot on their night-sides.

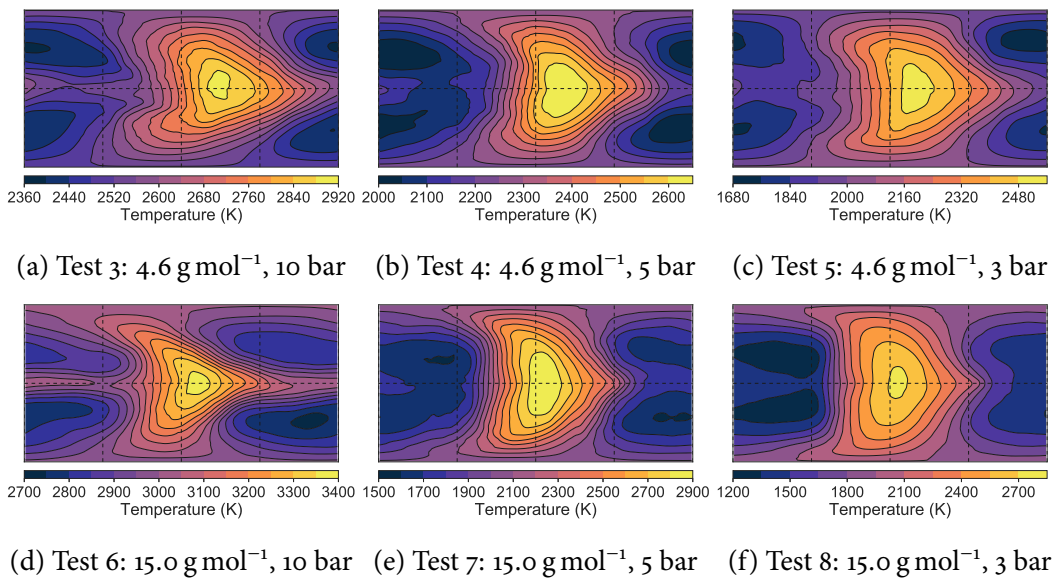


Figure 5.6: Temperatures at half-surface-pressure averaged over 10 days, for atmospheres with mean molecular weights of either  $\mu = 4.6 \text{ g mol}^{-1}$  or  $15.0 \text{ g mol}^{-1}$ , and surface pressures of 3, 5, or 10 bar.

#### 5.4.3 Effect of Optical Thickness

This section will show that the main effect of changing the longwave optical thickness  $\tau_\infty$  is to change the global mean temperature without strongly affecting the circulation and the shape of the phase curve. The high day-side brightness temperature observed by Demory et al. (2016) requires significant greenhouse heating, which approximately constrains the longwave optical depth of the atmosphere.

Figure 5.7 shows three atmospheres based on the “best-fit” Test 4. Tests 7, 8, and 9 have  $p_s = 10 \text{ bar}$  and  $\mu = 4.6 \text{ g mol}^{-1}$ , with  $\tau_\infty = 8.0, 4.0$ , and  $2.0$ . Section 5.2 predicts that  $\tau_\infty$  will not have a large effect on the hot-spot shift and fractional day-night contrast, beyond scaling the global mean temperature. This is confirmed by Figure 5.7, where the temperature distributions have different magnitudes but similar patterns. The high day-side temperature of Test 11 matches the day-side temperature of the phase curve best, but its night-side temperature is much higher than the observations. The tests with lower optical thickness match the night-side observations better but

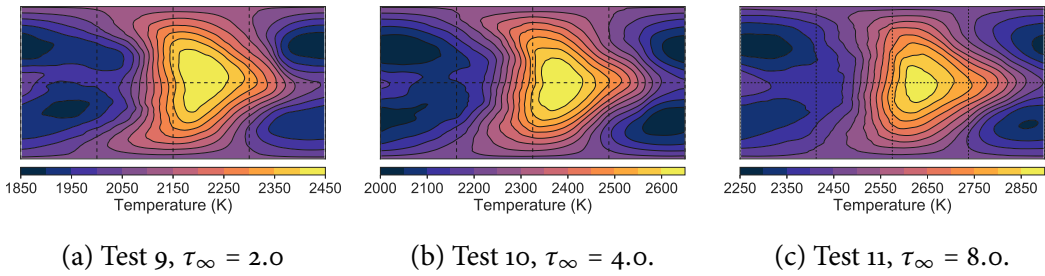


Figure 5.7: The temperature at the half-surface-pressure level for Tests 10, 11, and 12, with  $\mu = 4.6 \text{ g mol}^{-1}$ , surface pressure 5 bar and optical thicknesses of 2.0, 4.0, and 8.0. Increasing the optical thickness increases the global mean temperature but does not significantly affect the global circulation and temperature distribution.

the day-side observations worse. This is another example of the difficulty in fitting the observed phase curve, which appears to require a very specific atmospheric structure. These tests show that the longwave optical depth of the atmosphere must be in the range  $\tau_\infty = 8.0$  to 2.0, or the mean temperature of the atmosphere would be too high or too low. Figure 5.13 will show later that varying  $\tau_\infty$  just scales the magnitude of the thermal phase curves, with no significant differences in hot-spot shift or fractional day-night contrast.

#### 5.4.4 Vertical Temperature Structure

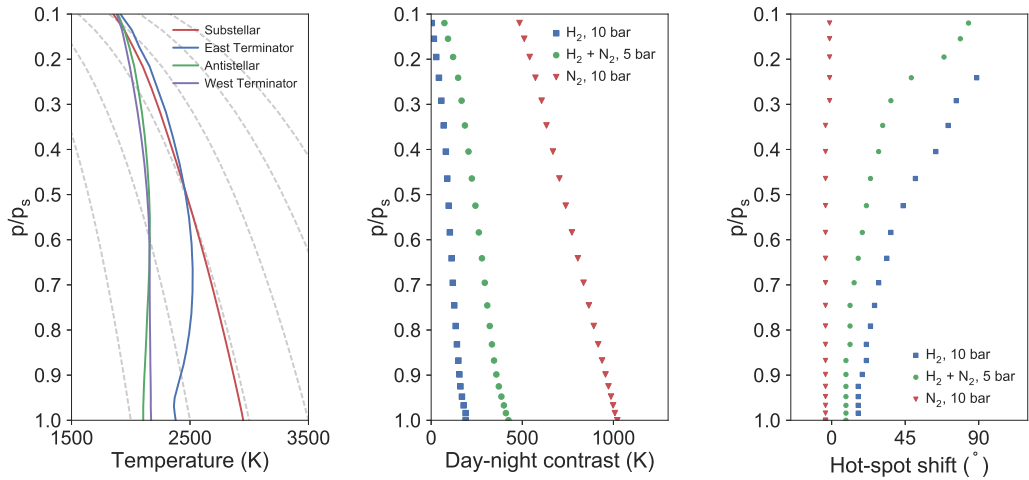
The thermal phase curve that would result from any of these simulations depends on the radiative properties of the atmosphere in the wavelength range of the observations. This chapter will assume that the outgoing radiation can be approximated as the emission from a single pressure level in the atmosphere – see Chapter 6 for more detailed modelling of the outgoing thermal emission.

The phase curve of the emission from a radiating level near the surface will have almost no hot-spot shift and a large day-night contrast, as it is closely coupled to the surface temperature which is dominated by the incoming shortwave stellar radiation. If the radiating level is very high in the atmosphere, the phase curve could be almost

flat due to efficient circulation as in Test 1, or it could still have a large day-night contrast as in Test 2. Generally, to fit the observed large day-night contrast and large hot-spot shift the radiating level must be somewhere between these two extremes. In this section, I will examine the vertical structure of the test atmospheres, and discuss how the observable quantities vary with pressure level.

Figure 5.8a shows temperature-pressure profiles of several vertical columns spaced evenly around the equator of Test 4. The red line at the substellar point is convective at high pressures, driven by the stellar heating at the surface. The blue line at the east terminator has a temperature inversion above the lower atmosphere, caused by the hot-spot shift that is strongest at the level of the equatorial jet at approximately 0.5 p<sub>s</sub>. It might be possible to detect an inversion due to atmospheric dynamics on a tidally locked planet with a strong circulation with phase-resolved emission spectroscopy (Stevenson et al., 2014). The temperature profile at the antistellar point is almost isothermal, as it is heated high in the atmosphere by the global circulation, rather than at the surface. These profiles show that the observable day-night contrast depends on the radiating level and thermal structure, as at the surface the temperature profiles are well separated but at low pressure they are almost uniform.

Figure 5.8b plots the day-night contrast at each pressure level in the atmosphere for Tests 1, 2, and 4. This suggests that the large observed day-night contrast corresponds to a radiating level near the surface. However, the high longwave optical thickness in the GCM means that the outgoing radiation in the model comes from high in the atmosphere, as shown in Figure 5.5. I will show later that the phase curves calculated from the outgoing radiation in the semi-grey scheme always have a day-night temperature contrast that is smaller than the observations. This suggests that in reality the atmospheric longwave thickness is high to explain the observed day-side temperature, but that the 4.5 μm band corresponds to a region of lower absorption with a radiating level low in the atmosphere to explain the large day-night contrast.



(a)  $T(p)$  profiles for columns on the equator of Test 4. Dry adiabats are plotted in grey. (b) Day-night contrast at each pressure level, showing how it is larger at higher pressures.. (c) Hot-spot shift at each pressure level, showing how it increases with height.

Figure 5.8: The vertical structure of Test 4, and the hot-spot shift and day-night contrast of Tests 1, 2, and 4. The temperature profiles tend to follow the dry adiabat at high pressures on the day-side, but can become isothermal or inverted on the night-side. The lower atmospheres have a larger day-night contrast, and the upper atmospheres have a larger hot-spot shift. This suggests that the observed phase curve corresponds to emission from an intermediate pressure level.

Figure 5.8c shows how the hot-spot shift varies with atmospheric pressure. It is always small close to the surface, where the temperature is closely coupled to the incoming stellar radiation due to the lack of shortwave absorption in these simulations. The hot-spot shift generally increases with height, as the zonal flow increases further from the surface up to a maximum at the centre of the jet. The heat redistribution can be so effective high in the atmosphere that it becomes almost isothermal, as shown by the brightness temperature of Test 1 in Figure 5.5.

The next section will investigate the same effects of atmospheric parameters on the global circulation by simulating the phase curves of each test. These will show the same trends as this section, and confirm the predictions of the scaling relations of [Zhang and Showman \(2017\)](#).

## 5.5 Simulated Observations

This section will discuss phase curves calculated from the GCM simulations shown previously. The 4.5  $\mu\text{m}$  phase curves were calculated using either the outgoing longwave radiation from the grey-gas model, or for a specific radiating level using the temperature of that level. This flux was integrated over the hemisphere centred on each grid cell around the equator, to produce the phase curve (Cowan and Agol, 2008):

$$I_p(\xi) = \frac{\int_{-\pi/2}^{\pi/2} \int_{-\xi-\pi/2}^{-\xi+\pi/2} I_{4.5}^\uparrow|_{p=0} \cos(\lambda + \xi) \cos^2(\theta) d\lambda d\theta}{\int_{-\pi/2}^{\pi/2} \int_{-\xi-\pi/2}^{-\xi+\pi/2} \cos(\lambda + \xi) \cos^2(\theta) d\lambda d\theta} \quad (5.9)$$

where the phase angle is  $\xi$ , the outgoing 4.5  $\mu\text{m}$  flux is  $I_{4.5}^\uparrow|_{p=0}$ , longitude is  $\lambda$ , and latitude is  $\theta$ . The phase curves are plotted as a ratio of planetary flux  $F_p$  to stellar flux  $F_\oplus$ :

$$\frac{F_p}{F_\oplus} = \frac{I_p}{I_\oplus} \left( \frac{r_p}{r_\oplus} \right)^2 \quad (5.10)$$

where the ratio of planetary radius to stellar radius is  $\frac{r_p}{r_\oplus} = 0.0187$  and the stellar emission is determined by its effective temperature of 5196 K (Von Braun et al., 2011).

### 5.5.1 Effect of Radiating Level

Section 5.4.4 showed how the hot-spot shift and day-night contrast vary with pressure level due to changes in stellar forcing, radiative timescale, and jet speed. Figure 5.9 shows phase curves calculated from the emission at 4.5  $\mu\text{m}$  of different radiating levels in Test 4, which show the same trends in hot-spot shift and day-night contrast as the analysis in Section 5.4.4.

The phase curve from a pressure level close to the surface has a large amplitude and small phase shift as explained previously. High in the atmosphere, the phase

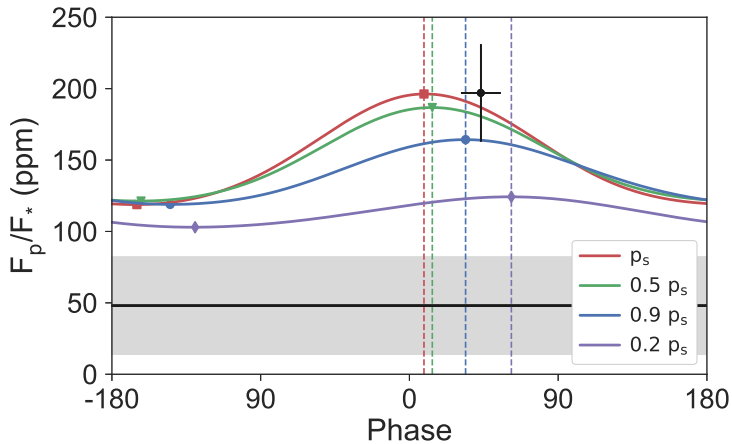


Figure 5.9: Thermal phase curves calculated at different radiating levels in Test 4. Moving the radiating level to lower pressures has a similar effect to decreasing the mean molecular weight, as shown in Figures 5.10 and 5.11. The black point shows the maximum (day-side) observed flux, and the black line shows the minimum (night-side) observed flux.

curve has a smaller amplitude and large phase shift. I will show later in Figure 5.10 that the mean molecular weight and radiating level are somewhat degenerate in their effects on the phase curve, as they both affect the radiative timescale which then changes the day-night contrast and hot-spot shift in the same way. Figures 5.9 and 5.10 show phase curves varying from a case with low amplitude and large phase shift, to a case with high amplitude and low phase shift.

Observations at multiple wavelengths corresponding to multiple radiating levels could break this degeneracy. As discussed earlier, it is possible to explain the high observed brightness temperature and large hot-spot shift if the atmospheric opacity in the 4.5  $\mu\text{m}$  *Spitzer* bandpass is lower than average in the longwave region – i.e., it is observed in a window. A broadband thermal phase curve would constrain the overall brightness temperature, and could be compared with the 4.5  $\mu\text{m}$  observations to test the prediction that they correspond to a window in the atmospheric opacity. Chapter 6 discusses these possibilities in more detail.

### 5.5.2 Effect of Atmospheric Properties

Figure 5.10 shows the phase curves of the simulated atmospheres with different values of mean molecular weight, calculated using the outgoing longwave radiation from each test. The black points show the maximum and minimum of the observed phase curve. The tests with very high or low molecular weight do not fit the observations well, as discussed previously. The phase curve of Test 1 (pure H<sub>2</sub>) has a large phase shift, but a very small amplitude due to its efficient heat transport from day-side to night-side. This can be explained using the wave-based theory in Chapter 4, as the low molecular weight would give a long radiative damping timescale, reducing the strength of the day-night wave-1 response, and producing a more zonally uniform temperature field like the solution in Figure 4.11a.

The phase curve of Test 2 fits the day-night contrast but not the hot-spot shift, owing to its high radiative damping rate. The phase curve of Test 4 fits the observations better (as did its temperature distribution in Section 5.4.2) – it has a large amplitude and offset, although neither is quite as large as those in the observations. The relatively low amplitude of all the tests in Figure 5.10 is due to the use of the model OLR in the phase curve. As discussed above, it may be that the observations at 4.5 μm correspond to an atmospheric window, so actually reflect the temperature of a lower level in the atmosphere which would give a phase curve with a larger amplitude.

To test this idea, Figure 5.11 shows the phase curves corresponding to the brightness temperature of a radiating level at half-surface-pressure for the same tests. Test 4 fits the observations better in this figure than in Figure 5.10 where the model OLR was used. In this case, it has a larger amplitude and a large phase shift due to the lower radiating level. The night-side flux is still higher than the observations as in most of the tests – later, I will discuss the possibility of night-side cloud formation producing a difference between the model and the observations.

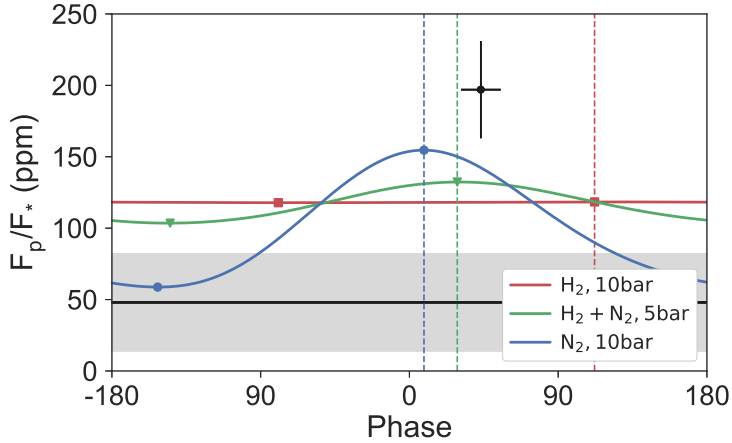


Figure 5.10: Simulated  $4.5 \mu\text{m}$  phase curves calculated from the grey-gas OLR of Tests 1, 2, and 4. The red curve is the Test 1, the 10 bar  $\text{H}_2$  atmosphere, which has such efficient heat transport that it has a large peak offset and very small amplitude. The blue curve is Test 2, the 10 bar  $\text{N}_2$  atmosphere, with very weak heat transport so a large amplitude and peak offset. The green curve is Test 4, the 5 bar  $\text{H}_2+\text{N}_2$  atmosphere, with a significant offset and amplitude. The offset and amplitude are not as large as the [Demory et al. \(2016\)](#) measurements, shown by the black point and line (with their errors shown by the bars and the shaded area).

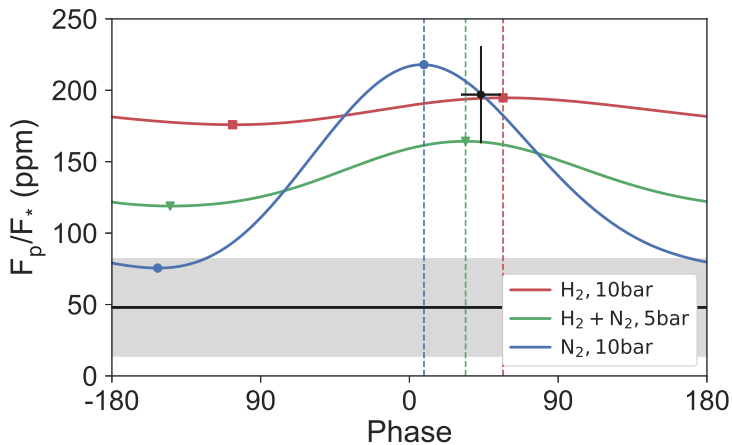


Figure 5.11: Simulated phase curves for the emission from a radiating level at half-surface-pressure for Tests 1, 2, and 4. The amplitude and offset are larger than the phase curves calculated from the OLR in Figure 5.10. The offset and amplitude are not as large as the [Demory et al. \(2016\)](#) measurements, but Figure 5.14 shows that the  $\text{H}_2+\text{N}_2$  atmosphere (green curve) could match the observations given night-side cloud formation as discussed in Section 5.5.3.

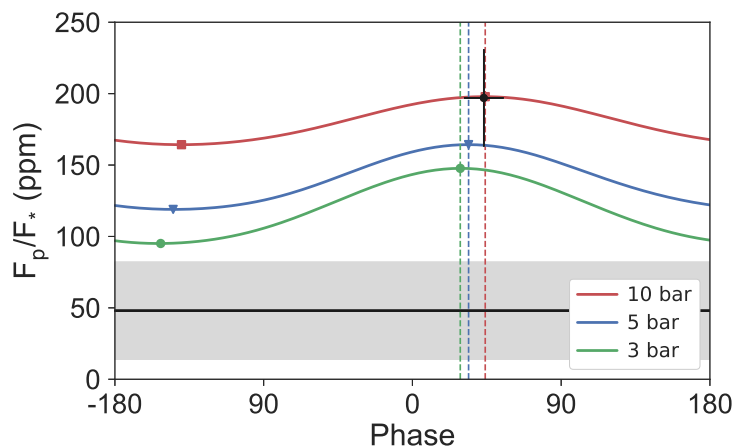


Figure 5.12: Phase curves calculated from the emission of the half-surface-pressure level of the  $4.6 \text{ g mol}^{-1} \text{ H}_2 + \text{N}_2$  atmospheres (Tests 3, 4, and 5) with surface pressures of 3, 5, and 10 bar, corresponding to the temperature maps in Figure 5.6.

Figure 5.12 shows the phase curves of the tests of different surface pressures in Section 5.4.2. These show how increasing the surface pressure increases the phase offset and magnitude of the phase curve, due to the longer radiative timescale and increased temperature (owing to the constant opacity). However, the tests with higher pressure also have a higher night-side flux due to the long radiative timescale, so the overall fractional amplitude of the curve decreases. The case with  $p_s = 10 \text{ bar}$  matches the position and magnitude of the observed maximum best, but does not match the observed minimum flux as well as Test 4.

Finally, Figure 5.13 shows the phase curves of the tests in Section 5.4.3, where the optical thickness of Test 4 was varied. As expected from Section 5.2, the optical thickness only affects the magnitude of the phase curve. In particular, the hot-spot shifts are almost identical. The optical thickness is something of a free parameter in this study, which does not affect the global circulation as strongly as the other parameters and can be tuned to match the observed maximum day-side flux.

In summary, the phase curve calculated from the thermal emission of the half-surface-pressure level of Test 4 matched the observations best. In Figure 5.11, it matches

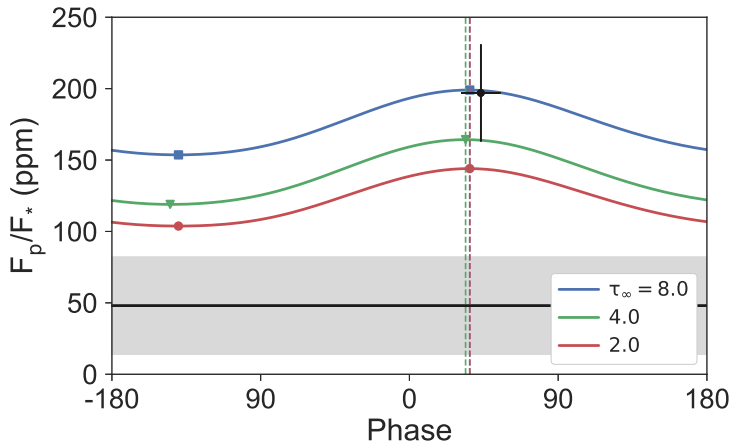


Figure 5.13: Phase curves calculated from the emission of the half-surface-pressure level of the 5 bar  $4.6 \text{ g mol}^{-1} \text{ H}_2 + \text{N}_2$  atmospheres (Tests 9, 10 and 11) with optical thicknesses of 2.0, 4.0, and 8.0, corresponding to the temperature maps in Figure 5.7.

the observed phase curve peak offset and magnitude, but not the observed minimum. The phase curves from the half-surface-pressure level matched the observations much better than the phase curves of the OLR of all the tests, suggesting a high mean longwave opacity with an absorption window at  $4.5 \mu\text{m}$ . I will discuss the possible effects of clouds and condensable species in the next section, focusing on their effect on the thermal emission from the night-side.

### 5.5.3 Condensables and Clouds

All the phase curves calculated from the simulations in this chapter had higher thermal emission from their night-side than was observed in the phase curve. This section will discuss the possibility that clouds form on the night-side, raising the radiating level and lowering the brightness temperature and night-side flux. I will post-process the simulation results to estimate where clouds could form, and will show their effect on the phase curve of the “best-fit” case, Test 4.

These clouds could be formed by condensables such as SiO or Na outgassed from a day-side magma ocean. [Miguel et al. \(2011\)](#) calculated the partial pressures of

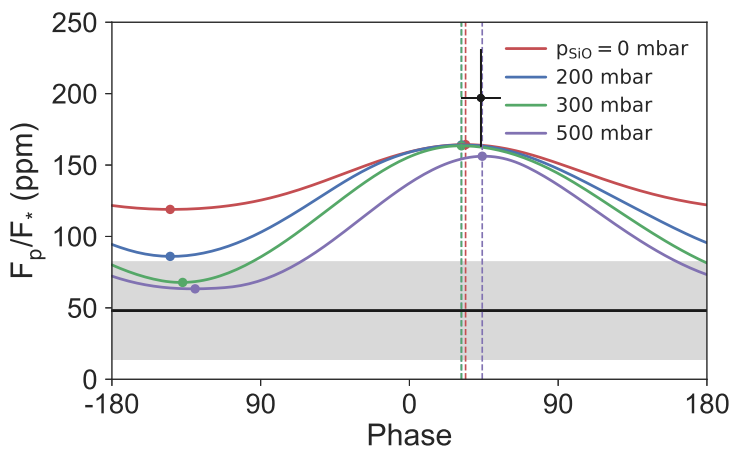


Figure 5.14: Phase curves from the thermal emission of the half-surface-pressure level of Test 4, modified to estimate the effects of cloud formation from different global partial pressures of SiO. The phase curve with a partial pressure of 300 mbar of SiO shows that clouds could form on the day-side at high enough surface partial pressures. The offset and amplitude of the 300 mbar case almost agrees with the observed phase curve within error.

different species outgassed by a silicate magma in a vacuum at different temperatures. A magma ocean at 2700 K would support significant partial pressures of various species, dominated by SiO and Na with partial pressures of about 10 mbar. For the higher surface temperatures of over 3000 K in some tests, SiO becomes more abundant with partial pressures of hundreds of mbar.

I used [Miguel et al. \(2011\)](#) to calculate the partial pressures of SiO and Na based on a range of possible surface temperatures, and assumed that these were mixed uniformly with the rest of the atmosphere. I chose to test whether clouds could form at the top of the atmosphere, as this gives an upper bound on their effect on the thermal emission ([Parmentier et al., 2016](#)). I calculated the saturation vapour pressure of each species at the top of each column ([Wetzel et al., 2013](#)). Estimating the effect of the clouds If the partial pressure is greater than the saturation vapour pressure, I assumed that clouds have formed in that column and set the radiating level to the top of the atmosphere.

This approximate calculation showed that SiO could condense on the night-side of some tests including Test 4, but that Na would not condense in any tests. Figure 5.14 shows that at high enough partial pressures of SiO, the clouds could significantly increase the day-night contrast and phase curve amplitude. For a partial pressure of 300 mbar, the new post-processed phase curve matches the observations of [Demory et al. \(2016\)](#) within error. Figure 5.14 also shows that cloud formation around the cool west terminator can increase the hot-spot shift, for high enough partial pressures of SiO. This is similar to the heterogenous day-side cloud formation shown to affect phase curves by [Parmentier et al. \(2016\)](#). This effect is small in the tests in this chapter, but could be more important for optical phase curves, as clouds can affect the atmospheric albedo very strongly.

In summary, SiO outgassed from a magma ocean is a plausible candidate for a cloud species that would form on 55 Cancri e and affect the observed phase curve. It could form high on the cooler night-side, raising the radiating level and reducing the thermal flux observed from the night-side. This could explain the difference between the modelled and observed night-side flux in the simulations. Further observations at optical wavelengths could test for the presence of clouds, which would help to explain the features of the thermal phase curve ([Dragomir et al., 2012](#)). A better understanding of the species outgassed by a magma ocean would also help to predict the possible cloud formation on 55 Cancri e ([Miguel et al., 2011](#)).

## 5.6 Discussion

The simulation results constrain the atmospheric composition and parameters of 55 Cancri e. Test 4 fitted the observations the most closely. It was a 90%-10% mixture of H<sub>2</sub> and N<sub>2</sub> with  $\mu = 4.6 \text{ g mol}^{-1}$ , specific heat capacity  $7443 \text{ J kg}^{-1} \text{ K}^{-1}$ , optical thickness 4.0, and surface pressure 5 bar. These are similar to the parameters predicted to fit

the observations by the scaling relations of [Zhang and Showman \(2017\)](#) in Figure 5.4. This test did not exactly match the observations of [Demory et al. \(2016\)](#), but confirmed that the scaling relations are broadly accurate. This means that while the idealised model cannot exactly fit the phase curve, it can constrain the atmospheric composition. The results suggest that the atmosphere must have a mean molecular weight above  $2 \text{ g mol}^{-1}$  and a surface pressure above 1 bar. Surface pressures of over 10 bar could be possible given a higher atmospheric molecular weight. The results also point towards the presence of night-side clouds lowering the observed brightness temperature, as have been used to explain observations of hot Jupiters ([Parmentier et al., 2016](#)).

The results in this chapter can be analysed using the wave-based theory in Chapter 4, rather than the advection-based scaling relations of [Zhang and Showman \(2017\)](#). Tests 1 and 2 follow the qualitative predictions of the wave-based theory. Test 1 has a long radiative timescale due to its low mean molecular weight, so has a low radiative damping rate  $\alpha$ . This means that the wave-1 response due to the day-night forcing will be weak in comparison to the wave-0 response due to the geostrophically balanced jet – exactly what is seen in the earlier plots of the zonally homogeneous temperature field of Test 1. In addition, the low damping rate  $\alpha$  in Test 1 is dominated by the jet speed  $U$  in the expression for the hot-spot shift (Equation 4.5). This results in the large hot-spot shift in Figure 5.5.

Test 2 also behaves as expected from the wave-based theory. The short radiative timescale due to the  $\text{N}_2$  atmosphere corresponds to a high radiative damping rate  $\alpha$ , giving a very strong wave-1 response. This causes the strong day-night contrast in Test 2, as this response dominates the wave-0 response from the jet. This test has no hot-spot shift, which can be explained as the high damping rate  $\alpha$  dominating the jet speed  $U$  in Equation 4.5. This means that the real part of the denominator in Equation 4.5 dominates the imaginary part, and the wave response is mostly in

phase with the forcing, giving a pattern similar to the response to forcing plotted in [Matsuno \(1966\)](#).

The wave-based and advection-based theories both give similar predictions for the global circulation patterns. Which theory is a better description of the global circulation of a tidally locked planet? [Perez-Becker and Showman \(2013\)](#) use a theory based on wave transport (not stationary waves, as in Chapter 4) to argue that the wave timescale is key to the global circulation of hot Jupiters, not the advective timescale. This agrees with the wave-based theory in this thesis. [Perez-Becker and Showman \(2013\)](#) suggest that the two different interpretations give similar results because the wave timescale and advective timescale are similar on hot Jupiters.

I suggest that they reflect the same fundamental physics and have different uses. The wave-based theory matches the two-dimensional field seen in the GCM, explains the form of the hot-spot shift and night-side cyclones, and shows how the strengths of the wave response and jet height field vary relative to each other. But, the advection-based theory supplies useful predictions of real observational features such as day-night contrast and hot-spot shift, which are harder to produce from the more idealised wave-based picture. Ultimately, both pictures are useful for different situations. – further work could use the wave-based theory to provide more practical scaling relations for real observable features.

## 5.7 Conclusions

The thermal phase curve of 55 Cancri e observed by [Demory et al. \(2016\)](#) is a puzzle. It implies a large hot-spot shift and a large day-night temperature contrast, features which should be mutually exclusive. This chapter used idealised simulations of atmospheres on 55 Cancri e to show that the phase curve can be partially matched by an atmosphere with the correct properties. The results of these simulations qualitatively

matched the predictions of scaling relations for the global circulation of tidally locked planets.

The “best-fit” atmospheric simulation, Test 4, had a surface pressure of 5 bar and a mean molecular weight of  $4.6 \text{ g mol}^{-1}$ . It matched the phase shift and maximum amplitude of the observed thermal phase curve. However, it was too warm on the night-side to match the observed night-side flux, which was a problem for all the simulations in this chapter. Using a simple estimate of where SiO clouds could form, I showed that night-side cloud formation on the night-side could raise the radiating level and lower the brightness temperature.

The simulations suggested that the observations at  $4.5 \mu\text{m}$  correspond to an absorption window. This was because they required an atmosphere with a strong greenhouse effect, that was emitting from a relatively high pressure at the observed wavelength. Further observations such as broadband phase curve or measurements at optical wavelengths could constrain the temperature of the planet better, or test for the presence of clouds. This would be very valuable to further, more realistic atmospheric modelling.

In summary, this chapter has shown that the observed thermal phase curve of 55 Cancri e can be explained by an atmosphere with a surface pressure of 5 bar and a mean molecular weight of  $4.6 \text{ g mol}^{-1}$ , with a mechanism such as cloud formation to lower the night-side brightness temperature. The suite of GCM tests were consistent with the theories of atmospheric circulation discussed so far in this thesis, but could only partially match the observed phase curve. Chapter 6 will use a model with more detailed radiative transfer to investigate this problem further.

## CHAPTER 6

# *Phase-Resolved Emission Spectra of Potential Climates on 55 Cancri e*

---

Chapter 5 modelled the thermal phase curves of by idealised simulations of 55 Cancri e, and compared them to the observations of Demory et al. (2016). The simple semi-grey radiative transfer focused the modelling on the atmospheric circulation and the effect of bulk properties, but meant that the simulated observations were not realistic. This chapter uses the more realistic radiative transfer scheme *Socrates* to model the atmosphere, and to simulate emission spectra and phase curves (Edwards and Slingo, 1996). This work follows Miguel (2018) and Ito et al. (2015) who simulated emission and transmission spectra for a variety of nitrogen-dominated atmospheres and outgassed rock vapour atmospheres on 55 Cancri e with different absorbing species.

Section 6.1 describes the updated dynamical core and new *Socrates* radiative transfer scheme added to Exo-FMS for the modelling in this chapter. Section 6.2 discusses two control simulations using the new radiative transfer and compares them to the equivalent tests in Chapter 5. I will show how the global circulation is similar for both models, and simulate emission spectra and thermal phase curves to compare to the observations. Neither of these control simulations exactly match the observed phase curve, so in Section 6.3 I will discuss the results of a “best-fit”

simulation with similar bulk properties to Test 4 in Chapter 5. This simulation has a hot-spot shift in its temperature field that does not appear in the thermal phase curve at any wavelength. I will suggest that this is because the atmosphere is too thin, and show that a test with a surface pressure of 100 bar does have a phase shift in its thermal phase curve, which is made possible by its higher surface pressure.

Section 6.5 discusses the results of all the tests, and their implications for a possible atmosphere on 55 Cancri e. I will explain why a sufficiently thick atmosphere is required for a hot-spot shift to produce a phase shift in the thermal phase curve. I will conclude that the simulations are evidence for an atmosphere that is thicker than 10 bar on 55 Cancri e, with a mean molecular weight higher than that of H<sub>2</sub>. Further observations to measure the atmospheric composition and to improve the accuracy of the phase curve would be vital for further modelling.

## 6.1 Improvements to Exo-FMS

This section describes the updated dynamical core and new radiative transfer scheme added to Exo-FMS for the simulations in this chapter. I will discuss how these changes improved the stability of the simulations, and the new capabilities of the radiative transfer scheme.

### 6.1.1 Cubed-Sphere Dynamical Core

The dynamical core of a GCM solves the equations describing the fluid dynamics of the atmosphere on a grid. The simulations in Chapter 5 used a dynamical core on a latitude-longitude grid, which sometimes crashed due to instabilities that appeared to be caused by high winds at the poles of the planet. The cell size is very small at the poles of a latitude-longitude grid, meaning that high winds could easily break the CFL condition ([Courant et al., 1928](#)).

I updated the model to use a newer dynamical core on a cubed-sphere grid to

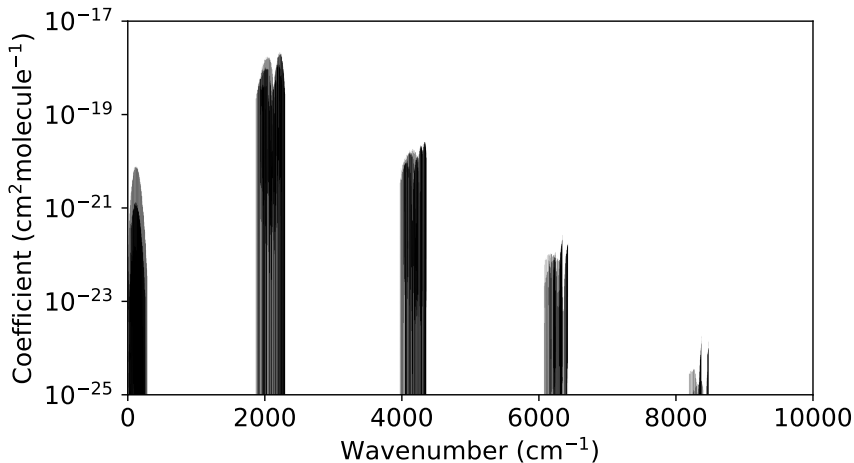


Figure 6.1: The absorption coefficient of CO versus wavenumber at 2500 K and 1 bar from the *HITEMP* database (Rothman et al., 2010). For the simulations in this chapter, the longwave radiation from the surface peaks at about  $5000\text{ cm}^{-1}$  and the incoming stellar radiation peaks at about  $10\,000\text{ cm}^{-1}$ , so the longwave optical depth of the CO-dominated atmospheres in this chapter is higher than the shortwave optical depth.

avoid these problems. Appendix A shows the new grid in more detail, and explains why it avoids the problems at the poles of the latitude-longitude grid. The appendix also shows the new model structure, which is based on a single interface between the dynamical core and physics modules. The updated model runs simulations of 55 Cancri e ran much faster and more stably, which made running the computationally expensive radiative transfer model *Socrates* more feasible.

### 6.1.2 Socrates Radiative Transfer

Chapter 5 used a semi-grey radiative transfer scheme to model the atmosphere of 55 Cancri e. This reduced the complexity and number of parameters of the model, but had two main limitations. First, the simple scheme may not fully represent the details of the real radiative transfer and global circulation. Second, the outgoing longwave radiation had no wavelength dependence in the model, so the  $4.5\text{ }\mu\text{m}$  radiation was post-processed by choosing a particular radiating level. This chapter will show how

this approximation can be inaccurate, producing unrealistically large phase offsets in the thermal phase curve.

For the simulations in this chapter, I coupled the correlated-k radiative transfer scheme *Socrates* ([Edwards and Slingo, 1996](#)) to Exo-FMS. This scheme represents the wavelength-dependent radiative effects of real gases, unlike the wavelength-independent semi-grey model. The simulations used low-resolution spectral data, and were then post-processed using higher-resolution data to produce simulated observations.

The *Socrates* radiative transfer scheme requires a “spectral file” of gaseous absorption data to be generated from line lists. The simulations in this chapter generated this data from line lists in the *HITEMP* database ([Rothman et al., 2010](#)), using the utilities provided with the *Socrates* code ([Edwards and Slingo, 1996](#)). Figure 6.1 shows the absorption spectrum of CO, which was used to produced *Socrates* spectral files for the simulations.

## 6.2 Control Simulation Results

This section discusses two control simulations in the updated model, based on the first two tests using the previous model in Chapter 5. The first control simulation is Test 1, with a 10 bar H<sub>2</sub> atmosphere and a 1% molar concentration of CO. The second simulation, Test 2, has a 10 bar N<sub>2</sub> atmosphere with a 1% molar concentration of CO. The small amounts of CO were not taken into account when calculating the heat capacity of the atmosphere, to keep the bulk thermodynamic properties the same as the equivalent previous tests. Only absorption from CO is considered in the tests, to keep the radiative properties of the atmosphere the same. In reality, collision-induced absorption from H<sub>2</sub> and N<sub>2</sub> would also contribute to the opacity of the atmosphere.

It is not clear what gases are likely to make up the atmosphere of a lava planet.

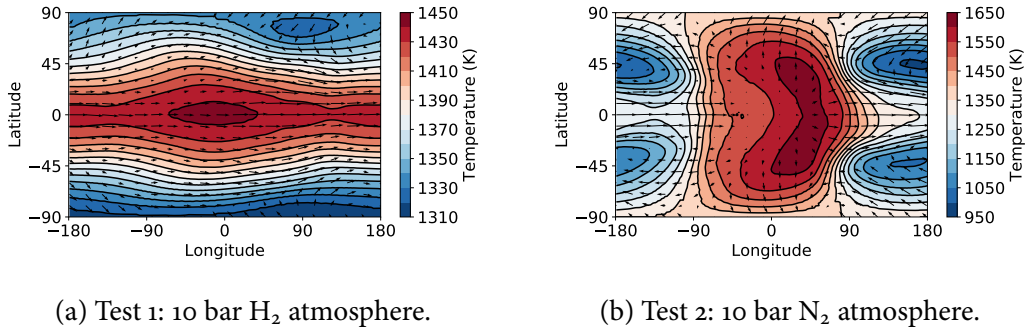


Figure 6.2: Global temperature maps at the 3.57 bar pressure level of the simulations with 1% CO. The mean molecular weight of the atmosphere affects the circulation and temperature distribution in the same way as in Chapter 5.

Miguel (2018) modelled N<sub>2</sub>-dominated atmospheres with absorbers such as CO, CO<sub>2</sub>, and H<sub>2</sub>O. Ito et al. (2015) modelled atmospheres of the rock vapour such as SiO that would be outgassed by a magma ocean. I will investigate the effect of an atmospheric opacity dominated by CO, which is a physically plausible gas with a strong longwave opacity. The modelling in this chapter does not aim to test the hypothesis that there is an atmosphere with exactly this composition on 55 Cancri e, but rather to show the effect of different atmospheric opacities at different wavelengths on the observed phase curve.

This section will compare the global circulation and temperature distribution of the two control tests to the equivalent tests in Chapter 5 to determine if the non-grey radiative transfer makes a significant difference. I will then discuss the features of the emission spectra and thermal phase curves, and show how the radiative properties of the atmosphere can be degenerate with the strength of the circulation. I will conclude that the realistic radiative transfer does not greatly affect the global circulation in each test, but does strongly affect the observed thermal phase curve. I will follow these control tests with a “best-fit” case based on similar tests in Chapter 5.

### 6.2.1 Global Circulation

The model results shown in this chapter were time-averaged over either 100 or 200 days, after the model was spun up for at least 100 days. The model reached equilibrium well before 100 days according to the same conditions as in the previous chapter. Figure 6.2 shows the temperature fields at the pressure level corresponding to the position of the maximum zonal-mean zonal flow of Test 2. This is the level where the effect of the equatorial jet should be strongest. The tests have similar temperature distributions to the equivalent 10 bar H<sub>2</sub> and N<sub>2</sub> tests in Chapter 5, suggesting that the realistic radiative transfer in the new tests does not greatly change the global circulation compared to the previous simulations.

Test 2 has a large day-night contrast due to its high mean molecular weight and short radiative timescale, just like the equivalent test in the previous chapter. Test 1 has a more zonally uniform temperature field due to its low mean molecular weight and long radiative timescale, which is also in agreement with the semi-grey tests. Chapter 4 explains why the radiative timescale affects the global temperature distribution.

Figure 6.3 shows the zonal-mean zonal wind for Tests 1 and 2. The theory in Chapter 3 correctly predicts that the more strongly damped Test 2 should have strong eastward flow at the equator and strong westward flow at high latitudes. Chapter 3 also correctly predicts that the more weakly damped Test 1 should have weaker westward flow at high latitudes. It is not clear why there are two eastward jets at the equator in Test 1, which merits further investigation.

Figure 6.4 shows temperature profiles of atmospheric columns in the model spaced evenly around the equators of Tests 1 and 2. The atmospheric temperature of Test 1 is almost uniform around the equator, except for pressure levels very near the surface, due to the long radiative timescale and efficient heat redistribution. Test 2 has weaker heat redistribution due to its short radiative timescale caused by its higher

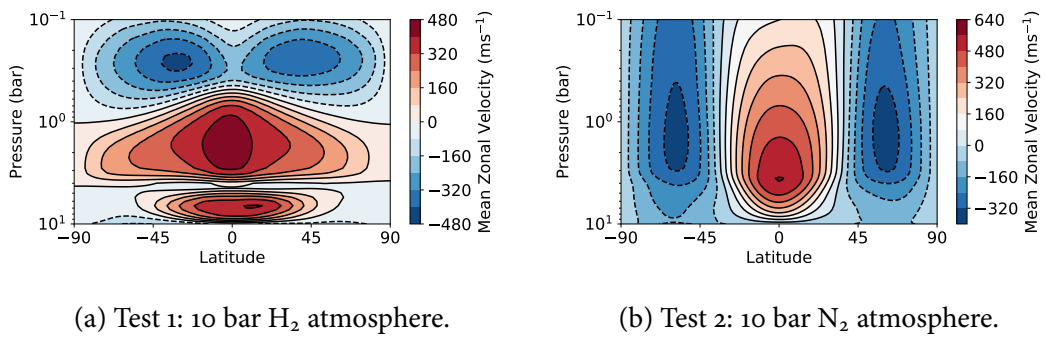


Figure 6.3: Zonal-mean zonal wind of the simulations with 1% CO. The strong westward flow at high latitudes in Test 2 is due to its strong radiative damping.

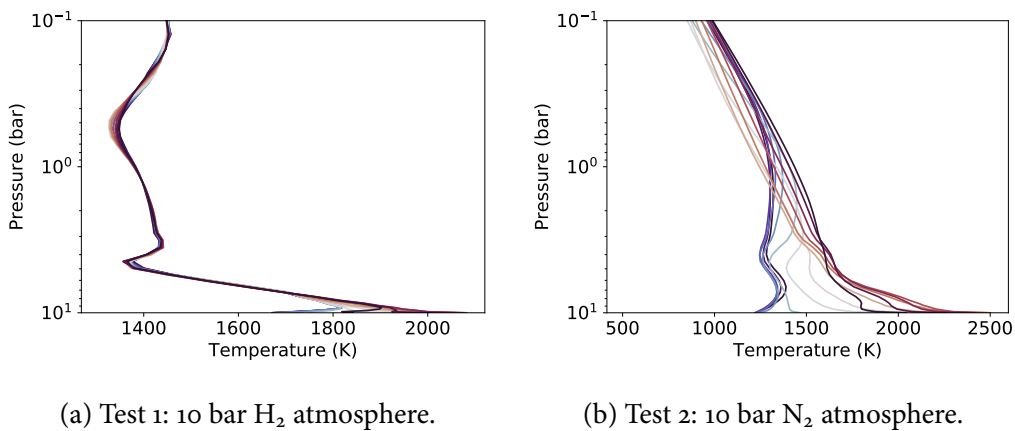


Figure 6.4: Temperature profiles of the simulations with 1% CO. Test 1 has much more efficient heat circulation than Test 2, so its temperature profiles are almost homogeneous.

mean molecular weight, so the day-side and night-side temperature profiles are very different. These profiles are qualitatively similar to the equivalent tests in Chapter 5.

The similarity of the global circulation and temperature structure of these tests to the corresponding tests in the previous chapter suggests that the more realistic radiative transfer does not strongly affect the atmospheric dynamics. This means that the idealised semi-grey model is still useful to investigate the global circulation of these planets. More realistic radiative transfer might be required to model atmospheres with radiative features such as strong shortwave absorption or variable albedo, which could be caused by heterogeneous composition or cloud formation.

### 6.2.2 Thermal Emission

This section shows the outgoing longwave radiation and emission spectra produced by post-processing the final state of each test with a higher-resolution spectral file with 621 bands. Hemisphere-averaged spectra and phase curves were produced with the STARRY software package ([Luger et al., 2019](#)). Figure 6.5 shows the spectral radiance of the outgoing longwave radiation in Tests 1 and 2, from columns evenly spaced around the equator at the substellar point, east terminator, antistar point, and west terminator. Each spectrum shows the three main CO absorption features in this range, at 2000, 4000, and 6000 cm<sup>-1</sup>.

The differences between the OLR of Tests 1 and 2 are only due to their global circulation and the resulting temperature distribution, as they have the same surface pressure and mixing ratio of CO. The substellar and antistar OLR are closer in magnitude in Test 1 than in Test 2, due to the higher day-night contrast in Test 2 discussed above. The eastward heat circulation in Test 1 warms the east terminator, so the emission there is greater than the emission from the west terminator. This effect is reversed in Test 2, where the stationary wave response temperature field in Test 6.2 is not shifted by the zonal flow due to the short radiative timescale (giving a wave pattern similar to the response to forcing in [Matsuno \(1966\)](#)). This means that the west terminator is warmer (as the unshifted stationary wave response is stronger there), making the OLR at the west terminator stronger than that at the east terminator. Observations of spectrally resolved phase curves may reveal dynamical effects like this in the future ([Stevenson et al., 2014](#)).

Figure 6.6 shows simulated emission spectra of the day-sides and night-sides of Tests 1 and 2. These contain the same information as the plots in Figure 6.5, but the emission spectra are averaged over the hemisphere and divided by the stellar flux at that wavelength. The vertical dashed lines show the wavelengths of the phase curves

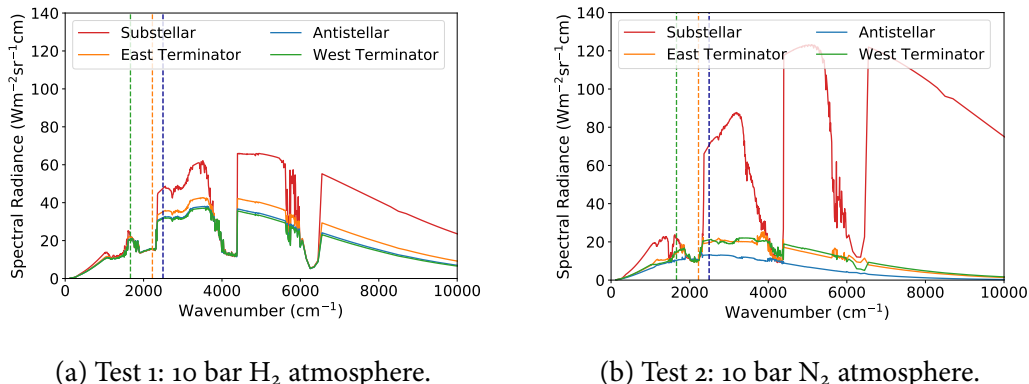


Figure 6.5: Spectral radiance of the outgoing longwave radiation (OLR) of Tests 1 and 2, showing the main CO absorption features at  $2000$ ,  $4000$ , and  $6000\text{ cm}^{-1}$ . The relative magnitudes of the fluxes at each longitude are due to the instellation and global circulation.

plotted later in Figure 6.7, and the shaded region shows the extent of the  $4.5\text{ }\mu\text{m}$  *Spitzer* bandpass used by Demory et al. (2016).

The spectra show the same absorption features as Figure 6.5. Emission features could appear in these spectra given a temperature inversion, which would require a shortwave absorber high in the day-side atmosphere. The differences between the day-side and night-side emission spectra show the day-night contrast of each test, which is much larger in Test 2 than Test 1. These figures show the three-dimensional radiative and dynamical information contained in phase-resolved emission spectroscopy, which may be possible for lava planets like 55 Cancri e using upcoming telescopes such as ARIEL (Stevenson et al., 2014; Tinetti et al., 2016).

### 6.2.3 Thermal Phase Curves

Figure 6.7 shows thermal phase curves calculated from snapshots of the thermal emission of Tests 1 and 2 at a higher spectral resolution. Figure 5.1 showed that the phase curve is the hemisphere-integrated emission from the planet as a function of orbital phase. Note that the phase curves in this chapter are plotted by orbital phase rather than planetary longitude, so are reversed compared to the simulated phase

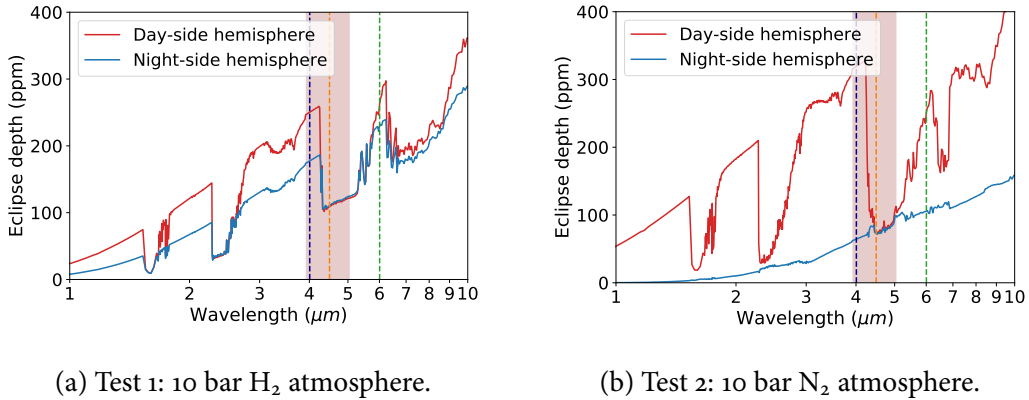


Figure 6.6: Emission spectra of the day-side and night-side of Tests 1 and 2, showing the CO absorption features. The day-night contrast varies with atmospheric opacity. The green, orange, and blue dashed lines show the wavelengths corresponding to the phase curves of the same colours in Figure 6.7.

curve in Chapter 5. The thick black line in Figure 6.7 is the phase curve measured by Demory et al. (2016), with a hot-spot shift of  $41^\circ$  east of the substellar point, and a day-night contrast of 1300 K. The observed phase curve contains the primary and secondary eclipses at phases of 0 and  $\pi$ , unlike those calculated from the simulations.

The colours of the other phase curves correspond to the wavelengths shown by the dashed lines of the same colours in Figure 6.6. The atmospheric opacity at the wavelength of the phase curve determines the contributions of each pressure level to the thermal emission, making the phase curve depend strongly on the wavelength observed. This is similar to the effect of varying the radiating level in Chapter 5. A phase curve at a low atmospheric opacity or at a radiating level close to the surface will have a large day-night contrast, and vice versa. The thick red lines shows the phase curves that would be observed in the *Spitzer* 4.5  $\mu\text{m}$  bandpass. They are weighted by the response function of the IRAC<sup>1</sup> instrument, which corresponds to the band shaded in red in Figure 6.6.

None of the phase curves in Figure 6.7 have a significant phase offset, despite

<sup>1</sup>The Infrared Array Camera, with a response function available at [irsa.ipac.caltech.edu/data/SPITZER/docs/irac/calibrationfiles/spectralresponse](http://irsa.ipac.caltech.edu/data/SPITZER/docs/irac/calibrationfiles/spectralresponse)

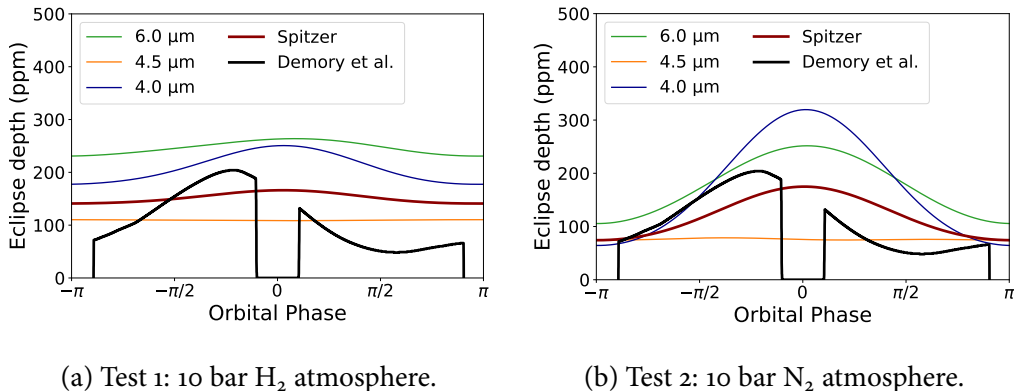


Figure 6.7: Thermal phase curves of Tests 1 and 2. The thick black line shows the phase curve observed by [Demory et al. \(2016\)](#) in the *Spitzer* 4.5  $\mu\text{m}$  channel. The thick red line is the phase curve simulated from each test using the same 4.5  $\mu\text{m}$  bandpass. The other coloured lines show phase curves calculated at the wavelengths plotted in the same colours in Figure 6.6.

the efficient heat redistribution in Test 1. The OLR is dominated by emission from the surface at most wavelengths. The surface temperature is closely coupled to the instellation, so there is normally no large phase shift in its emission. I will discuss the implications of this later in the chapter.

The day-night contrasts of the phase curves in Figure 6.7 depend on both the mean molecular weight of the atmosphere, and the opacity of the atmosphere at the wavelength observed. The phase curves of Test 1 have smaller day-night contrasts in Test 2 due to the stronger heat circulation in Test 1; this is consistent with the results of Chapter 5. Larger day-night contrasts are also seen in the phase curves observed at wavelengths of lower opacity such as the blue 4.0  $\mu\text{m}$  curves, where the emission from the surface dominates the OLR. Conversely, the orange 4.5  $\mu\text{m}$  lines in both cases are almost flat as the OLR is from very high in the atmosphere where the temperature is almost uniform. The thick red line calculated in the *Spitzer* bandpass observed by [Demory et al. \(2016\)](#) approximately matches the day-night contrast of the observations in Test 2, but does not match any of the features in Test 1.

### 6.2.4 Control Tests Summary

The control tests using the updated model with the *Socrates* radiative transfer scheme qualitatively matched the global circulation and temperature distribution of the corresponding tests in Chapter 5. This suggests that the semi-grey radiative transfer was a good approximation to the more realistic model in this chapter.

However, the simulated observations of Tests 1 and 2 were very different to the results of Chapter 5. The realistic radiative transfer showed that the phase curves depended strongly on the atmospheric opacity, and that this was degenerate with other properties such as mean molecular weight. Neither of the control tests matched the observed phase curve well, so in the next section I will discuss two tests that were designed to fit the observations more closely.

## 6.3 Best-Fit Simulation Results

The control simulations did not match the observed phase curve. As in Chapter 5, their extreme mean molecular weights led to either too much heat redistribution, or too little. I therefore ran a new test similar to the “best-fit” simulation in the previous chapter with an intermediate mean molecular weight. This new test, Test 3, has a mixing ratio of 0.1 N<sub>2</sub> and 0.9 H<sub>2</sub>. Its other parameters are the same as the two control tests, with a mixing ratio of 0.01 CO and a 10 bar surface pressure. The results of Test 3 are plotted as a time-average from 200 to 400 days.

This section shows its global circulation and simulated observations. I will show how the scaling relations from Chapter 5 still describe the changes in global circulation compared to the control tests. However, the simulated observations will show that there is no observable phase offset in the thermal phase curve despite the hot-spot shift in the temperature field. I will suggest that this is because the surface pressure is too low, and in the next section will simulate a thicker atmosphere.

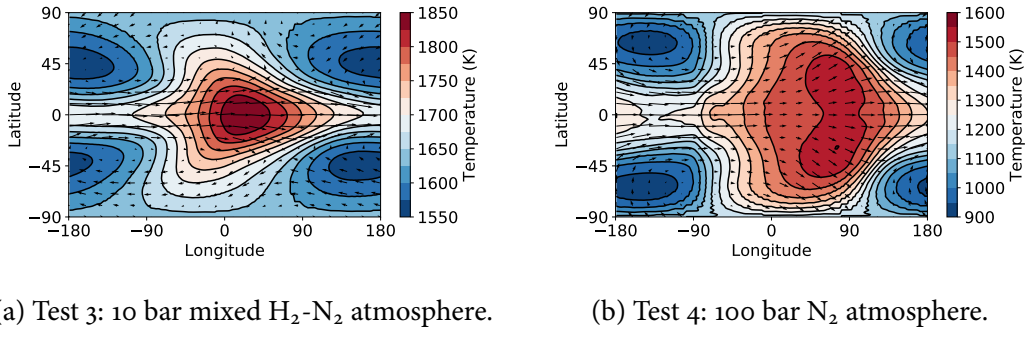


Figure 6.8: Global temperature maps of Tests 3 and 4, at pressure levels chosen to show the largest hot-spot shift. Test 3 is plotted at the 8.24 bar pressure level, and has a small hot-spot shift that does not appear in the thermal phase curve. Test 4 is plotted at the 28.3 bar pressure level, and has a large hot-spot shift that appears in the thermal phase curve.

### 6.3.1 Global Circulation

Figure 6.8a shows the global temperature field at the pressure level of the maximum zonal-mean zonal velocity for Test 3. It has a distinct hot-spot shift and day-night contrast due to its intermediate mean molecular weight, like the best-fit test in Chapter 5. The hot-spot shift is smaller than that of the test in Chapter 5, possibly due to the different radiative transfer scheme in this chapter, but should still affect the thermal emission from the layer of the jet. Figure 6.9a shows the zonal-mean zonal flow, with a single eastward equatorial jet that produces the hot-spot shift. The westward flow at high latitudes is weaker than Test 2 but stronger than Test 1. This is consistent with the predictions of Chapter 3, as its radiative damping timescale is shorter than Test 1 but longer than Test 2.

Figure 6.10a shows the temperature profiles around the equator of Test 3. There is more day-night variation than Test 1 and less day-night variation than Test 2, as expected from the intermediate radiative timescale. The global circulation and resulting temperature distribution is similar overall to the corresponding best-fit test with semi-grey radiative transfer in Chapter 5.

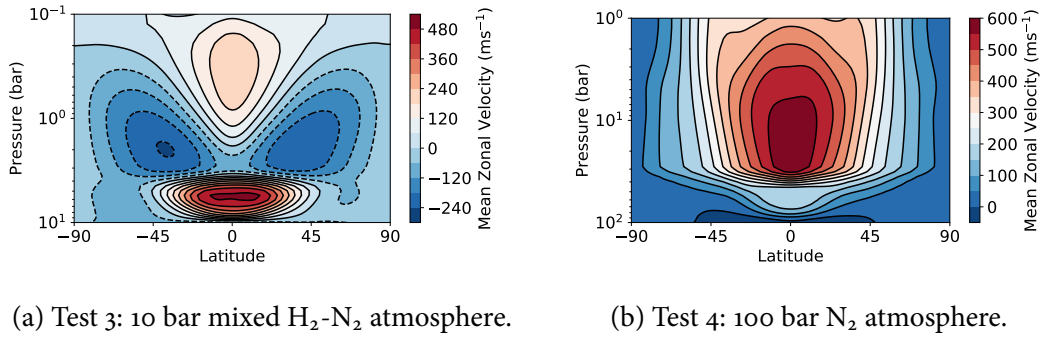


Figure 6.9: Zonal-mean zonal wind of Tests 3 and 4, showing an equatorial jet produced by longwave heating in Test 3 and a similar jet produced mostly by shortwave heating in Test 4.

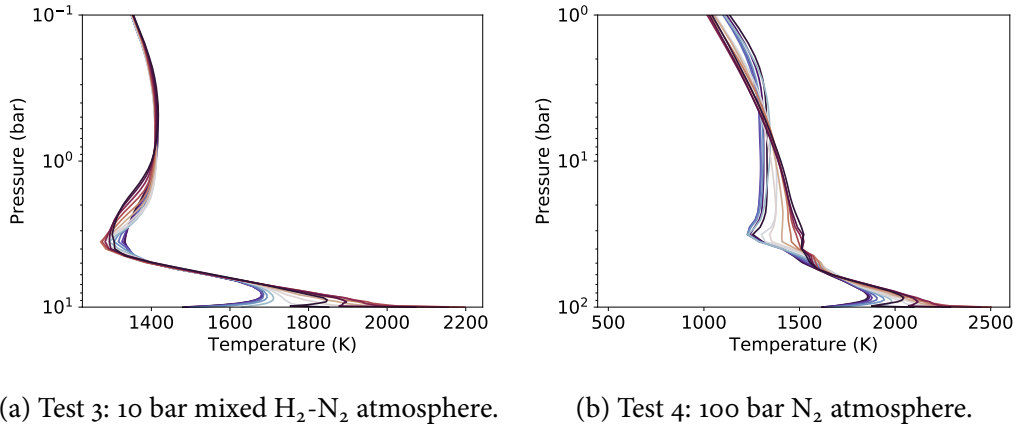


Figure 6.10: Temperature profiles around the equators of Tests 3 and 4, showing the moderate day-night variation in Test 3 and the greater day-side heating due to shortwave absorption in Test 4.

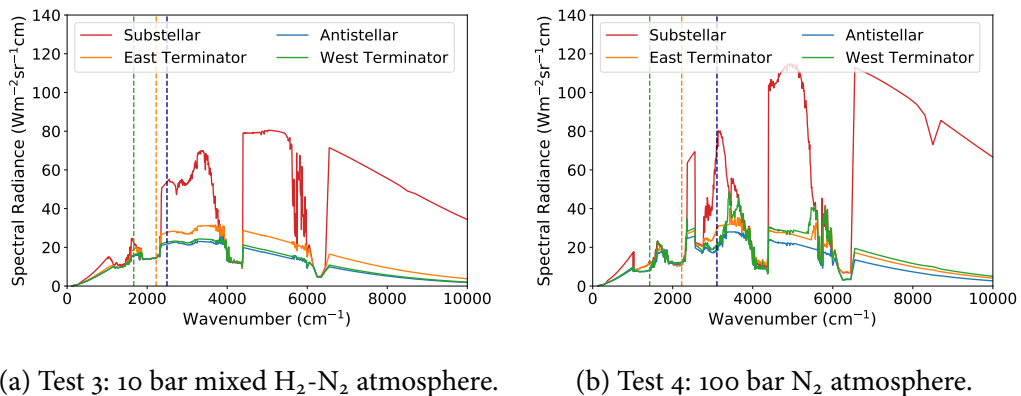


Figure 6.11: Outgoing longwave radiation of Tests 3 and 4 from various columns on their equators, showing the same CO absorption features as Figure 6.5.

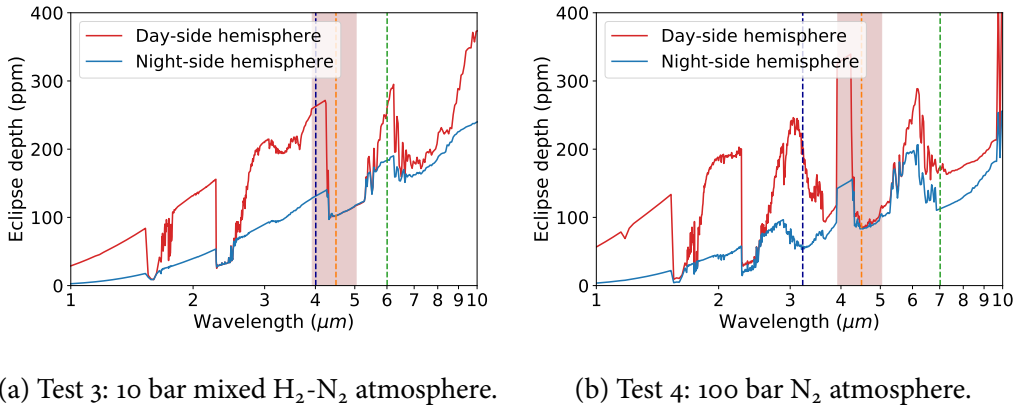


Figure 6.12: Thermal emission spectra of the day-sides and night-sides of Tests 3 and 4, showing the same absorption features as Figure 6.11 and relative magnitudes that depend on the atmospheric heat distribution efficiency.

### 6.3.2 Thermal Emission

Figure 6.11a shows the outgoing longwave radiation from atmospheric columns spaced evenly around the equator of Test 3. The CO absorption features have a greater magnitude than Test 1, but are smaller than those in Test 2. Figure 6.12a shows the emission spectra of the day-side and night-side of Test 3. The intermediate molecular weight of the atmosphere means that the heat redistribution is stronger than Test 2, but weaker than Test 1. This means that the magnitudes of the day-side and night-side spectra are closer than they are in Test 2, but are further apart than in Test 1. Observations of spectrally resolved phase curves could be compared to simulations like these to constrain the day-side and night-side temperature structures.

### 6.3.3 Thermal Phase Curves

Figure 6.13a shows phase curves simulated from the thermal emission of Test 3, in the same spectral bands as Figure 6.7. The best-fit test in Chapter 5 produced a phase curve that matched the hot-spot shift observed by Demory et al. (2016). However, Test 3 does not have a phase offset in any of its phase curves, despite the hot-spot shift in its temperature field.

The *Spitzer* bandpass and the wavelengths chosen for the phase curves cover a range of atmospheric opacities, so should probe a range of radiating levels. The phase curves at low and high atmospheric opacities have large and small amplitudes respectively, as discussed previously for the control test. The phase curves at the intermediate opacity of 6.0  $\mu\text{m}$  and in the *Spitzer* band should probe the mid-atmosphere where the hot-spot shift is present. They show no phase shift, unlike the equivalent test in the previous chapter.

So, why does the hot-spot shift in the temperature field not appear in these phase curves? The hot-spot shift is not as large as the equivalent test in the previous chapter, but should still be large enough to shift the position of the maximum thermal emission at the level of the jet. However, the thermal emission from the surface appears to dominate the emission from the pressure level of the jet at the wavelength plotted (apart from 4.5  $\mu\text{m}$ , where the phase curve is from high in the atmosphere and is almost flat). The surface temperature is closely coupled to the incoming stellar radiation, so has no hot-spot shift. This shows that the atmosphere is too thin to observe the hot-spot shift in the temperature field, as the surface dominates the thermal emission. Hot-spot shifts are regularly observed and simulated in the atmospheres of hot Jupiters ([Zellem et al., 2014](#); [Showman et al., 2015](#)), suggesting that a sufficiently thick atmosphere is required for a phase offset in the outgoing longwave radiation. The next section will show the results of a simulation of a 100 bar atmosphere on 55 Cancri e, which will be thick enough to produce an observable offset in its thermal phase curve.

## 6.4 Thick Atmosphere Results

This section shows the results of Test 4, a simulation with a 100 bar surface pressure, to test the hypothesis that a sufficiently thick atmosphere is required for an offset in

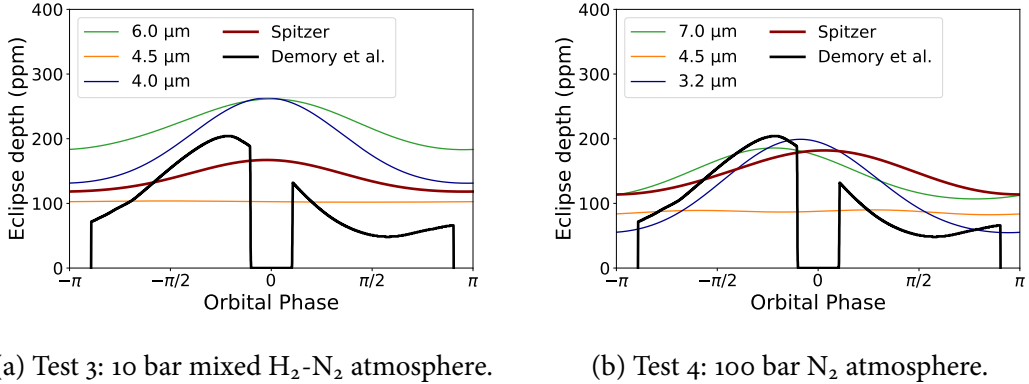


Figure 6.13: Phase curves at different wavelengths and in the *Spitzer* bandpass of Tests 3 and 4. Test 3 has no phase offset at any wavelength, due to its thin atmosphere. Test 4 has a significant phase offset at 7.0  $\mu\text{m}$ , due to its thick atmosphere.

the thermal phase curve. The higher mean molecular weight of its  $\text{N}_2$  atmosphere balances the effect of the increased surface pressure, which would otherwise increase the radiative timescale and decrease the hot-spot shift.

Significant emission from the pressure level of the equatorial jet is needed for an offset in the thermal phase curve, so that emission from the hot-spot shift dominates emission from the level heated in phase with the stellar radiation. In the 10 bar atmospheres earlier, the thermal emission was always dominated by emission from the surface which has no hot-spot shift. At wavelengths where the atmospheric opacity was high, such as the 4.5  $\mu\text{m}$  phase curves earlier, the emission from the jet level dominated the emission from the surface. However, the high opacity meant that the phase curve reflected a radiating level high in the atmosphere so was almost flat.

This section will show that there is an observable hot-spot shift in the temperature field and outgoing longwave radiation of Test 4, supporting the hypothesis that a thick atmosphere is needed to observe a hot-spot shift. This thick atmosphere is more similar to a hot Jupiter, where hot-spot shifts are commonly simulated and observed. I will conclude that this simulation is evidence for an atmosphere on 55 Cancri e with a surface pressure greater than 10 bar.

### 6.4.1 Global Circulation

Figure 6.8b shows the global temperature map and winds at the pressure level of Test 4 where the equatorial jet is strongest, as a time-average from 200 to 400 days. There is a strong eastward hot-spot shift and a large day-night contrast. Test 2 had a similar 10 bar N<sub>2</sub> atmosphere with no hot-spot shift in Figure 6.2; the hot-spot shift in Test 4 is due to the increased radiative timescale caused by the higher surface pressure ([Zhang and Showman, 2017](#)).

Figure 6.9b shows the zonal-mean zonal wind of Test 4. It is similar to the zonal wind of a hot Jupiter simulation, where the equatorial jet extends through many pressure levels due to shortwave heating through the atmosphere ([Showman et al., 2015](#)). The prograde eastward flow at all latitudes at the level of the maximum equatorial jet speed is explained by the mechanism discussed in Chapter 3.

Figure 6.10b shows the temperature profiles around the equator of this test. They are similar to the temperature profiles of the other tests, but show higher temperatures high on the day-side due to the increased effect of shortwave absorption. In reality, a 100 bar atmosphere would have a higher opacity at all wavelengths due to collision-induced absorption, so shortwave absorption would play a greater role in the temperature profiles, as in the atmospheres of hot Jupiters ([Amundsen et al., 2016](#)).

### 6.4.2 Thermal Emission

Figure 6.11b shows the outgoing longwave radiation from the substellar point, antistar point, and terminators on the equator of Test 4. The spectrum has the same absorption features as before, with deeper features than the other tests in regions of intermediate opacity due to the thicker atmosphere. Figure 6.12b shows the emission spectrum of the day-side and night-side of Test 4, which also has deeper absorption

features than the previous tests. The magnitude of the emission is higher than the previous tests, due to the increased surface temperature of the thicker atmosphere. As discussed above, in reality such a thick atmosphere would have a higher opacity in the absorption windows in this test, meaning that the emission from the surface would not appear in the OLR. However, this idealised situation is useful for comparing the effect of different opacities on the thermal emission and phase curves.

#### 6.4.3 Thermal Phase Curves

Figure 6.13b shows phase curves calculated from Test 4 at various wavelengths and in the *Spitzer* 4.5  $\mu\text{m}$  bandpass. Note that the wavelengths of the phase curves are different to those chosen for the previous tests, to highlight new behaviour. The green phase curve at 7.0  $\mu\text{m}$  has a large phase offset, a feature that did not appear in the phase curves of the other tests in this chapter. This supports the hypothesis that a sufficiently thick atmosphere is required to observe a hot-spot shift in the phase curve. The blue 3.2  $\mu\text{m}$  phase curve matches the day-side and night-side temperature of the observed phase curve, but not the hot-spot shift. The 4.5  $\mu\text{m}$  opacity is very high, so the phase curve at that wavelength has almost zero amplitude. Even if there were a hot-spot shift at this wavelength it would not be visible due to the small amplitude of the phase curve.

The thick red line calculated in the *Spitzer* bandpass does not match the observations. This suggests that the CO-dominated radiative transfer in the simulations is not a good model of the observed atmosphere. This is not a problem for the conclusions of this chapter, which seeks to show the general effect of variable atmospheric opacity on the global circulation and observed thermal emission. It would be possible to tune the atmospheric radiative properties to probe exactly the right level in the *Spitzer* bandpass, but this would be an artificial fit without any observational constraints of composition. More observations such as emission spectra are needed

to constrain the composition, which would allow for further modelling with more accurate parameters.

I therefore suggest that the observation of the hot-spot shift on 55 Cancri e is evidence for an atmosphere with a higher surface pressure than 10 bar. This is a different conclusion to Chapter 5, which suggested an atmosphere of 1 to 10 bar produced the maximum hot-spot shift. Chapter 5 aimed to find the maximum hot-spot shift and day-night contrast in the temperature field only. This chapter has sought to find the maximum phase offset and amplitude in the thermal phase curve from the spectrally resolved outgoing longwave radiation, which also requires a sufficiently thick atmosphere. So, the conclusions of the chapters are different but do not contradict each other.

## 6.5 Discussion

The first aim of this chapter was to compare the simulations using the new *Socrates* radiative transfer scheme to the results of the semi-grey scheme in the previous chapter. Tests 1, 2, and 3 qualitatively matched the corresponding tests with the semi-grey model, showing that the scaling relations for hot-spot shift and day-night contrast apply to this more realistic model as well ([Zhang and Showman, 2017](#)).

However, there was an important difference between the simulated thermal phase curves in this chapter and Chapter 5. Previously, the phase curves were calculated from the  $4.5\text{ }\mu\text{m}$  flux emitted from a particular atmospheric pressure level radiating as a black body. This approximation meant that if a hot-spot shift appeared in the temperature field at a particular pressure level, it had to appear in the thermal phase curve calculated using that level. The thermal phase curves in this chapter are instead calculated with the OLR simulated by the *Socrates* radiative transfer scheme, which does not correspond to a single pressure level for a given wavelength. In Tests 1, 2,

and 3 this meant that the emission from the surface dominated the emission from the relatively thin atmosphere at most wavelengths, reducing the effect of the atmospheric circulation on the phase curve. In particular, there was no phase offset in any of the phase curves calculated from Tests 1, 2, and 3.

This is due to the fact that surface temperature is higher than the jet layer temperature. The relative emission can be estimated with a simple model. If the lower atmosphere follows a dry adiabat and the jet layer is at half the surface pressure, the temperature of the jet layer is  $T_{jet} = 0.5^{R/c_p} T_{surf}$ , where  $R/c_p$  is the dry adiabatic lapse rate. This gives  $T_{jet} \approx 0.8 T_{surf}$  for an  $N_2$  atmosphere, which means that the black-body emission from the surface is stronger than the emission from the level of the jet –  $B_{surf} \approx 2.4 B_{jet}$ . Therefore, a sufficiently high opacity is required for the emission from the level of the jet to be stronger than the emission from the surface. However, this high opacity may mean that the emission from the jet is weakened, and the outgoing radiation is dominated by a level above the jet. There may be no appropriate opacity for a thin atmosphere to give a thermal phase curve dominated by emission from the level of the equatorial jet.

Therefore, it is unlikely that a hot-spot shift will appear in the thermal phase curve of a terrestrial planet with a thin atmosphere. Hot-spot shifts are regularly seen in observations and simulations of hot Jupiters with thick atmospheres ([Amundsen et al., 2016](#); [Parmentier and Crossfield, 2017](#)). Hot Jupiters have much deeper zonal jets due to the shortwave heating through a large range of pressure levels of their atmosphere, rather than the longwave heating that produces a strongly forced jet in a small pressure range on a terrestrial planet. They also have much thicker atmospheres, meaning that the thermal emission from the potentially hotter deep atmosphere does not affect the OLR, unlike the emission from the surface in these terrestrial planets.

The results in this chapter suggest that a hot-spot shift will appear in the thermal emission only for a surface pressure of at least 10 to 100 bar. This effect accounts

for the difference between the 10 bar tests and the 100 bar Test 4, where a hot-spot shift only appeared in the thermal phase curve of the thicker atmosphere. These simulations therefore present a different conclusion to those in Chapter 5. Instead of a 5 bar atmosphere with a mean-molecular weight of  $4.6 \text{ g mol}^{-1}$ , they suggest that an atmosphere thicker than 10 bar is required, and that a heavier mean molecular weight may be required to compensate for the increased radiative timescale.

This conclusion does not contradict the work in Chapter 5. Chapter 5 used scaling relations and simulations to identify the largest day-side temperature, day-night contrast and hot-spot shift possible in the temperature field of 55 Cancri e, as the radiative transfer could not accurately model the outgoing longwave radiation. This chapter, on the other hand, aimed to find the best-fitting phase curve at a particular wavelength. This required a higher surface pressure, which warmed the night-side further (a problem with matching the observations in the previous chapter), but produced an observable hot-spot shift in the thermal phase curve that matched the observations.

The temperature fields of these simulations showed variability similar to that discussed in Chapter 5 ([Pierrehumbert and Hammond, 2019](#)). It is possible that this means that the observed phase curve corresponds to a period of increased hot-spot shift or day-night contrast, and that more observations are required to find the true time-mean thermal phase curve. Processes such as condensable transport or cloud formation could cause a more complex climate, or variability in the thermal emission ([Parmentier et al., 2013](#)). Studies such as [Parmentier et al. \(2016\)](#) and [Lines et al. \(2018\)](#) showed the strong effect that cloud formation can have on the emitted and reflected radiation. A collaboration is underway to follow up this work with Graham Lee, coupling the DIHRT model of cloud formation and transport to Exo-FMS, to investigate the effect of clouds formed by species outgassed by the magma ocean ([Lee et al., 2016; Lines et al., 2018](#)).

## 6.6 Conclusions

This chapter used simulations in an updated version of the GCM Exo-FMS to show the effect of realistic radiative transfer on the climate and thermal phase curve of 55 Cancri e. The global circulation and temperature distribution of these simulations qualitatively matched the grey-gas simulations in the previous version of Exo-FMS. However, the thermal phase curves calculated with the more realistic radiative transfer did not match the observations in the 10 bar tests, as the thermal emission was dominated by the hotter surface which has no hot-spot shift.

This suggested that the hot-spot shift observed in the thermal emission requires a thicker atmosphere, comparable to a hot Jupiter. A test with a surface pressure of 100 bar had a hot-spot shift in its temperature field, and also a phase shift in its thermal phase curve at some wavelengths. It may therefore not be possible to observe dynamical features such as hot-spot shifts in thermal phase curves of terrestrial planets with atmospheres thinner than about 10 bar. This many mean that the phase curve of LHS 3844b measured [Kreidberg et al. \(2019\)](#) to have no hot-spot shift, may not yet be evidence for the lack of an atmosphere, or even for the lack of a hot-spot shift.

In summary, the simulations with more realistic radiative transfer suggest that a thick atmosphere is required on 55 Cancri e to explain the observed thermal phase curve. It appears to be much harder to match the observed phase curve of a terrestrial planet than a hot Jupiter, due to the variety of possible atmospheric composition and efficiency of heat redistribution, and the strong effect of the surface on the thermal emission.

This chapter modifies the conclusions of Chapter 5, suggesting the phase curve requires an atmosphere with a surface pressure higher than 10 bar, and a mean molecular weight higher than H<sub>2</sub>. Test 4 matched the observed phase curve at some wavelengths, suggesting that a 100 bar N<sub>2</sub> atmosphere could explain the observations. However,

the effects of the radiative and thermodynamic properties of the atmosphere are degenerate and can produce the same effects on the phase curve. More observations are needed to better constrain the composition and temperature distribution of this planet.

# CHAPTER 7

## *Conclusions*

---

This thesis aimed to understand the atmospheric circulation and global temperature distribution of tidally locked planets. The first two chapters addressed the theory of the formation of the atmospheric circulation, and the last two chapters applied this theory to a case study of the observed thermal phase curve of the planet 55 Cancri e.

After introducing the topic of the thesis and reviewing relevant work in Chapters 1 and 2, I investigated the formation of the zonal flow that dominates the atmospheres of tidally locked planets in Chapter 3. I showed that the meridional circulation is vital to the formation of this flow, and used the Gierasch-Rossow-Williams mechanism to explain how it combines with equatorward momentum transport from stationary waves to produce superrotation. This correctly predicted the equilibrium momentum balance at all latitudes in linear and non-linear shallow-water models and 3D GCM simulations. I used this mechanism to explain the qualitative scaling of the zonal flow of a suite of simulations, and concluded that the equatorial jet dominates the high-latitude jets for strong stellar forcing, and vice versa. Further work could apply this mechanism to predict scaling relations for observables such as zonal flow speed and hot-spot shift, or consider how the mechanism operates in the thicker atmospheres of hot Jupiters.

Chapter 4 shows how this zonal flow produces the eastward hot-spot shift in the atmospheres of tidally locked planets. I linearised a shallow-water model on an equatorial beta-plane around an equatorial jet and its associated height perturbation. The resulting response to day-night forcing matched the form of the hot-spot shift seen in 3D simulations. It showed that the hot-spot shift is not a result of advection of hot air from the substellar point. Instead, it is a combination of the stationary Rossby and Kelvin waves excited by the forcing, and the zonally uniform pressure perturbation required to geostrophically balance the equatorial jet. This explained how the observable hot-spot shift and day-night contrast scale with planetary properties. These two chapters showed how the zonal flow forms on a tidally locked planet, and how it then affects the observable temperature distribution.

I applied the theory of the first two chapters to a case study of the observations of the lava planet 55 Cancri e. Chapter 5 used 1D scaling relations and idealised 3D atmospheric simulations to interpret the thermal phase curve measured by [Demory et al. \(2016\)](#). The scaling relations qualitatively predicted the effect of surface pressure and mean molecular weight on the global circulation of the simulations, and on the observable day-night contrast and hot-spot shift. It was possible to match either the observed day-night contrast with a high mean molecular weight atmosphere, or the observed hot-spot shift with a low mean molecular weight and high surface pressure. The “best-fit” simulation with intermediate properties selected using the scaling relations had a hot-spot shift of  $25^\circ$  east compared to the observed value of  $41^\circ$ . I concluded that the scaling relations were a powerful tool to predict simulation results and interpret the observations, but that the radiative effects of gaseous absorbers and clouds needed to be represented to properly model the thermal emission.

Motivated by Chapter 5, Chapter 6 used an improved radiative transfer model to investigate the effect of realistic gaseous absorption on the global climate and the thermal emission of 55 Cancri e. I found that atmospheres with absorption dominated

---

by CO behaved similarly to the idealised grey-gas simulations in the previous chapter, suggesting that this is a useful approximation and that the details of the radiative transfer do not greatly affect the global circulation. However, the thermal emission and simulated observations calculated with the more realistic radiative transfer model were very different to the grey-gas model. They matched the day-night contrasts of the previous chapter, but hot-spot shifts present in the temperature field did not appear in the  $4.5\text{ }\mu\text{m}$  phase curves. I explained why a sufficiently thick atmosphere is required for a shift in the thermal phase curve, and used a test with 100 bar surface pressure to confirm the presence of a shift at higher pressure. I concluded that the phase curve of [Demory et al. \(2016\)](#) is evidence for an atmosphere with surface pressure significantly larger than 10 bar and a mean molecular weight greater than that of  $\text{H}_2$ .

These chapters addressed the theory of the global circulation of tidally locked terrestrial planetary atmospheres step by step. The first two chapters provided a mechanism for the formation of zonal flow, and a description of the effect of the flow on the observable temperature distribution. They showed that the meridional circulation is vitally important to the momentum budget of the equilibrium zonal flow, and that the hot-spot shift is a combination of stationary waves with the pressure structure of the zonal flow itself. The last two chapters showed how this theory applies to a real planet, and how the thermal phase curve of 55 Cancri e constrains its atmospheric composition. I concluded that a sufficiently thick atmosphere is needed to observe the hot-spot shift, and that a sufficiently high mean molecular weight is required to explain the day-night contrast.

The next steps are to use the theory of the first two chapters to make predictions for observations, such as the dependence of the hot-spot shift and jet speed on planetary parameters like rotation rate and temperature. I will investigate the free modes in the shallow-water models in more details, and relate these to the atmospheric variability in simulations ([Pierrehumbert and Hammond, 2019](#)) and observations ([Demory et al.,](#)

## 7. CONCLUSIONS

---

(2015; Armstrong et al., 2017). Further work on the phase curves of 55 Cancri e and other planets would benefit from more detailed 3D modelling, which could include the effects of chemistry and cloud formation.

This thesis has developed a new description of the formation and observable effect of the global circulation of tidally locked terrestrial planets. The study of exoplanetary atmospheres is still very young, and has allowed the work in this thesis to be touched by a great range of stimulating ideas, techniques, and (occasional) real data. I hope that the huge potential of exoplanetary science can be realised, and that there are many more surprises to come.

## Bibliography

---

- Amundsen, D.S. et al. The UK Met Office global circulation model with a sophisticated radiation scheme applied to the hot Jupiter HD 209458b. *Astronomy & Astrophysics*, 595:A36, 2016.
- Angelo, I. and Hu, R. A Case for an Atmosphere on Super-Earth 55 Cancri e. *The Astronomical Journal*, 154(6):232, Dec. 2017.
- Arcangeli, J. et al. Climate of an ultra hot Jupiter-Spectroscopic phase curve of WASP-18b with HST/WFC3. *Astronomy & Astrophysics*, 625:A136, 2019.
- Armstrong, D.J. et al. Variability in the atmosphere of the hot giant planet HAT-P-7 b. *Nature Astronomy*, 1(1):0004, 2017.
- Barnes, R. Tidal locking of habitable exoplanets. *Celestial Mechanics and Dynamical Astronomy*, 129(4):509–536, 2017.
- Boutle, I.A. et al. Exploring the climate of Proxima B with the Met Office Unified Model. *Astronomy & Astrophysics*, 601:A120, May 2017.
- Boyd, J.P. The Effects of Latitudinal Shear on Equatorial Waves. Part I: Theory and Methods. *Journal of Atmospheric Sciences*, 35(1):2236–2258, Dec. 1978.
- Boyd, J.P. *Chebyshev & Fourier Spectral Methods*. Springer, 2000.
- Brogi, M. et al. Rotation and winds of exoplanet HD 189733 b measured with high-dispersion transmission spectroscopy. *The Astrophysical Journal*, 817(2):106, 2016.
- Carone, L., Keppens, R. and Decin, L. Connecting the dots: a versatile model for the atmospheres of tidally locked Super-Earths. *Monthly Notices of the Royal Astronomical Society*, 445(1):930–945, Sept. 2014.
- Carone, L., Keppens, R. and Decin, L. Connecting the dots - II. Phase changes in the climate dynamics of tidally locked terrestrial exoplanets. *Monthly Notices of the Royal Astronomical Society*, 453(3):2412–2437, Nov. 2015.
- Charnay, B., Meadows, V. and Leconte, J. 3D Modeling of GJ 1214b's Atmosphere: Vertical Mixing Driven by an Anti-Hadley Circulation. *The Astrophysical Journal*, 813(1):15, Nov. 2015.

- Cho, J.K., Polichtchouk, I. and Thrastarson, H.T. Sensitivity and variability redux in hot-Jupiter flow simulations. *Monthly Notices of the Royal Astronomical Society*, 454(4):3423–3431, 2015.
- Courant, R., Friedrichs, K. and Lewy, H. Über die partiellen Differenzengleichungen der mathematischen Physik. *Mathematische annalen*, 100(1):32–74, 1928.
- Cowan, N.B. and Agol, E. Inverting phase functions to map exoplanets. *The Astrophysical Journal Letters*, 678(2):L129, 2008.
- Cowan, N.B. and Agol, E. The statistics of albedo and heat recirculation on hot exoplanets. *The Astrophysical Journal*, 729(1):54, 2011.
- Crida, A. et al. Mass, radius, and composition of the transiting planet 55 Cnc e: using interferometry and correlations. *The Astrophysical Journal*, 860(2):122, 2018.
- Crossfield, I.J.M. Observations of Exoplanet Atmospheres. *Publications of the Astronomical Society of the Pacific*, 127(9):941–, Oct. 2015.
- Dawson, R.I. and Fabrycky, D.C. Radial velocity planets de-aliased: a new, short period for super-Earth 55 Cnc e. *The Astrophysical Journal*, 722(1):937, 2010.
- Demory, B.O. et al. Detection of a transit of the super-Earth 55 Cancri e with warm Spitzer. *Astronomy & Astrophysics*, 533:A114, Sept. 2011.
- Demory, B.O. et al. Variability in the super-Earth 55 Cnc e. *Monthly Notices of the Royal Astronomical Society*, 455(2):2018–2027, 2015.
- Demory, B.O. et al. A map of the large day–night temperature gradient of a super-Earth exoplanet. *Nature*, 532(7598):207–209, Mar. 2016.
- Ding, F. and Pierrehumbert, R.T. Convection in condensable-rich atmospheres. *The Astrophysical Journal*, 822(1):24, 2016.
- Dragomir, D. et al. New MOST Photometry of the 55 Cancri System. *Proceedings of the International Astronomical Union*, 8(S293):52–57, 2012.
- Drummond, B. et al. Observable signatures of wind-driven chemistry with a fully consistent three-dimensional radiative hydrodynamics model of HD 209458b. *The Astrophysical Journal Letters*, 855(2):L31, 2018.
- Dunkerton, T.J. Eigenfrequencies and Horizontal Structure of Divergent Barotropic Instability Originating in Tropical Latitudes. *Journal of Atmospheric Sciences*, 47(1): 1288–1301, June 1990.
- Edwards, J. and Slingo, A. Studies with a flexible new radiation code. i: Choosing a configuration for a large-scale model. *Quarterly Journal of the Royal Meteorological Society*, 122(531):689–719, 1996.

- Gierasch, P.J. Meridional circulation and the maintenance of the Venus atmospheric rotation. *Journal of the Atmospheric Sciences*, 32(6):1038–1044, 1975.
- Gillon, M. et al. Improved precision on the radius of the nearby super-Earth 55 Cnc e. *Astronomy & Astrophysics*, 539:A28, 2012.
- Goldreich, P. and Soter, S. Q in the Solar System. *Icarus*, 5(1-6):375–389, 1966.
- Hammond, M. and Pierrehumbert, R.T. Linking the Climate and Thermal Phase Curve of 55 Cancri e. *The Astrophysical Journal*, 849(2):152, Nov. 2017.
- Hammond, M. and Pierrehumbert, R.T. Wave-Mean Flow Interactions in the Atmospheric Circulation of Tidally Locked Planets. *The Astrophysical Journal*, 869(1):65, Dec. 2018.
- Held, I.M. and Hou, A.Y. Nonlinear axially symmetric circulations in a nearly inviscid atmosphere. *Journal of the Atmospheric Sciences*, 37(3):515–533, 1980.
- Held, I.M. and Suarez, M.J. A proposal for the intercomparison of the dynamical cores of atmospheric general circulation models. *Bulletin of the American Meteorological Society*, 75(10):1825–1830, 1994.
- Heng, K. and Showman, A.P. Atmospheric Dynamics of Hot Exoplanets. *Annual Review of Earth and Planetary Sciences*, 43(1):509–540, May 2015.
- Heng, K. and Workman, J. Analytical models of exoplanetary atmospheres. I. Atmospheric dynamics via the shallow water system. *Astrophysical Journal, Supplement Series*, 213(2):27, Aug. 2014.
- Heng, K., Frierson, D.M.W. and Phillipps, P.J. Atmospheric circulation of tidally locked exoplanets: II. Dual-band radiative transfer and convective adjustment. *Monthly Notices of the Royal Astronomical Society*, 418(4):2669–2696, Oct. 2011.
- Hide, R. Dynamics of the atmospheres of the major planets with an appendix on the viscous boundary layer at the rigid bounding surface of an electrically-conducting rotating fluid in the presence of a magnetic field. *Journal of the Atmospheric Sciences*, 26(5):841–853, 1969.
- Iga, S.I. and Matsuda, Y. Shear Instability in a Shallow Water Model with Implications for the Venus Atmosphere. *Journal of Atmospheric Sciences*, 62(7):2514–2527, July 2005.
- Ito, Y. et al. Theoretical emission spectra of atmospheres of hot rocky super-Earths. *The Astrophysical Journal*, 801(2):144, 2015.
- Joshi, M., Haberle, R. and Reynolds, R. Simulations of the atmospheres of synchronously rotating terrestrial planets orbiting M dwarfs: conditions for atmospheric collapse and the implications for habitability. *Icarus*, 129(2):450–465, 1997.

- Kataria, T. et al. The Atmospheric Circulation of the Super Earth GJ 1214b: Dependence on Composition and Metallicity. *The Astrophysical Journal*, 785(2):92, Apr. 2014.
- Kataria, T. et al. The atmospheric circulation of the hot Jupiter WASP-43b: Comparing three-dimensional models to spectrophotometric data. *The Astrophysical Journal*, 801(2):86, 2015.
- Koll, D.D.B. and Abbot, D.S. Deciphering thermal phase curves of dry, tidally locked terrestrial planets. *The Astrophysical Journal*, 802(1):21, Mar. 2015.
- Koll, D.D.B. and Abbot, D.S. Temperature Structure and Atmospheric Circulation of Dry Tidally Locked Rocky Exoplanets. *The Astrophysical Journal*, 825(2):99, July 2016.
- Komacek, T.D. and Showman, A.P. Atmospheric Circulation of Hot Jupiters: Dayside-Nightside Temperature Differences. *The Astrophysical Journal*, 821(1):16, Apr. 2016.
- Komacek, T.D., Showman, A.P. and Tan, X. Atmospheric Circulation of Hot Jupiters: Dayside-Nightside Temperature Differences. II. Comparison with Observations. *The Astrophysical Journal*, 835(2):198, Feb. 2017.
- Kreidberg, L. et al. Absence of a thick atmosphere on the terrestrial exoplanet LHS 3844b. *Nature*, 2019.
- Laraia, A.L. and Schneider, T. Superrotation in terrestrial atmospheres. *Journal of the Atmospheric Sciences*, 72(11):4281–4296, 2015.
- Lebonnois, S. et al. Angular momentum budget in general circulation models of superrotating atmospheres: A critical diagnostic. *Journal of Geophysical Research: Planets*, 117(E12), 2012.
- Leconte, J. et al. Asynchronous rotation of Earth-mass planets in the habitable zone of lower-mass stars. *Science*, 347(6222):632–635, 2015.
- Lee, G. et al. Dynamic mineral clouds on HD 189733b-I. 3D RHD with kinetic, non-equilibrium cloud formation. *Astronomy & Astrophysics*, 594:A48, 2016.
- Lin, S.J. A “vertically lagrangian” finite-volume dynamical core for global models. *Monthly Weather Review*, 132(10):2293–2307, 2004.
- Lines, S. et al. Simulating the cloudy atmospheres of HD 209458 b and HD 189733 b with the 3D Met Office Unified Model. *Astronomy & Astrophysics*, 615:A97, 2018.
- Liu, B. and Showman, A.P. Atmospheric circulation of hot Jupiters: insensitivity to initial conditions. *The Astrophysical Journal*, 770(1):42, 2013.
- Longuet-Higgins, M.S. The eigenfunctions of Laplace’s tidal equation over a sphere.

- Philosophical Transactions of the Royal Society of London. Series A, Mathematical and Physical Sciences*, 262(1132):511–607, 1968.
- Louden, T. and Wheatley, P.J. Spatially resolved eastward winds and rotation of HD 189733b. *The Astrophysical Journal Letters*, 814(2):L24, 2015.
- Luger, R. et al. STARRY: Analytic occultation light curves. *The Astronomical Journal*, 157(2):64, 2019.
- Lutsko, N.J. The response of an idealized atmosphere to localized tropical heating: Superrotation and the breakdown of linear theory. *Journal of the Atmospheric Sciences*, 75(1):3–20, 2018.
- Majeau, C., Agol, E. and Cowan, N.B. A two-dimensional infrared map of the extrasolar planet HD 189733b. *The Astrophysical Journal Letters*, 747(2):L20, 2012.
- Matsuno, T. Quasi-Geostrophic Motions in the Equatorial Area. *Journal of the Meteorological Society of Japan Ser II*, 44(1):25–43, 1966.
- Mayne, N.J. et al. The unified model, a fully-compressible, non-hydrostatic, deep atmosphere global circulation model, applied to hot Jupiters-ENDGame for a HD 209458b test case. *Astronomy & Astrophysics*, 561:A1, 2014.
- Mayne, N.J. et al. Results from a set of three-dimensional numerical experiments of a hot Jupiter atmosphere. *Astronomy & Astrophysics*, 604:A79, Aug. 2017.
- Mayne, N.J. et al. The Limits of the Primitive Equations of Dynamics for Warm, Slowly Rotating Small Neptunes and Super Earths. *The Astrophysical Journal*, 871(1):56, 2019.
- McArthur, B.E. et al. Detection of a Neptune-mass planet in the  $\rho_1$  Cancri system using the Hobby-Eberly Telescope. *The Astrophysical Journal Letters*, 614(1):L81, 2004.
- Mendonça, J.M. et al. THOR: a new and flexible global circulation model to explore planetary atmospheres. *The Astrophysical Journal*, 829(2):115, 2016.
- Mendonça, J.M. et al. Revisiting the Phase Curves of WASP-43b: Confronting Re-analyzed Spitzer Data with Cloudy Atmospheres. *The Astronomical Journal*, 155(4):150, 2018.
- Menou, K. Magnetic scaling laws for the atmospheres of hot giant exoplanets. *The Astrophysical Journal*, 745(2):138, 2012.
- Merlis, T.M. and Schneider, T. Atmospheric dynamics of earth-like tidally locked aquaplanets. *Journal of Advances in Modeling Earth Systems*, 2(4), 2010.
- Miguel, Y. Observability of molecular species in a nitrogen dominated atmosphere for

- 55 Cancri e. *Monthly Notices of the Royal Astronomical Society*, 482(3):2893–2901, 2018.
- Miguel, Y. et al. Compositions of hot super-Earth atmospheres: exploring Kepler candidates. *The Astrophysical Journal Letters*, 742(2):L19, 2011.
- Noda, S. et al. The circulation pattern and day-night heat transport in the atmosphere of a synchronously rotating aquaplanet: Dependence on planetary rotation rate. *Icarus*, 282:1–18, Jan. 2017.
- Norton, W. Tropical wave driving of the annual cycle in tropical tropopause temperatures. Part II: Model results. *Journal of the atmospheric sciences*, 63(5):1420–1431, 2006.
- Parmentier, V. and Crossfield, I.J.M. Exoplanet Phase Curves: Observations and Theory. *Handbook of Exoplanets*, 564(7):116–22, 2017.
- Parmentier, V., Showman, A.P. and Lian, Y. 3D mixing in hot Jupiters atmospheres-I. Application to the day/night cold trap in HD 209458b. *Astronomy & Astrophysics*, 558:A91, 2013.
- Parmentier, V. et al. Transitions in the Cloud Composition of Hot Jupiters. *The Astrophysical Journal*, 828(1):22, Sept. 2016.
- Pekeris, C.L. A Derivation of Laplace’s Tidal Equation from the Theory of Inertial Oscillations. In *Proceedings of the Royal Society of London. Series A*, pages 81–86, June 1975.
- Perez-Becker, D. and Showman, A.P. Atmospheric heat redistribution on hot Jupiters. *The Astrophysical Journal*, 776(2):134, 2013.
- Perryman, M. *The Exoplanet Handbook*. Cambridge University Press, 2018.
- Pierrehumbert, R. and Gaidos, E. Hydrogen Greenhouse Planets Beyond the Habitable Zone. *The Astrophysical Journal Letters*, 734(1):L13, June 2011.
- Pierrehumbert, R.T. *Principles of Planetary Climate*. Cambridge University Press, 2010.
- Pierrehumbert, R.T. and Ding, F. Dynamics of atmospheres with a non-dilute condensable component. *Proceedings of the Royal Society A: Mathematical, Physical and Engineering Sciences*, 472(2190):20160107, 2016.
- Pierrehumbert, R.T. and Hammond, M. Atmospheric circulation of tide-locked exoplanets. *Annual Review of Fluid Mechanics*, 51:275–303, 2019.
- Polichtchouk, I. et al. Intercomparison of general circulation models for hot extrasolar planets. *Icarus*, 229:355–377, 2014.

- Polvani, L.M., Scott, R. and Thomas, S. Numerically converged solutions of the global primitive equations for testing the dynamical core of atmospheric GCMs. *Monthly Weather Review*, 132(11):2539–2552, 2004.
- Putman, W.M. and Lin, S.J. Finite-volume transport on various cubed-sphere grids. *Journal of Computational Physics*, 227(1):55–78, Nov. 2007.
- Read, P. Super-rotation and diffusion of axial angular momentum: II. A review of quasi-axisymmetric models of planetary atmospheres. *Quarterly Journal of the Royal Meteorological Society*, 112(471):253–272, 1986.
- Read, P.L. and Lebonnois, S. Superrotation on Venus, on Titan, and elsewhere. *Annual Review of Earth and Planetary Sciences*, 46:175–202, 2018.
- Ribstein, B., Zeitlin, V. and Tissier, A.S. Barotropic, baroclinic, and inertial instabilities of the easterly Gaussian jet on the equatorial  $\beta$ -plane in rotating shallow water model. *Physics of Fluids*, 26(5):056605, May 2014.
- Rossow, W.B. and Williams, G.P. Large-scale motion in the Venus stratosphere. *Journal of the Atmospheric Sciences*, 36(3):377–389, 1979.
- Rothman, L. et al. HITRAN, the high-temperature molecular spectroscopic database. *Journal of Quantitative Spectroscopy and Radiative Transfer*, 111(15):2139–2150, 2010.
- Shell, K.M. and Held, I.M. Abrupt Transition to Strong Superrotation in an Axisymmetric Model of the Upper Troposphere. *Journal of Atmospheric Sciences*, 61(2): 2928–2935, Dec. 2004.
- Showman, A.P. and Guillot, T. Atmospheric circulation and tides of “51 Pegasus b-like” planets. *Astronomy & Astrophysics*, 385(1):166–180, 2002.
- Showman, A.P. and Polvani, L.M. The matsuno-gill model and equatorial superrotation. *Geophysical Research Letters*, 37(18), 2010.
- Showman, A.P. and Polvani, L.M. Equatorial Superrotation on Tidally Locked Exoplanets. *The Astrophysical Journal*, 738(1):71, Sept. 2011.
- Showman, A.P., Wordsworth, R.D. and Merlis, T.M. Atmospheric Circulation of Terrestrial Exoplanets. *Comparative Climatology of Terrestrial Planets*, 1675:8090, June 2012.
- Showman, A.P., Lewis, N.K. and Fortney, J.J. Three-dimensional atmospheric circulation of warm and hot Jupiters: Effects of orbital distance, rotation period, and nonsynchronous rotation. *Astrophysical Journal*, 801(2):95, Mar. 2015.
- Stevenson, K.B. et al. Thermal structure of an exoplanet atmosphere from phase-resolved emission spectroscopy. *Science*, 346(6211):838–841, 2014.

- Sugimoto, N., Takagi, M. and Matsuda, Y. Fully Developed Superrotation Driven by the Mean Meridional Circulation in a Venus GCM. *Geophysical Research Letters*, 46(3):1776–1784, 2019.
- Thrastarson, H.T. and Cho, J.Y. Effects of initial flow on close-in planet atmospheric circulation. *The Astrophysical Journal*, 716(1):144, 2010.
- Thuburn, J. and Lagneau, V. Eulerian Mean, Contour Integral, and Finite-Amplitude Wave Activity Diagnostics Applied to a Single-Layer Model of the Winter Stratosphere. *Journal of Atmospheric Sciences*, 56(5):689–710, Mar. 1999.
- Tinetti, G. et al. The science of ARIEL (Atmospheric Remote-sensing Infrared Exoplanet Large-survey). In *Space Telescopes and Instrumentation 2016: Optical, Infrared, and Millimeter Wave*, volume 9904. International Society for Optics and Photonics, 2016.
- Tsai, S.M., Dobbs-Dixon, I. and Gu, P.G. Three-dimensional structures of equatorial waves and the resulting super-rotation in the atmosphere of a tidally locked hot Jupiter. *Astrophysical Journal*, 793(2):141, Oct. 2014.
- Tsiaras, A. et al. Detection of an atmosphere around the super-Earth 55 Cancri e. *The Astrophysical Journal*, 820(2):99, 2016.
- Vallis, G.K. Atmospheric and Oceanic Fluid Dynamics. *Atmospheric and Oceanic Fluid Dynamics*, pages 770–, Nov. 2006.
- Von Braun, K. et al. 55 Cancri: Stellar astrophysical parameters, a planet in the habitable zone, and implications for the radius of a transiting super-Earth. *The Astrophysical Journal*, 740(1):49, 2011.
- Wang, H., Boyd, J.P. and Akmaev, R.A. On computation of Hough functions. *Geoscientific Model Development*, 9(4):1477–1488, Apr. 2016.
- Wang, P. and Mitchell, J.L. Planetary ageostrophic instability leads to superrotation. *Geophysical Research Letters*, 41(12):4118–4126, 2014.
- Wetzel, S. et al. Laboratory measurement of optical constants of solid SiO and application to circumstellar dust. *Astronomy & Astrophysics*, 553:A92, 2013.
- Winn, J.N. et al. A super-Earth transiting a naked-eye star. *The Astrophysical Journal Letters*, 737(1):L18, 2011.
- Zellem, R.T. et al. The  $4.5\ \mu\text{m}$  full-orbit phase curve of the hot Jupiter HD 209458b. *The Astrophysical Journal*, 790(1):53, 2014.
- Zhang, X. and Showman, A.P. Effects of Bulk Composition on the Atmospheric Dynamics on Close-in Exoplanets. *The Astrophysical Journal*, 836(1):73, Feb. 2017.

## APPENDIX A

### *The Exo-FMS GCM*

---

A General Circulation Model (GCM) simulates the fluid dynamics of an atmosphere or ocean, coupled to other models of physical processes such as radiative transfer or convection. GCMs are valuable tools for investigating the atmospheric dynamics of new types of exoplanet, as they can simulate a great variety of planetary atmospheres without prior knowledge. This appendix reviews the structure and functionality of the GCM “Exo-FMS” used to model planetary atmospheres in this thesis. Exo-FMS is hosted at [github.com/OxfordPlanetaryClimate](https://github.com/OxfordPlanetaryClimate), and will be made public soon.

#### A.1 Model Structure

Exo-FMS has a simple structure with as few changes as possible to the original code release of the latest cubed-sphere version of the GFDL FMS<sup>1</sup>. In this section, I will give an overview of the modelling structure “FMS”, the dynamical core and physics modules, and the “Exo-FMS” interface between the dynamical core and physics modules.

---

<sup>1</sup>[gfdl.noaa.gov/cubed-sphere-quickstart](https://gfdl.noaa.gov/cubed-sphere-quickstart)

### A.1.1 FMS

Exo-FMS is built on the GFDL “Flexible Modelling System” (FMS)<sup>2</sup>, which is a “software framework for supporting the efficient development, construction, execution, and scientific interpretation of atmospheric, oceanic, and climate system models”. In the context of Exo-FMS, FMS is the framework of the model, which manages the compiling and running of the model, data input and output, parallelisation via MPI, and many utilities such as time-keeping or initialisation.

### A.1.2 Physics Interface

Exo-FMS is based on a single interface between the dynamical core and the physics modules. The interface takes the state of the atmosphere at each timestep (its temperature, pressure, and so on) and passes it to each module in turn. These each return a tendency in some variable (a temperature tendency from the radiative transfer scheme, for example) which are then applied to the atmospheric state.

I produced this interface to simplify the addition of new physics modules to the model. The interface also makes it simple to swap the modules in and out, to model different types of planet. This is very valuable for simulating exoplanets that may have different processes at work in their atmospheres. Developing the new interface allowed more use of the object-oriented style of the recent release of the FMS, giving a more straightforward coupling between the dynamical core and physics modules.

### A.1.3 Physics Modules

The default configuration of the unmodified cubed-sphere release of the FMS couples the dynamical core to a single physics module that applies a “Held-Suarez” forcing scheme ([Held and Suarez, 1994](#)). Exo-FMS includes additional modules to

---

<sup>2</sup>[gfdl.noaa.gov/fms](http://gfdl.noaa.gov/fms)

simulate different physical processes, which can be swapped in and out using the interface discussed above.

The simplest configuration applies dry convective adjustment, a Rayleigh drag at the surface, and semi-grey radiative transfer (Pierrehumbert, 2010). This configuration was used for the simulations in Chapters 3 and 4. Chapter 5 used the same configuration of modules in the previous version of Exo-FMS on latitude-longitude grid. The simulations in Chapter 6 use the new cubed-sphere version of Exo-FMS with the more realistic radiative transfer model *Socrates* (Edwards and Slingo, 1996). The cloud formation and transport model DIHRT has also been coupled to Exo-FMS (Lee et al., 2016). The next steps in the model development will be to add more detailed convective adjustment schemes or to couple it to a chemical model.

#### A.1.4 Utilities

I also produced Python utilities to run the model and process its output. The Python interface to run the model provides a single script to set its input parameters. The interface then produces the model runscript, several Fortran namelists to set the parameters of the test, and sets the model diagnostics that will be saved. After the test finishes, the interface then uses the “cubedsphere” Python package<sup>3</sup> to re-grid the diagnostic fields from a cubed-sphere grid to a latitude-longitude grid for analysis.

## A.2 Finite-Volume Dynamical Core

The dynamical core of the model solves the primitive equations describing the fluid dynamics of the atmosphere (Lin, 2004; Vallis, 2006). A finite-volume core (as opposed to a finite-difference core, or a spectral core) uses a grid of points, each with a surrounding volume that exchanges fluxes with the adjacent volumes.

---

<sup>3</sup>[github.com/JiaweiZhuang/cubedsphere](https://github.com/JiaweiZhuang/cubedsphere)

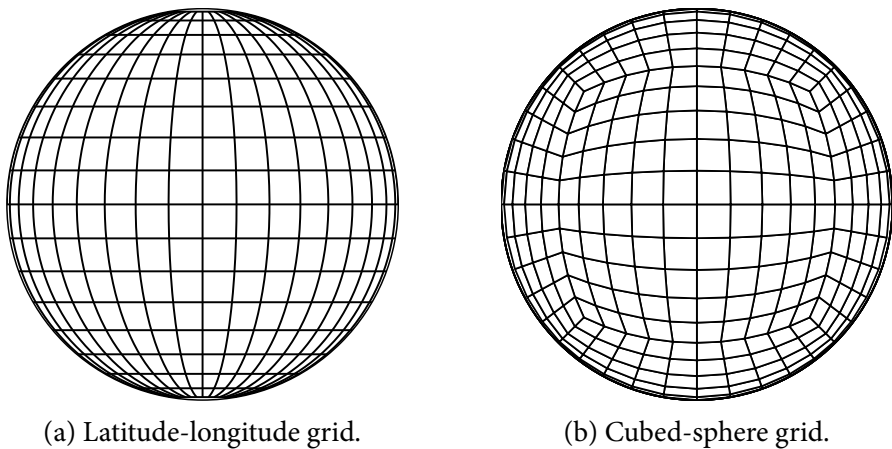


Figure A.1: The old latitude-longitude grid and the new cubed-sphere grid used in Exo-FMS. The new grid avoids the small grid scale at the poles of the old grid, which was a source of instability.

### A.2.1 Latitude-Longitude

The simulations in Chapter 5 used a version of Exo-FMS inherited from [Pierrehumbert and Ding \(2016\)](#). The dynamical core of this version was on a latitude-longitude grid, shown in Figure A.1a. It became clear that the poles of this grid were a source of instability for the high temperature and high winds produced in simulations of 55 Cancri e. The instability was likely due to a failure of the CFL condition at the poles, which requires that

$$C = \frac{u\Delta t}{\Delta x} \leq C_{\max}, \quad (\text{A.1})$$

where  $u$  is the local velocity,  $\Delta t$  is the model timestep,  $\Delta x$  is the local grid scale,  $C$  is the Courant number, which must be below a critical value  $C_{\max}$  ([Courant et al., 1928](#)). On a latitude-longitude grid, the grid scale  $\Delta x$  becomes very small at the poles, requiring a very small timestep  $\Delta t$  to satisfy this condition. I therefore updated the model to use a newer dynamical core on a cubed-sphere grid, which does not have such a small grid scale at its poles.

### A.2.2 Cubed-Sphere

Figure A.1b shows a cubed-sphere grid like the grid used in the updated version of Exo-FMS ([Putman and Lin, 2007](#)). A cubed-sphere grid is a regular grid on the six faces of a cube that is projected onto the surface of a sphere. This creates six “poles” on the grid from the vertices of the cube, as well as small variations in the grid cell sizes. These can produce instabilities at the poles, or artifacts in the pattern of the grid ([Putman and Lin, 2007](#)), but these were never a serious issue in the simulations in this thesis. The updated version of Exo-FMS was found to avoid the instabilities and crashing caused by high winds at the poles of the latitude-longitude grid, and to run more stably which allowed for longer timesteps.



## APPENDIX B

# *Pseudo-Spectral Methods for the Shallow-Water Equations*

---

This appendix describes the pseudo-spectral methods used to solve the linearised shallow-water equations in Chapters 3 and 4. I will give a general description of a pseudo-spectral collocation method, then show the methods used to solve the shallow-water equations on the beta-plane and on a sphere.

### B.1 Pseudo-Spectral Collocation for a Single Equation

A pseudo-spectral collocation method expands the solution to a partial differential equation or system of equations as a series of “basis functions” and then imposes the condition that the equation is satisfied at a number of “collocation points” (Boyd, 2000). The resulting matrix equation provides the coefficients of the series, giving the solution to the initial equation.

For a linear ordinary differential equation:

$$Lu = q \tag{B.1}$$

where  $L$  is a differential operator acting on the variable  $u$ , and  $q$  is the forcing or eigenvalue term, the solution is written as a sum of a series of basis functions:

$$u(x) = \sum a_n \psi_n(x). \quad (\text{B.2})$$

This is solved by imposing the condition that the differential equation is satisfied at  $N$  “collocation points”, the positions of which depend on the set of basis functions. The condition is equivalent to specifying that the “residual” – the difference between the exact solution and the pseudo-spectral series solution – is zero at these points. This provides  $N$  equations to solve for the  $N$  unknowns  $a_n$ , which gives the matrix equation:

$$\mathbf{H}\mathbf{a} = \mathbf{f}, \quad (\text{B.3})$$

where the matrix elements  $H_{ij}$  are the operator  $L$  applied to the modes  $\phi_j$  at the collocation points  $x_i$ , and the vector elements  $f_i$  are the right-hand-side forcing terms  $q$  evaluated at the collocation points  $x_i$ :

$$H_{ij} = L\phi_j(x_i), \quad (\text{B.4})$$

$$f_i = q(x_i). \quad (\text{B.5})$$

Solving Equation B.3 with a numerical method such as LU decomposition gives the coefficients  $a_n$  of the solution  $u(x)$ .

## B.2 Beta-Plane Shallow Water Equations

The method above can be applied to a system of equations rather than a single equation. Equation B.1 is modified so that  $L$  is a matrix and  $u$  and  $q$  are vectors. In the case of a system of forced, time-independent equations:

$$\mathbf{Lu} = \mathbf{q}, \quad (\text{B.6})$$

the condition that the differential equation is satisfied at the collocation points gives the equivalent matrix equation to Equation B.3:

$$\mathbf{Ha} = \mathbf{f}. \quad (\text{B.7})$$

$\mathbf{H}$  is an  $M \times N$  square matrix with elements:

$$H_{ij}^{kl} = L^{kl} \phi_j(x_i), \quad (\text{B.8})$$

i.e. the operator  $L^{kl}$  acting on the  $l$ th variable in the  $k$ th equation, applied to the  $j$ th basis function and evaluated at the  $i$ th collocation point.  $\mathbf{f}$  is a vector made up of  $N$  subvectors  $f_i$ , which are the forcing terms in each equation evaluated at each collocation point.

$$\mathbf{H} = \begin{pmatrix} \left( \begin{matrix} H_{ij} & \dots \\ \vdots & \ddots \end{matrix} \right)^{kl} & \dots \\ \vdots & \ddots \end{pmatrix} \begin{pmatrix} \left( \begin{matrix} \alpha_i \\ \vdots \\ \alpha_i \end{matrix} \right) \\ \vdots \\ \vdots \end{pmatrix} = \begin{pmatrix} \left( \begin{matrix} f_i \\ \vdots \\ f_i \end{matrix} \right) \\ \vdots \\ \vdots \end{pmatrix}. \quad (\text{B.9})$$

$\mathbf{H}$  is the same as the matrix in Equation B.4 with the elements  $H_{ij}$  replaced by submatrices  $H_{ij}^{kl}$ . Solving this system returns the coefficients of the basis functions, and the solutions are:

$$u(y) = \sum_{n=0}^N a_n \phi_n; \quad v(y) = \sum_{n=0}^N b_n \phi_n; \quad h(y) = \sum_{n=0}^N c_n \phi_n. \quad (\text{B.10})$$

This gives a linear matrix equation with one solution corresponding to the coefficient vectors  $a_n, b_n, c_n$  of the forced solution.

For the forced linear shallow-water equations, the matrix equation B.6 corresponds to Equation 3.3 in Chapter 3 ([Matsuno, 1966](#)). These can be solved using the parabolic cylinder functions plotted in Figure B.1a. These functions are appropriate as they obey the boundary conditions of the beta-plane linear shallow-water equations, and the lowest order functions are exact solutions of the shallow-water equations.

Without forcing, the shallow-water equations define a free eigensystem where the eigenvalue is the frequency  $\omega$ .

$$\mathbf{Lu} = \omega \mathbf{Pu}. \quad (\text{B.11})$$

The pseudo-spectral equation is then:

$$\mathbf{Ha} = \omega \mathbf{Ra}, \quad (\text{B.12})$$

where  $\mathbf{R}$  is an  $M \times N$  square matrix with elements:

$$R_{ij}^{kl} = P^{kl} \phi_j(x_i), \quad (\text{B.13})$$

i.e. the eigenvalue operator  $P^{kl}$  acting on the  $l$ th variable in the  $k$ th equation, applied to the  $j$ th basis function and evaluated at the  $i$ th collocation point:

$$\mathbf{H} = \begin{pmatrix} \left( \begin{matrix} H_{ij} & \dots \\ \vdots & \ddots \end{matrix} \right)^{kl} & \dots \\ \vdots & \ddots \end{pmatrix} \begin{pmatrix} \alpha_i \\ \vdots \\ \vdots \end{pmatrix} = \omega \begin{pmatrix} \left( \begin{matrix} R_{ij} & \dots \\ \vdots & \ddots \end{matrix} \right)^{kl} & \dots \\ \vdots & \ddots & \ddots \end{pmatrix} \begin{pmatrix} \alpha_i \\ \vdots \\ \vdots \end{pmatrix}. \quad (\text{B.14})$$

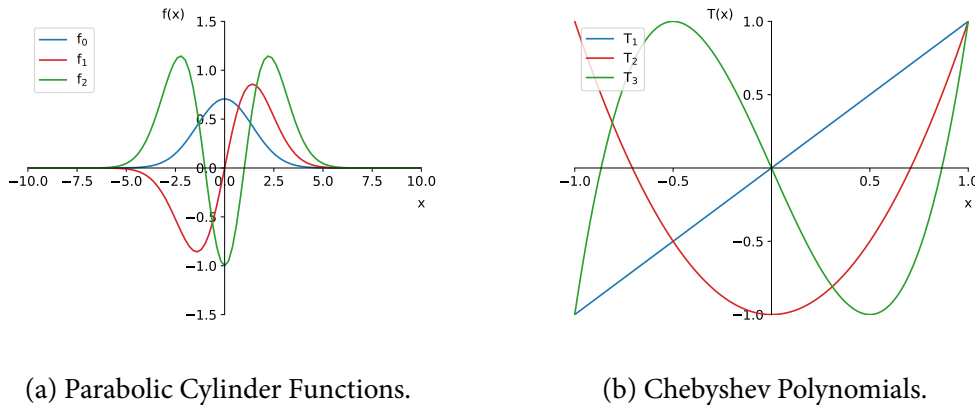


Figure B.1: The basis functions used for the pseudo-spectral methods to solve the shallow-water equations on a beta-plane and on a sphere. The choice of basis function depends primarily on the boundary conditions of the system.

This means that Equation B.11 is a solvable eigenvalue matrix equation, with  $N$  eigenvalues and eigenvectors, corresponding to the frequencies and coefficient vectors  $a_n$ ,  $b_n$ ,  $c_n$  for each free mode. It can be solved with a similar numerical solution to the linear matrix equation in the forced problem. Not all  $N$  modes must be physically realistic, so the spurious modes are identified by inspecting the eigenvalues for different values of  $N$ .

### B.3 Spherical Shallow-Water Equations

This method is used in Chapters 3 and 4 to solve the shallow-water equations on a sphere. These equations are singular with respect to  $u$  and  $v$  at the poles (although real solutions do exist), so all the variables cannot be solved simultaneously as on the beta-plane ([Iga and Matsuda, 2005](#)). Instead, the three shallow-water equations can be reduced to one equation in  $\phi$ , also known as “Laplace’s Tidal Equation” ([Pekeris, 1975](#); [Dunkerton, 1990](#)). This equation can be solved with a pseudo-spectral method, then the solution for  $\phi$  used to find the solutions for  $u$  and  $v$ .

The linear shallow-water equations on the sphere are:

$$\begin{aligned}
\frac{\partial u'}{\partial t} + \frac{\partial(\bar{U}u')}{a \cos \theta \partial \lambda} + v' \frac{\partial \bar{U}}{a \partial \theta} - \frac{\bar{U}v' \tan \theta}{a} &= 2\Omega v' \sin \theta - \frac{g \partial h'}{a \cos \theta \partial \lambda}, \\
\frac{\partial v'}{\partial t} + \frac{\partial(\bar{U}v')}{a \cos \theta \partial \lambda} + \frac{2\bar{U}u' \tan \theta}{a} &= -2\Omega u' \sin \theta - \frac{g \partial h'}{a \partial \theta}, \\
\frac{\partial h'}{\partial t} + v' \frac{\partial \bar{H}}{a \partial \theta} + \bar{U} \frac{\partial h'}{a \cos \theta \partial \lambda} + \bar{H} \nabla_H \cdot \mathbf{v}' &= 0,
\end{aligned} \tag{B.15}$$

where  $h$  is the height of the layer,  $\mathbf{v} = (u, v)$  is the velocity,  $\theta$  is latitude,  $\lambda$  is longitude,  $t$  is time,  $a$  is radius,  $g$  is gravity, and  $\Omega$  is angular velocity. Overbars denote zonal-mean quantities (the background flow and height  $\bar{U}$  and  $\bar{H}$ ). Dashes denote perturbations to this background state.

The background state is stationary and the zonally uniform equatorial jet  $\bar{U}$  is in gradient wind balance:

$$\frac{1}{a} \frac{\partial}{\partial \theta} (\bar{H} + h_g) = - \left( 2\Omega \bar{U} \sin \theta + \frac{\bar{U}^2}{a} \tan \theta \right). \tag{B.16}$$

The perturbed variables are wavelike in longitude and are uniformly damped, so have the form  $X(y) \exp[i m \lambda + \alpha t]$ . All variables are made non-dimensional with velocity scale  $2\Omega a$ , height scale  $(2\Omega a)^2/g$  and time scale  $1/(2\Omega)$ , and denoted as such by an asterisk. This gives the following non-dimensional shallow-water equations:

$$\begin{aligned}
\alpha^* u_m^* + im \frac{\bar{U}^* u_m^*}{\cos \theta} + v_m^* \frac{\partial \bar{U}^*}{\partial \theta} - \bar{U}^* v_m^* \tan \theta &= v_m^* \sin \theta - \frac{im h_m^*}{\cos \theta}, \\
\alpha^* v_m^* + im \frac{\bar{U}^* v_m^*}{\cos \theta} + 2\bar{U}^* u_m^* \tan \theta &= -u_m^* \sin \theta - \frac{\partial h_m^*}{\partial \theta}, \\
\alpha^* h_m^* + im \bar{U}^* \frac{h_m^*}{\cos \theta} &= -\frac{\epsilon^*}{\cos \theta} \left[ imu_m^* + \frac{\partial}{\partial \theta} (\cos \theta v_m^*) \right],
\end{aligned} \tag{B.17}$$

where Lamb's parameter is  $\epsilon \equiv (2\Omega a)^2/gH$ . These can be written as

$$\begin{aligned} -\hat{\sigma}^* u_m^* - \bar{\zeta}^* v_m^* + \frac{mh_m^*}{\cos \theta} &= 0, \\ \hat{\sigma}^* v_m^* + f_1^* u_m^* + \frac{dh_m^*}{d\theta} &= 0, \\ \hat{\sigma}^* \epsilon \alpha h_m^* + \frac{mu_m^*}{\cos \theta} + \frac{1}{\cos \theta} \frac{d}{d\theta} (v \cos \theta) &= 0, \end{aligned} \quad (\text{B.18})$$

where

$$\bar{\zeta}^* = f^* - \frac{1}{\cos \theta} \frac{d}{d\theta} (\bar{U} \cos \theta) \quad (\text{B.19})$$

is the absolute vorticity of the background flow,

$$f_1 = f + 2\bar{U} \tan \theta \quad (\text{B.20})$$

is an effective Coriolis parameter modified by the background flow, and

$$\hat{\sigma}^* = \sigma^* - \frac{m\bar{U}}{\cos \theta} \quad (\text{B.21})$$

is the Doppler-shifted time-derivative of the variables (see Chapter 4). Solving the first two shallow-water equations gives the two velocity components in terms of the height field:

$$\begin{aligned} u_m^* &= \frac{-\hat{\sigma}^* h_m^* m / \cos \theta - \bar{\zeta}^* dh_m^* / dy}{\Delta}, \\ v_m^* &= \frac{\hat{\sigma}^* dh_m^* / dy + f_1^* h_m^* m / \cos \theta}{\Delta}. \end{aligned} \quad (\text{B.22})$$

where  $\Delta = f_1^* \bar{\zeta}^* - \hat{\sigma}^{*2}$ . Then, substituting these into the third shallow-water equation, while changing variables to  $\mu = \sin \theta$  and  $\phi_m^* = (1 - \mu^2)^{-m/2} h_m^*$  to avoid the polar singularities (Iga and Matsuda, 2005), gives:

$$\frac{\partial^2 \phi_m^*}{\partial \mu^2} - B(\sigma^*, \mu) \frac{\partial \phi_m^*}{\partial \mu} - A(\sigma^*, \mu) \phi_m^* = \frac{F(\theta, x)}{i\sigma}, \quad (\text{B.23})$$

where

$$\begin{aligned}
 A(\sigma^*, \mu) &\equiv \frac{1}{1 - \mu^2} \left[ m(m+1) - m\mu \frac{1}{\Delta^*} \frac{\partial \Delta^*}{\partial \mu} + \epsilon \Delta^* \right. \\
 &\quad \left. + \frac{m}{\Delta^* \hat{\sigma}^*} \left( f_1^* \frac{\partial \Delta^*}{\partial \mu} - \Delta^* \frac{\partial f_1^*}{\partial \mu} \right) \right], \\
 B(\sigma^*, \mu) &\equiv \frac{1}{\Delta^*} \frac{\partial \Delta^*}{\partial \mu} + \frac{2\mu(m+1)}{(1 - \mu^2)}, \\
 \Delta^* &\equiv f_1^* \bar{\zeta}^* - \hat{\sigma}^{*2}.
 \end{aligned} \tag{B.24}$$

This equation is then solved with a pseudo-spectral method using the Chebyshev polynomials plotted in Figure B.1 ([Wang et al., 2016](#)). The tidal equation in spherical coordinates can be modified to represent the beta-plane by setting  $\cos \theta = 1$  and  $f_1 = f$  ([Dunkerton, 1990](#)).